

JAERI-M  
9 0 3 2

REACTOR ENGINEERING DIVISION ANNUAL REPORT

(April 1, 1979-March 31, 1980)

September 1980

Division of Reactor Engineering

日 本 原 子 力 研 究 所  
Japan Atomic Energy Research Institute

この報告書は、日本原子力研究所が JAERI-M レポートとして、不定期に刊行している研究報告書です。入手、複製などのお問い合わせは、日本原子力研究所技術情報部（茨城県那珂郡東海村）あて、お申しこしください。

JAERI-M reports, issued irregularly, describe the results of research works carried out in JAERI. Inquiries about the availability of reports and their reproduction should be addressed to Division of Technical Information, Japan Atomic Energy Research Institute, Tokai-mura, Naka-gun, Ibaraki-ken, Japan.

Reactor Engineering Division  
Annual Report  
(April 1, 1979 - March 31, 1980)

Division of Reactor Engineering,  
Tokai Research Establishment, JAERI

(Received July 30, 1980)

Research activities in the Division of Reactor Engineering in fiscal 1979 are described.

The work of the Division is closely related to development of multi-purpose Very High Temperature Gas Cooled Reactor and fusion reactor, and development of Liquid Metal Fast Breeder Reactor carried out by Power Reactor and Nuclear Fuel Development Corporation. Contents of the report are achievements in fields such as nuclear data and group constants, theoretical method and code development, integral experiment and analysis, shielding, reactor and nuclear instrumentation, reactor control and diagnosis, and fusion reactor technology, and activities of the Committees on Reactor Physics and on Decommissioning of Nuclear Facilities.

Keywords: Reactor Engineering, Very High Temperature Gas Cooled Reactor, Thermonuclear Fusion Reactor, Liquid Metal Fast Breeder Reactor, Group Constant, Theoretical Method and Code, Integral Experiment and Analysis, Shielding, Reactor and Nuclear Instrumentation, Reactor Control and diagnosis, Decommissioning of Nuclear Facility.

---

Board of Editors for Annual Report  
J. Hirota (Chief Editor)  
Y. Ishiguro (Associate Chief Editor)  
H. Takano, M. Nakano, F. Akino, K. Ara  
R. Oguma, N. Sasamoto, H. Maekawa

昭和 54 年度原子炉工学部年報

日本原子力研究所東海研究所原子炉工学部

(1980 年 7 月 30 日受理)

昭和 54 年度の原子炉工学部研究活動状況報告書である。原子炉工学部における研究は、多目的高温ガス炉の開発、核融合炉の開発、さらに動燃事業団による液体金属高速増殖炉の開発に密接に関連している。核データと群定数、炉理論とコード開発、積分実験と解析、遮蔽、炉計装と核計装、炉制御と診断、核融合炉技術、および炉物理と原子力施設解体に関する研究委員会活動の各分野にわたり、多くの成果を述べている。

---

年報編集委員会

弘田実弥（編集委員長）

石黒幸雄（副編集委員長）

高野秀機，中野正文，秋濃藤義，荒 克之，尾熊律雄，笹本宣雄，前川 洋

## Foreword

In the present report is given the annual research activity of Division of Reactor Engineering, Japan Atomic Energy Research Institute, for the period of April 1979 - March 1980. The research activity of the Division extends to a broad area of reactor engineering. The major fields are thermal and fast reactor physics, fusion reactor physics, shielding, reactor instrumentation and control, and numerical analysis.

The total number of people working in the Division at the end of period was 84 in which regular members totalled to 74. Expenditures during the period amounted to about 0.64 billion yen, without including personnel expenses. In addition, a considerable amount of expenditures was covered under research contracts with outside organizations, among which Power Reactor and Fuel Development Corporation (PNC) offered the largest contribution.

The research activities were conducted in 7 Laboratories, the Committee on Reactor Physics and the Committee on Study of Decommissioning of Nuclear Facilities. The Laboratories are

Reactor System Laboratory,  
Fast Reactor Physics Laboratory,  
Thermal Reactor Physics Laboratory,  
Reactor Instrumentation Laboratory,  
Reactor Control Laboratory,  
Shielding Laboratory and  
Reactor Physics Experiment Laboratory.

The major research and development projects related closely to research programs in the Division are

- (1) Development of very high temperature gas cooled reactor (VHTR) for multi-purpose use,
- (2) Engineering research of thermonuclear fusion reactor, and
- (3) Development of liquid metal fast breeder reactor (LMFBR).

As concerns research and development of VHTR, reactivity worths of burnable poison rods were measured in a systematic way on SHE and the results were analyzed with LAMP-B code developed for lattice cell analyses by the collision probability method. Long term operation tests for high-temperature neutron detectors have been conducted in the JRR-4 reactor to achieve the high performance at 600 °C. In addition, trial

productions have been performed for tungsten-rhenium thermocouple and a long term test has been carried out for platinum-molybdenum thermocouple to get the stable performance at around 1000 °C. Furthermore, studies have been continued on the control and dynamics characteristics of VHTR.

Concerning the fusion reactor physics, for having a high intensity 14 MeV neutron source, the construction of accelerator system for Fusion Neutronics Source (FNS) has been proceeded to finish the factory test. On the other hand, cross section sensitivity analyses of fission rates have been performed to investigate the discrepancy between calculated and measured results in a graphite reflected lithium oxide assembly.

As for the research and development of LMFBR, fuel slumping experiments were performed on FCA Assembly VIII-2 to measure reactivity changes and flux distribution changes. An improvement was made on a computer code system for generating the group constants from JENDL-2. Furthermore, a study has been proceeded on the cross section evaluation of actinides for burning then in fast reactors. In addition, studies have been conducted on the detection of sodium boiling and on the reactivity anomaly diagnosis.

As concerns researches other than those related closely to the projects, various shielding computer codes have been developed for dealing with anisotropic transmission problems by using the discrete ordinates method or the finite element method. The development of a standard computer code system has been proceeded for nuclear design calculations of thermal reactors. In addition, improvements have been made on semiconductor detectors and developments have been achieved on passive-gamma-ray type non-destructive assay techniques for nuclear materials. Furthermore, investigations have been proceeded on the reactor physics by the Committee on Reactor Physics and on the decommissioning of nuclear facilities by the Committee on Study of Decommissioning of Nuclear Facilities.

Takumi ASAOKA, Acting Head

Division of Reactor Engineering

## CONTENTS

Foreword .....	iii
1. Nuclear Data and Group Constants .....	1
1.1 Preliminary Results of Benchmark Tests on JENDL-2 .....	1
1.2 JFS-3: Group Constants Library Produced with the Group Structure of GAM-Type .....	5
1.3 Production of Group Constants Library for the PALLAS- type Transport Codes with Direct Integration .....	9
1.4 Self-Shielding Effect of Inelastic Scattering Cross Sections of Iron on Neutron Spectrum .....	13
1.5 Calculation of Nuclide Yields Produced by High Energy Proton Spallation Reactions .....	17
2. Theoretical Methods and Code Development .....	19
2.1 SRAC, A Standard Computer Code System for Lattice Cell and Core Calculations on Reactor Design and Analysis ...	19
2.2 Finite Element Method to Solve the Three-Dimensional Neutron Transport Equation .....	23
2.3 Acceleration of Convergence of Iterations in Neutron Diffusion code .....	25
2.4 Detailed Analysis of Reactor Cell and Core Calculations of VHTR .....	28
2.5 Probabilistic Method for Evaluation of Reactivity Margin of VHTR .....	31
2.6 Determination of Order of Priority among Nuclear Data of Actinides by means of Nonlinear Optimization Technique.	32
2.7 Study of the Stochastic Point Reactor Kinetic Equation ..	35
2.8 Kinetics of Anisotropic Particle-Transport in Dense Gases .....	37
2.9 High Resolution Structure Images of a Simple Defect in a Silicon Crystal Oriented in (110) .....	39
3. Integral Experiment and Analysis .....	45
3.1 Measurement of Reactivity Worths of Burnable Poison Rods in SHE-14 Core .....	45
3.2 Fuel Slumping Experiment on FCA Assembly VIII-2 (I): Reactivity Change .....	47

3.3	Fuel Slumping Experiment on FCA Assembly VIII-2 (II): Flux Distribution Change .....	50
3.4	Analysis of Reaction Rate Distribution in Fast Critical Assemblies, ZPPR-2, ZPPR-3 phase 2 and MZB .....	54
3.5	Actinides Cross Section Evaluation by Integral Data and Experimental Program proposed at FCA .....	58
4.	Shielding .....	62
4.1	Effect of Iron Cross Section Valley at 24.3 keV Neutron Shielding .....	62
4.2	Effect of $^{56}\text{Fe}$ Angular Anisotropy for Neutron Penetration .....	67
4.3	A Computational Method for Anisotropic Transmission Problems by $S_N$ -Transport Code .....	72
4.4	An Improvement of the PALLAS Discrete Ordinates Transport Code .....	75
4.5	PALLAS-2DCY-FC, A Computational Method and Radiation Transport Code in Two-Dimensional (R,Z) Geometry .....	78
4.6	A Computer Code FEM-3DP3 for Solving Three-Dimensional Radiation Transport $P_3$ Equation by Finite Element Method ..	79
4.7	Selection of Shielding Benchmark Problems for Evaluating the Data and Methods (II) .....	83
4.8	Measurement and Calculation of Radiation Streaming through Annular Ducts .....	85
4.9	Fast Neutron Transport through Laminated Iron-Water Shield .....	93
5.	Reactor and Nuclear Instrumentation .....	98
5.1	Development of High-Temperature Neutron Detectors .....	98
5.2	Development of High-Temperature Thermocouples for VHTR ..	100
5.3	Preliminary Study of Johnson Noise Thermometer for VHTR Application .....	103
5.4	Development of Organic and Inorganic Composite Insulated Cables .....	106
5.5	Development and Test of On-line Cover-Gas Gamma-Ray Monitor for LMFBR .....	108
5.6	Temperature Dependence of $^3\text{He}$ Proportional Counter Performance .....	109



5.7	Fabrication Technique Development of $\text{HgI}_2$ Radiation Detectors .....	112
5.8	Performance of an Anticoincidence-shielded High-purity Ge Gamma-ray Spectrometer .....	114
5.9	Nondestructive Measurement of FP Plateout Density Using a Portable Ge(Li) Detector with a Lead Collimator .....	117
5.10	Development of Passive Gamma Type Nondestructive Nuclear Material Assay Meter System .....	120
5.11	Portal Monitor Development at FCA for IAEA Safeguards ..	124
5.12	Uncertainty Induced by Count Statistics in Enrichment Measurement with SAM-2 .....	127
5.13	Program Development for Canberra Industries 8100/QUANTA System .....	129
6.	Reactor Control and Diagnosis .....	132
6.1	Preliminary Study on Detection of Sodium Boiling in LMFBR .....	132
6.2	Reactivity Anomaly Diagnosis for Fast Experimental Reactor .....	133
6.3	Reactor Water Level Estimation of a BWR Plant by the Use of Kalman-Bucy Filtering Technique .....	135
6.4	Survey of Existing Robot Technologies for Nuclear Facilities Application .....	138
7.	Fusion Reactor Technology .....	139
7.1	Contruction of Accelerator System for Fusion Neutronics Source (FNS) ---- Factory Test ---- .....	139
7.2	Effect of Hydrogen and Carbon in Lithium-Oxide blocks on Data of Integral Experiments .....	142
7.3	Preliminary Hot-Test on Tritium Scrubber for FNS .....	145
7.4	Cross Section Sensitivity Analysis of $^{235}\text{U}$ and $^{238}\text{U}$ Fission Rates in a Graphite Reflected Lithium Oxide Assembly .....	148
7.5	Development of Ge Thin Film Bolometer for Plasma Radiation Loss Measurement .....	150
8.	Activities of the Committees .....	153
8.1	Activities Related to the NEA Committee on Reactor Physics .....	153

8.2	Activities of the Subcommittees on Reactor Physics .....	155
8.3	Activities of the Japanese Preparatory Committee for SMORN-III .....	157
8.4	Activities of the Committee on Study of Decommissioning of Nuclear Facilities .....	158

## 1. Nuclear Data and Group Constants

### 1.1 Preliminary Results of Benchmark Tests on JENDL-2

Y. Kikuchi, T. Narita and H. Takano

At the first step of the compilation of JENDL-2, the highest priority was put to evaluation of most important nuclides for fast reactors:  $^{235}\text{U}$ ,  $^{238}\text{U}$ ,  $^{239}\text{Pu}$ ,  $^{240}\text{Pu}$ ,  $^{241}\text{Pu}$ , Cr, Fe and Ni. This decision was made responding to an urgent request to use JENDL-2 for analyses in the JUPITER project. The evaluation of the 8 nuclides above mentioned was completed in November 1979.

The benchmark tests were made on these evaluated data. The group constants based on JENDL-1 were used for other nuclides. This combined library of JENDL-2 for the 8 nuclides and JENDL-1 for the others is called JENDL-2B library. The benchmark problems are the same as those used in the benchmark tests of JENDL-4<sup>1)</sup>, and are based on one dimensional diffusion and first order perturbation approximations. The calculated results are given in the form of C/E values, and are compared with those of JENDL-1<sup>1)</sup>, JAERI-Fast-II<sup>2)</sup> and ENDF/B-IV<sup>3)</sup>.

Effective Multiplication Factors : Table 1.1.1

JENDL-2B gives  $\bar{k}_{\text{eff}} = 0.998$  with standard deviation of 0.65 %. The discrepancy between the Pu cores and the U cores is 0.2 % and smaller than those with JENDL-1 and ENDF/B-IV.

Central Reaction Rate Ratios : Table 1.1.2

The ratio of  $^{238}\text{U}$  fission to  $^{235}\text{U}$  fission is overestimated by 6 % on an average. It should be noted, however, that the C/E values of some assemblies much deviate from unity with any library set. The experimental condition should be checked more carefully for such cases, since the fission rate of fertile material such as  $^{238}\text{U}$  is very sensitive to the detector position in the cell. We believe that the C/E values of JENDL-2B are not so much overestimated, eliminating such extreme cases. The ratio of  $^{239}\text{Pu}$  fission to  $^{235}\text{U}$  fission is underestimated by 1.2 % but is 1.5 % higher than JENDL-1. The C/E values are satisfactory for both the ratios of  $^{238}\text{U}$  capture to  $^{235}\text{U}$  fission and of  $^{238}\text{U}$  capture to  $^{239}\text{Pu}$  fission.

## Central Reactivity Worths : Table 1.1.3

In order to avoid the scaling problem, both calculated and measured reactivity worths were normalized to those of  $^{239}\text{Pu}$ , respectively. The C/E values of the normalized worth were compared in Table 1.1.3. The results of JENDL-2B are satisfactory for  $^{235}\text{U}$  and  $^{238}\text{U}$ , while the worths were a little overestimated with JENDL-1. The worth of  $^{10}\text{B}$  obtained from JENDL-2B is underestimated by 9 % and becomes 3.5 % lower than that from JENDL-1. This difference is caused by the core neutron spectrum, because the cross sections of JENDL-1 were used for  $^{10}\text{B}$ .

## Doppler Coefficients : Table 1.1.4

Doppler coefficients are very satisfactorily predicted with JENDL-2B, while JENDL-1 overestimates them by 10 % and JAERI-Fast-II underestimates them by 10 %.

## Discussion and Concluding Remarks

JENDL-2B predicts various characteristics of fast reactors better than JENDL-1 as a whole. It is now used in the analyses of the JUPITER project. However, the following problems have been pointed out. The overestimate in the ratio of  $^{238}\text{U}$  fission to  $^{235}\text{U}$  fission suggests that the neutron flux is overestimated in MeV region with JENDL-2B. On the contrary, the slight underestimate in the fission rate ratio of  $^{239}\text{Pu}$  to  $^{235}\text{U}$  implies some underestimate of the flux in the energy region above 100 keV, because the microscopic fission cross section ratio hardly seems to be underestimated. From the underestimate of  $^{10}\text{B}$  worth, the underestimate of the flux in low energy region is suggested, though satisfactory results in Doppler coefficients implies the well-prediction of low energy spectrum. In order to investigate this apparently inconsistent suggestion on the neutron spectrum, the effects of the fission spectrum and the inelastic scattering cross section of  $^{238}\text{U}$  should be investigated by a sensitivity analysis.

## References

- 1) Kikuchi, Y., et al.: Paper ED-9, Int. Conf. Nuclear Cross Sections for Technology, Knoxville, 1979.
- 2) Takano, H., et al.: JAERI Fast Reactor Group Constants Set, Version II", JAERI-1255 (1978).
- 3) Hardie, R. W., Schenter, R. E., Wilson, R. E.: Nucl. Sci. Eng., 57, 222 (1975).

Table 1.1.1 Effective Multiplication Factors.

No. of Cores	*	JENDL-2B	JENDL-1	JAERI-Fast-II	ENDF/B-IV**
Pu cores 16 (11)	A	0.9971	0.9978	1.0019	0.9972
	B	0.0049	0.0074	0.0044	0.0047
U cores 10 (6)	A	0.9992	1.0067	1.0033	1.0038
	B	0.0082	0.0077	0.0100	0.0059
All cores 26 (17)	A	0.9979	1.0012	1.0024	0.9993
	B	0.0065	0.0086	0.0072	0.0060

\* A: Average of C/E, B: Standard Deviation.

\*\* The values are taken from Ref. (3) for assemblies whose numbers are given in parentheses in the first column.

Table 1.1.2 Central Reaction Rate Ratios.

Quantities	No. of Cores	*	JENDL-2B	JENDL-1	JAERI -Fast-II	ENDF/B-IV**
<u>U-238 Fission</u> <u>U-235 Fission</u>	Pu cores 15 (11)	A	1.086	1.008	1.021	1.019
		B	0.081	0.075	0.072	0.076
	U cores 10 (6)	A	1.024	0.960	1.011	1.046
		B	0.074	0.071	0.076	0.076
	All cores 25 (17)	A	1.061	0.988	1.017	1.029
		B	0.084	0.077	0.074	0.077
<u>Pu-239 Fission</u> <u>U-235 Fission</u>	Pu cores 15 (11)	A	0.980	0.964	0.974	0.982
		B	0.032	0.031	0.031	0.036
	U cores 9 (5)	A	1.005	0.987	1.001	1.014
		B	0.055	0.058	0.058	0.026
	All cores 24 (16)	A	0.988	0.973	0.984	0.992
		B	0.044	0.045	0.045	0.036
<u>Pu-240 Fission</u> <u>U-235 Fission</u>	All cores 13 (11)	A	1.064	1.009	1.059	1.074
		B	0.126	0.115	0.105	0.116
<u>U-238 Capture</u> <u>U-235 Fission</u>	All cores 13 (10)	A	0.990	0.984	0.982	0.975
		B	0.032	0.030	0.031	0.040
<u>U-238 Capture</u> <u>Pu-239 Fission</u>	All cores 12 (9)	A	1.003	1.012	0.999	0.976
		B	0.047	0.046	0.045	0.064

\* A: Average of C/E, B: Standard Deviation of C/E.

\*\* The values are taken from Ref. (3). The numbers of assemblies are given in parentheses in column 2.

Table 1.1.3 Sample Worths Normalized to Those of  $^{239}\text{Pu}$ .

Sample	No. of Cores	*	JENDL-2B	JENDL-1	JAERI-Fast-II	ENDF/B-IV**
$^{235}\text{U}$	18	A B	1.007 0.058	1.037 0.072	1.005 0.058	1.014 0.060
$^{238}\text{U}$	17	A B	1.033 0.263	1.092 0.226	1.011 0.129	0.950 0.130
$^{10}\text{B}$	16	A B	0.909 0.143	0.944 0.122	0.928 0.120	0.836 0.115
Cr	10	A B	1.046 0.131	0.968 0.170	1.309 0.333	1.359 0.205
Fe	13	A B	0.979 0.156	0.905 0.150	1.018 0.130	1.109 0.275
Ni	11	A B	1.217 0.274	1.136 0.243	1.153 0.217	1.167 0.196

\* A: Average of C/E, B: Standard Deviation of C/E.

\*\* Taken from Ref. (3)

Table 1.1.4 Doppler Reactivity Coefficients (C/E).

		JENDL-2B	JENDL-1	JAERI-Fast-II
Small Sample Doppler Experiments	FCA V -1	0.96	1.09	0.78
	V -2	0.86	0.98	0.74
	VI-1	1.00	1.13	0.94
	VI-2	0.93	1.03	0.90
	ZPPR-2 (Normal)	1.13	1.25	1.08
	(Na voided)	0.85	0.96	0.81
	ZPR-3-47	0.97	1.04	0.95
Whole Core Doppler Experiment	SEFOR	1.05	1.12	1.05
Average of C/E		0.97	1.08	0.91
Standard Deviation of C/E		0.09	0.09	0.12

## 1.2 JFS-3: Group Constants Library Produced with the Group Structure of GAM-Type

H. Takano, K. Kaneko\* and H. Inoue\*

The group constant library for fast reactor calculation was produced by using the processing codes TIMS-1<sup>1)</sup> and PROF. GROUCH.G-II<sup>2)</sup> from the evaluated nuclear data files JENDL-1<sup>3)</sup>, -2<sup>4)</sup> and ENDF/B-IV<sup>5)</sup>. This library is called JFS-3. The JFS-3 differs from the JAERI-Fast set version II (JFS-2)<sup>6)</sup> as to the concepts of group constants as follows:

- (1) The group structure is the GAM-type in which the energy range from 10 MeV to 0.3224 eV is divided into 69 groups with equal lethargy width of 0.25 and the range below 0.3224 eV is a thermal group.
- (2) The group average cross sections are calculated with the REMO-correction method<sup>7)</sup>, for which the weighting spectrum is the collision density at core center in a typical fast reactor.
- (3) The self-shielding factor tables are given four temperatures 300, 800, 2100 and 4500 °K, eight admixture background cross sections  $\sigma_0 = 0, 1, 10, 10^2, 10^3, 10^4, 10^5$  and  $10^6$  barns and mutual shielding parameters<sup>6)</sup>.
- (4) The self-shielding factors of inelastic scattering cross sections are calculated. Especially, this shielding effect is important for iron.
- (5) The temperature dependent self-shielding factors for structural materials Fe, Cr and Ni are calculated.
- (6) The neutron group to group transfer materials are being expanded to P<sub>3</sub>.

The present JFS-3 library contains twenty-six nuclides shown in Table 1.2.1. The group constants for these nuclides are processed with both the REMO and standard  $(x + 1/E)$  weighting spectra. Using the JFS-3, the effects of the REMO-correction on the effective multiplication factor and neutron spectra are studied by performing the benchmark test<sup>6)</sup>.

Table 1.2.2 shows the comparison between the effective multiplication factors calculated by using the REMO and standard weighting methods. The effect of the REMO-correction on  $k_{eff}$  is small, but the effect seems

---

\* Japan Information Service Co. Ltd., Tokyo.

Table 1.2.1 Nuclides contained in the present JFS-3 library

	Nuclide	Nuclear data	No. of $\sigma_0$	No. of Temperatures
1	U-235	JENDL-2, ENDF/B-IV	8	4
2	U-238	JENDL-2, "	8	4
3	Pu-239	JENDL-2, "	8	4
4	Pu-240	JENDL-2, "	8	4
5	Pu-241	JENDL-2, "	8	4
6	U-234	JENDL-1, "	8	4
7	Th-232	JENDL-1, "	8	4
8	Am-241	JENDL-1, "	8	1
9	Ni	JENDL-2, "	8	4
10	Cr	JENDL-2, "	8	4
11	Fe	JENDL-2, "	8	4
12	Mo	JENDL-1, "	8	1
13	Cu	JENDL-1, "	8	1
14	Mn	JENDL-1, "	8	1
15	Si	JENDL-1, "	8	1
16	Al	JENDL-1, "	8	1
17	Na	JENDL-1, "	8	1
18	C	JENDL-1, "	8	1
19	B-10	JENDL-1, "	8	1
20	H-1	JENDL-1, "	8	1
21	U-233	ENDF/B-IV	8	4
22	U-236	ENDF/B-IV	8	4
23	Pu-242	ENDF/B-IV	8	4
24	Be	ENDF/B-IV	8	1
25	B-11	ENDF/B-IV	8	1
26	O	ENDF/B-IV	8	1



about 0.15 % for prototype assemblies such as MZB. The neutron spectra at core center in MZB are compared in Fig. 1.2.1. The spectrum becomes harder by the REMO-correction, because the elastic removal scattering cross sections become smaller than those calculated with the standard weighting spectrum.

At the present time, many analyses for fast reactor assemblies are performed by using the JFS-3 library. These results will be reported in the near future.

The present work was performed under the contracts between Power Reactor and Nuclear Fuel Development Corporation and Japan Atomic Energy Research Institute.

#### References

- 1) Takano H., Ishiguro Y. and Matsui Y.: "TIMS-1: A Processing Code for Production of Group Constants of Heavy Resonant Nuclei", JAERI 1267 (1980).
- 2) Hasegawa A., et al.: to be published.
- 3) Igarashi S., et al.: "Japanese Evaluated Nuclear Data Library, Version-1, JENDL-1", JAERI 1261 (1979).
- 4) Igarashi S., et al.: to be published.
- 5) "ENDF/B data file, BNL-NCS-17541 (ENDF-201), 2nd Edition (ENDF/B-IV), edited by D. GARBER (1975)".
- 6) Takano H., et al.: "JAERI Fast Reactor Group Constants Set, Version II", JAERI 1255 (1978).

Table 1.2.2 Comparison of effective multiplication factors calculated with the standard and REMO weighting spectra

Assembly	Standard	REMO	Assembly	Standard	REMO
VERA-11A	0.99445	0.99487	ZPPR-2	1.00213	1.00302
ZEBRA-3	0.99988	1.00153	MZA	0.99774	0.99869
SNEAK-7A	1.00654	1.00667	MZB(1)	0.99400	0.99537
ZPR-3-54	0.95742	0.95412	FCA-5-2	0.99125	0.99052
ZPR-3-53	0.99562	0.99284	VERA-1B	1.00151	0.99990
SNEAK-7B	1.00410	1.00602	ZPR-3-6F	1.01379	1.01377
ZPR-3-50	1.00270	1.00134	ZPR-3-12	1.00759	1.00717
ZPR-3-48	1.00449	1.00482	ZPR-3-11	1.00402	1.00475
ZPR-3-49	1.00946	1.01048	ZEBRA-2	0.99559	0.99411
ZPR3-56B	0.98969	0.99220	ZPR-6-6A	1.00879	1.00549
ZPR-6-7	0.99506	0.99607	Average	0.99885	0.99875

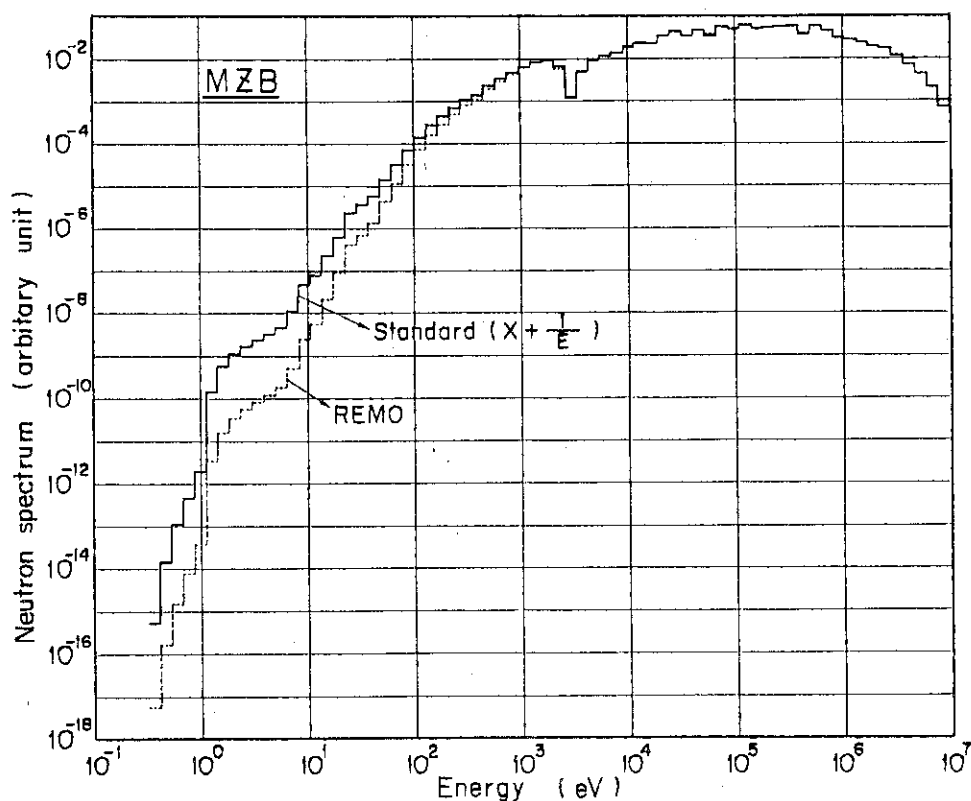


Fig. 1.2.1 Neutron spectra at core center; ----REMO, — Standard

### 1.3 Production of Group-Constants Library for the PALLAS-type Transport Codes with Direct Integration

Y. Ishiguro, T. Suzuki and Y. Matsui\*

A numerical method was developed for solving the transport equation in attenuating media on the basis of the direct integration method along the path traveled by neutrons<sup>1)</sup>. This method can formally give an exact solution to the neutron and/or  $\gamma$ -ray transport problems. The two codes, PALLAS<sup>2)</sup> and PALLAS-2DCY-FC,<sup>3)</sup> have been developed, respectively, for one- and two-dimensional transport problems, and their revising works have been in progress. Recently, another new version to the PALLAS series codes has been developed to improve the energy-angular correlation in the slowing-down source terms (PALLAS-TS code).<sup>4)</sup>

For the purpose of the production of a group constants library for the above mentioned PALLAS-type codes, the PROF GROUCH-GII code<sup>5)</sup> has been revised. The main revising point was put on the calculation of the average Legendre coefficients of the neutron angular distributions for elastic and inelastic scatterings. No special attention was however paid to the weighting function used for the averaging process under the assumption of finer lethargy and angular meshes and of smooth variation with energy of the angular distributions. The resonance shielding was completely neglected since the primary object of the library production was to be directed to the application to blanket neutron physics of fusion reactor.

A library of the 120 group constants has been produced, by the use of the revised PROF-GROUCH-GII code, for the twenty-nine nuclides from the ENDF/B-IV nuclear data file<sup>6)</sup>, as shown in Table 1.3.1. The general information and the group structure used are shown in Table 1.3.2 and 3, respectively. This library consists of the two files as follows:

#### (I) The first file

(I)-1 the first record (1771 words)

EUP(121), EMID(120), DELU(120), CHI(120), NCODEL(30), AW(30),  
LEVEL(30), Q(30,40)

---

\* Japan Information Service Co. Ltd., Tokyo

EUP : Upper energy of group  
 EMID : Mid-energy of group corresponding to the middle point of lethargy  
 DELU : Lethargy width of group  
 NCODEL: Code number of nuclide  
 AW : Atomic weight of nuclide  
 LEVEL : The number of inelastic scattering levels plus 1  
 Q : Q-value

(I)-2 from the second to the 121-th records (3720 words  $\times$  120)

[ I=1, 120  
   SST(30), SSFNU(30), SSF(30), SSC(30), SSO(120,30)  
 SST : Total cross section of nuclide (m) for group i  $\sigma_t^{mi}$   
 SSFNU :  $(v\sigma_f)^{mi}$   
 SSF :  $\sigma_f^{mi}$   
 SSC :  $\sigma_c^{mi}$   
 SSO :  $\sigma_s^{m,i \rightarrow i+j-1}$

(II) The second file (3600 records)

[ I=1, 120  
   [ M=1, 30  
     [ LVL, (NLV(M,L), SSL(M,L), (FL(M,J,L),  
       J=1, NLV(M,L)), L=1, LVL)  
 LVL : The total number of elastic and inelastic scattering levels  
 NLV : The order of Legendre expansion for the L-th level  
 SSL : The excitation cross section of the L-th level  
 FL : The average Legendre expansion coefficient of the L-th level  
 (Dummy record was inserted for M=30).

#### References

- 1) Takeuchi, K.: J. Nucl. Sci. Technol. 8, 141 (1971).
- 2) Takeuchi, K.: Report of Ship Research Institute, 9, 6 (1972)  
(in Japanese).
- 3) Takeuchi, K.: in Papers of Ship Research Institute No.57 (1979).
- 4) Suzuki, T.: to be published.
- 5) Hasegawa, A.: to be published.
- 6) ENDF/B Summary Document, BNL-17541 (ENDF-201), 2nd Edition, compiled by D. Garber (1975).

Table 1.3.1 List of nuclides cited from ENDF/B-IV nuclear data file

Material	MAT(MOD)	Authors	Institution
H	1969(2)	L. Stewart, R.J. Labauve and P.G. Young	LASL
D	1120(0)	B.R. Leonard and K.B. Stewart	BNW
T	1169(1)	Leona Stewart	LASL
Li-6*	1271(0)	G.M. Hale, D. Dodder and P. Young	LASL
Li-7*	1272(0)	R.J. Labouve, L. Stewart and M. Battat	LASL
Be-9	1289(2)	R.J. Howerton and Perkins	LLL
B-10	1293(0)	G.M. Hale, R.A. Nisley and P.G. Young	GE-BNL
B-11	1160(0)	C. Cowan	GE-BNL
C-12	1274(0)	F.G. Perey and C.Y. Fu	ORNL
N-14	1275(4)	P. Young, D. Foster, Jr. and G. Hale	LASL
O-16	1276(2)	P. Young, D. FASTER, Jr. and G. Hale	LASL
Na-23	1156(0)	N.C. Paik and Pitterle	WARD-ORNL
Al-27	1193(3)	P.G. Young and D.G. FASTER, Jr.	LASL
Cr	1191(0)	A. Prince	BNL(NNCSC)
Mn	1197(0)	H. Takahashi	BNL
Fe	1192(0)	F.G. Perey, C.Y. Fu, W.E. Kinney and R.Q. Wright	ORNL
Ni	1190(0)	M.R. Bhat	BNL(NNCSC)
Cu	1295(1)	M.K. Drake and F.P. Fricke	SAI
Zr-2	1284(0)	B.R. Leonard, Jr.	BNW
Mo	1287(0)	R.J. Howerton	LLL
Pb	1288(5)	C.Y. Fu and F.G. Perey	ORNL
Th-233	1296(0)	Wittkoph, Rog and Livolsi	BAW
U-233	1260(0)	N.M. Steen	BAPL
U-235	1261(0)	L. Stewart, H. Alter and R. Hunter	LASL, AI
U-238	1262(0)	N.C. Paik	WARD
Pu-239	1264(0)	B.A. Hutchins, H. Hunter, L. Stewart and R. Labauve	LASL
Pu-240	1265(0)	E. Pennington and H. Hummel	ANL
Pu-241	1266(0)	H. Hummel and E. Pennington	ANL
Pu-242	1161(0)	H. Alter and Dunford	AI, ANC

Table 1.3.2 General information

MATERIAL	MAT NO.	(FILE NO.)	CODE NO.	ATOMIC MASS
HYDROGEN	1269	(404)	11	1.0000
DEUTERIUM	1120	(402)	12	1.9970
TRITIUM	1169	(401)	13	2.9901
LITHIUM-6	1271	(404)	36	5.9634
LITHIUM-7	1272	(404)	37	6.9557
BERYLLIUM	1289	(404)	40	8.9348
BORON-10	1273	(404)	50	9.9269
BORON-11	1160	(403)	51	10.9150
CARBON	1274	(408)	60	11.8969
NITROGEN	1275	(408)	70	13.8830
OXYGEN	1276	(408)	80	15.8580
SODIUM	1156	(403)	110	22.7923
ALUMINIUM	1193	(405)	130	26.7500
CHROMIUM	1191	(406)	240	51.5490
MANGANESE	1197	(409)	250	54.4661
IRON	1192	(406)	260	55.3650
NICKEL	1190	(406)	280	58.1826
COPPER	1295	(410)	290	62.9940
ZIRCONIUM-2	1284	(411)	400	90.4360
MOLYBDENUM	1287	(409)	420	95.1160
LEAD	1288	(408)	820	205.4300
THORIUM-232	1296	(404)	902	230.0400
URANIUM-233	1260	(409)	923	231.0430
URANIUM-235	1261	(407)	925	233.0250
URANIUM-238	1262	(409)	928	236.0060
PLUTONIUM-239	1264	(407)	949	236.9990
plutonium-240	1265	(407)	940	237.9920
PLUTONIUM-241	1266	(407)	941	238.9780
PLUTONIUM-242	1161	(404)	942	240.1450
L.F.P. (PU-239)	0	( 0)	0	0.0

Table 1.3.3 Group structure

Group No.	Upper energy (eV)	Lethargy width
1	$1.648 \times 10^7$	0.0625
	↓	
44	$1.122 \times 10^6$	
45	$1.054 \times 10^6$	0.125
	↓	
76	$2.186 \times 10^4$	
77	$1.931 \times 10^4$	0.25
	↓	
120	$4.140 \times 10^{-1}$	

## 1.4 Self-Shielding Effect of Inelastic Scattering Cross Section of Iron on Neutron Spectrum

H. Takano and K. Kaneko\*

The multigroup transport or diffusion calculations are often based on the concept of multigroup constants set such as the ABBN<sup>1)</sup>, JFS-II<sup>2)</sup> or LIB-IV<sup>3)</sup>. In these sets, the effective cross sections are calculated by multiplying self-shielding factors to infinitely dilute cross sections. For inelastic scattering cross sections, however, the self-shielding effect was neglected by assuming small energy variation of the cross sections. This assumption will be valid, except for iron of which the energy fluctuations for inelastic scattering and total cross sections are seen remarkably below about 2 MeV from the evaluation data, for example, of Garber and Kinsey<sup>4)</sup>.

In fast reactor, the iron is a very important structural and/or reflector material. On the other hand, the energy range below 2 MeV where the iron inelastic scattering cross sections strongly fluctuate, is the main part of neutron spectrum in fast reactor. In this paper, the influence of the inelastic scattering self-shielding on neutron spectra was studied for the assemblies ZPR-3-54 and MZB with steel reflector.

ZPR-3-54: This assembly is composed of Pu-fueled core and steel reflector. The neutron spectra were calculated by using one-dimensional diffusion theory with spherical model. The effect of the inelastic scattering self-shielding on the neutron spectrum at the centre core was negligibly too small to be distinguished. As seen from Fig. 1.4.1, however, the neutron spectrum considerably varies in the steel reflector, that is, the spectrum becomes harder by decrease of the slowing down power.

The radial reaction rate distributions were calculated and the effect of the self-shielding on them was studied. The reaction rates were normalized to that at the centre core. Figure 1.4.2 shows the ratios of the reaction rates calculated with and without considering the self-shielding effect. As seen from this figure, the reaction rate distribution of  $^{239}\text{Pu}$  becomes smaller by about 1 % in the vicinity of the boundary

---

\* Japan Information Service Co. Ltd., Tokyo.

between the core and reflector and 8 % at the edge of the reflector. On the other hand, the reaction rate of  $^{238}\sigma_f$  becomes large by about 5 % in the reflector, because of the hardening spectrum.

MZB: This is the fast critical assembly for the Japan proto-type fast reactor "MONJU" mock-up in the MOZART programme. One-dimensional diffusion calculation was performed with the cylindrical geometry composed of the inner core, outer core, blanket and reflector. The inelastic scattering self-shielding effect produces again a hardening spectrum, similarly in the case of ZPR-3-54. Figure 1.4.3 shows the ratios of the reaction rates calculated with and without the self-shielding effect. The reaction rate of  $^{235}\sigma_f$  becomes smaller by about 3 % in the reflector. The same tendency was also seen for the reaction rate distributions of  $^{239}\sigma_f$ ,  $^{235}\sigma_c$  and  $^{238}\sigma_c$ , while the reaction rate distribution for  $^{238}\sigma_f$  became larger due to the spectrum-hardening.

The inelastic scattering self-shielding effect of iron produced a harder neutron spectrum because of decreasing the slowing down power. Especially, the effect on the neutron spectrum was considerably distinguished in steel reflector. Hence, the inelastic scattering self-shielding of iron should be considered in the reactor shield calculation and/or analysis of neutron spectrum experiments in the iron assembly.

#### References

- 1) Abagjan, L.P., et al.: "Group Constants for Nuclear Reactor Calculation", Consultant Bureau, New York (1964).
- 2) Takano, H., et al.: "JAERI Fast Reactor Group Constants Set, Version II", JAERI-1255 (1978).
- 3) Kidman, R.B. and Macfarlane, R.E.: "LIB-IV: A Library of Group Constants for Nuclear Reactor Calculations", LA-6260-MS, 1976.
- 4) Garber, D.I. AND Kinsey, R.R.: "Neutron Cross Sections Volume II, Curves", BNL 325, 3rd ed., Vol.II, 1976.



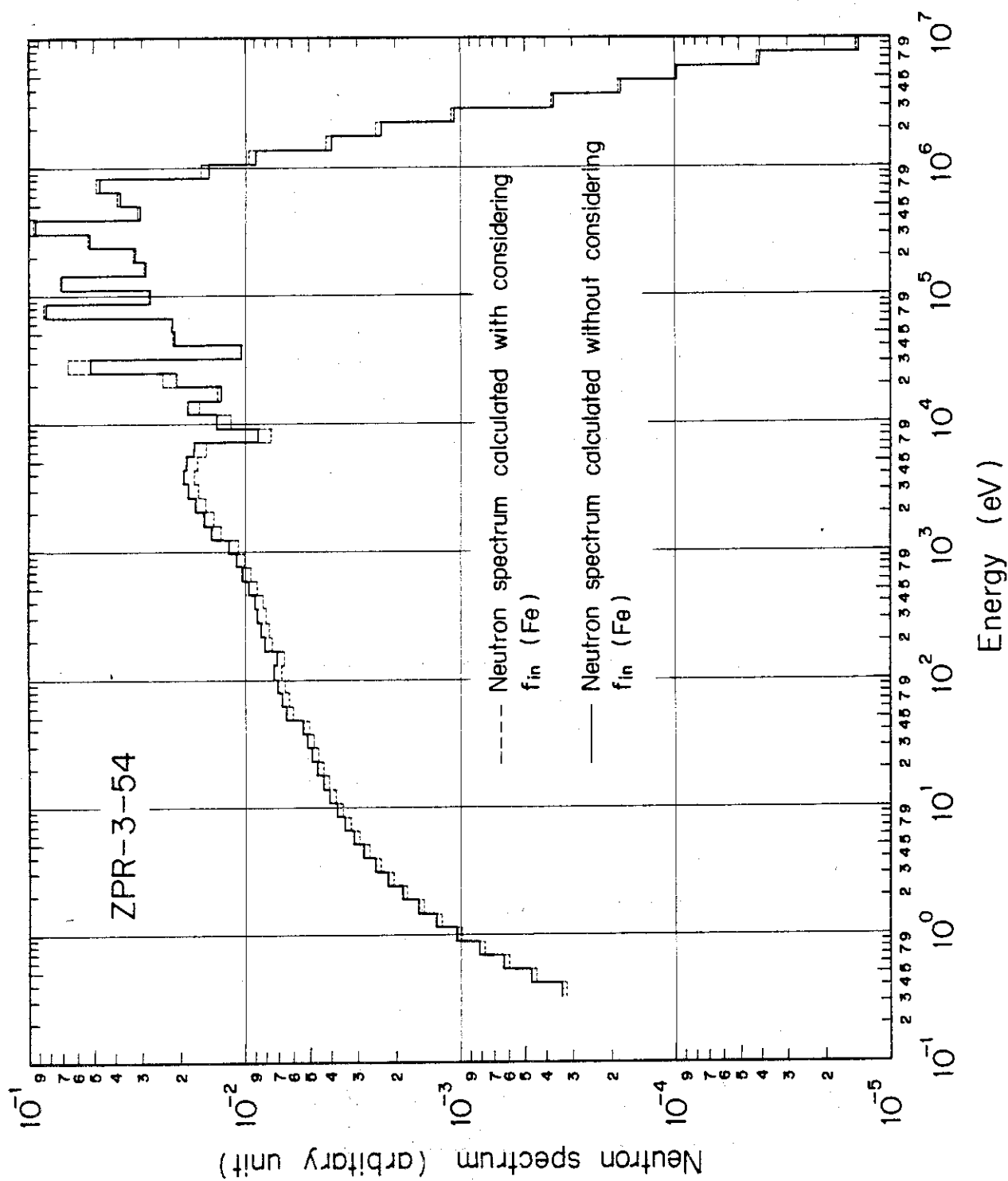


Fig. 1.4.1 Effect of inelastic scattering self-shielding on neutron spectra at the outer edge of the reflector in ZPR-3-54.

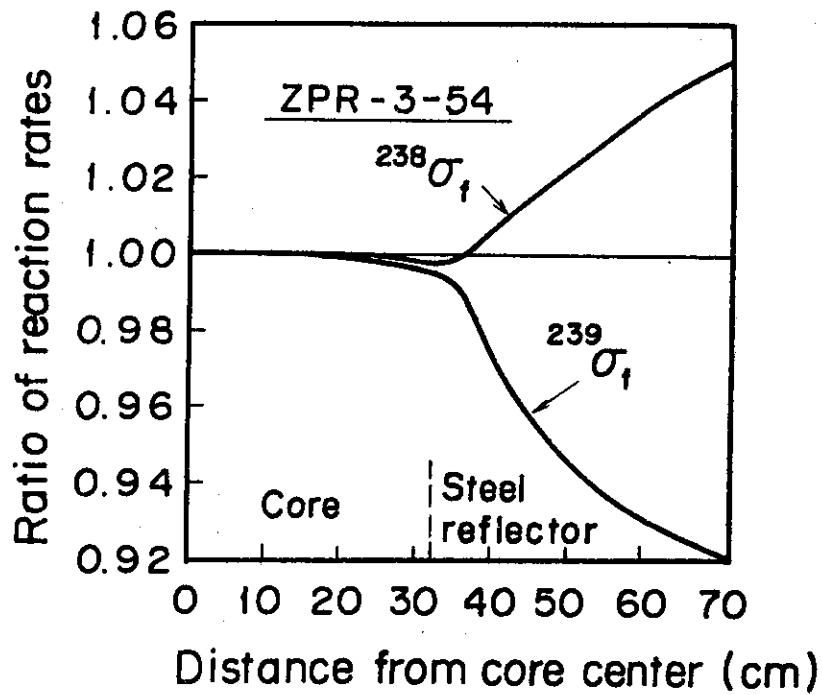


Fig. 1.4.2 Ratio of reaction rates for  $^{239}\sigma_f$  and  $^{238}\sigma_f$  Calculated with and without considering the self-shielding effect in ZPR-3-54.

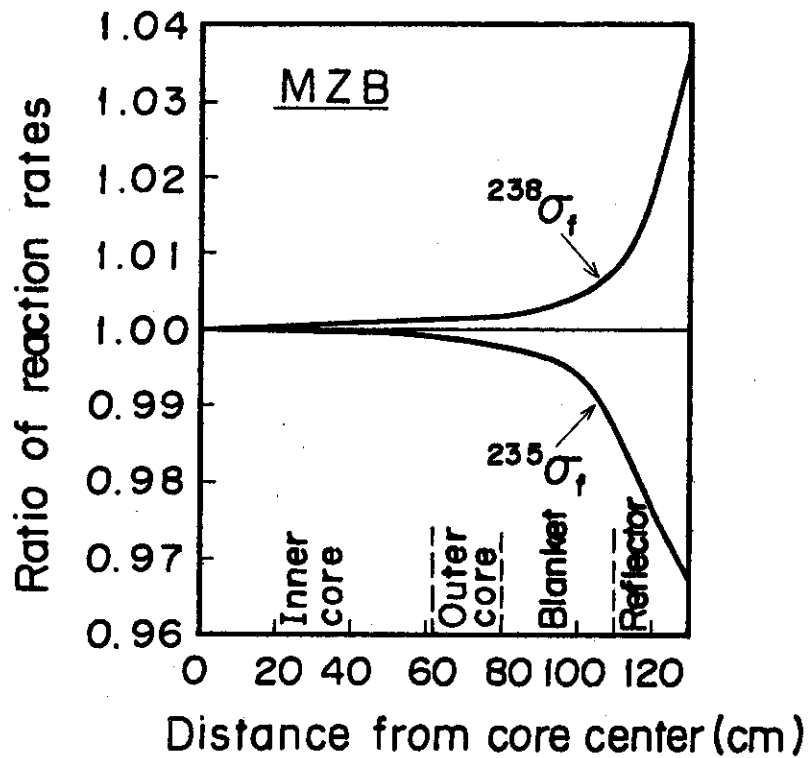


Fig. 1.4.3 Ratio of reaction rates for  $^{235}\sigma_f$  and  $^{238}\sigma_f$  calculated with and without considering the self-shielding effect in MZB.

## 1.5 Calculation of Nuclide Yields Produced by High Energy Proton Spallation Reactions

Y. Nakahara and T. Tsutsui

Concepts of accelerator breeding of fissile materials and transmutation of actinides and fission products have been investigated in USA, Canada and USSR. The most essential parameter is the number of neutrons from the spallation and fission reactions in the target/blanket triggered by the high energy proton beam from a linear accelerator.

Recently the theoretical and computational models have been examined by making a comparison of neutron yields and  $^{239}\text{Pu}$  distributions with the experiments by Vasil'kov et al. at JINR (USSR)<sup>1),2)</sup>. When the transmutations of actinides and fission products are to be investigated, the yields of product nuclides are to be predicted with reasonable accuracies.

A preliminary study of the spallation products has been performed with the use of the Monte Carlo code NMTC developed at ORNL, revised at BNL and JAERI. The target/blanket system is the Vasil'kov et al.'s, as used in Refs. (1) and (2). Computational results are shown in Figs. 1.5.1 and 1.5.2 for the incident proton energy of 1,500 MeV. It should be noticed that the contributions from the reactions below 15 MeV are not included entirely and the fission reactions above 15 MeV are not taken into consideration also. Shaded columns indicate the radioactive nuclides with relatively long half lives. The quantities in the kg/y unit are calculated for the 300 mA proton and full 365 days. It is seen in Fig. 1.5.1 that  $^{205}\text{Pb}$  with the half life of  $1.4 \times 10^7$  years is the main hazardous product.

### References

- 1)\* Nakahara Y., Takahashi H.: Atomnaya Energiya, 83, 47 (1979) (in Russian).
- 2) Takahashi H., Nakahara Y.: International Conf. on Nucl. Cross Sections for Tech., October, 1979, Knoxville.

---

\* Most of these works were performed during Nakahara's stay at BNL. Acknowledgements are due to Dr. H. Takahashi (BNL).

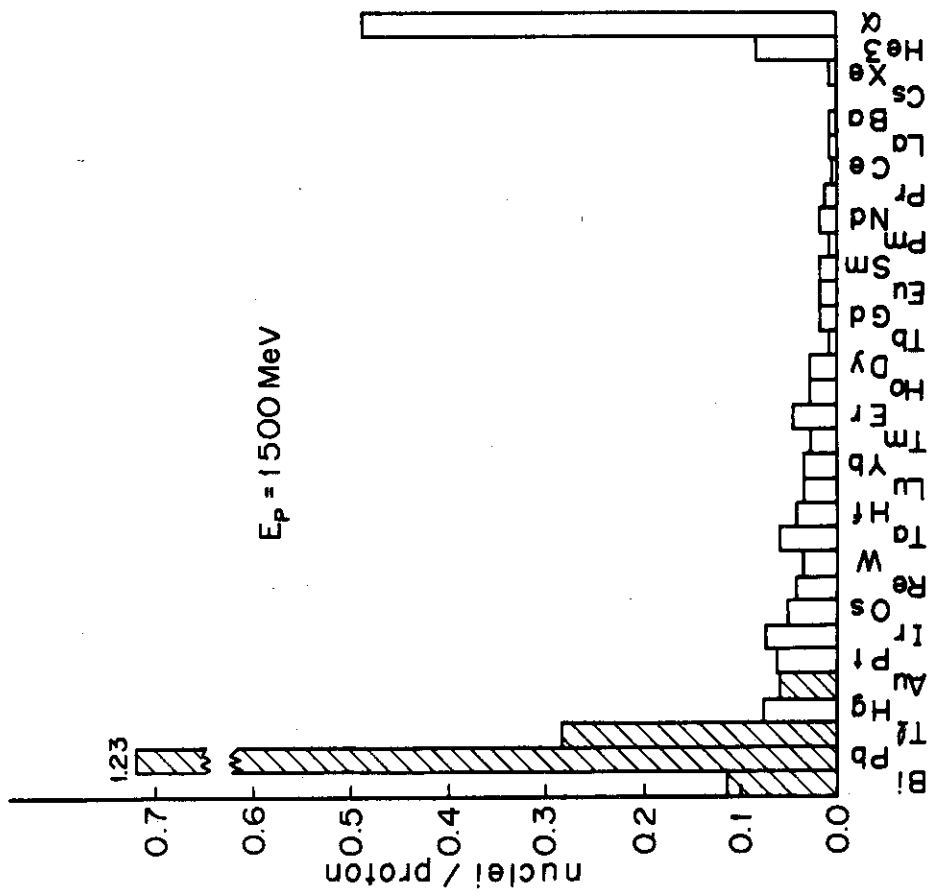


Fig. 1.5.2 Spallation products in the Pb target  
Shaded columns contain radioactive nuclides such as

Bi-205 (15.31 days)	Tl-202 (12.23 days)
-206 (6.243 days)	-204 (3.77 years)
-207 (38 years)	Au-195 (184 years)
Pb-202 ( $3 \times 10^5$ years)	
-205 ( $1.4 \times 10^7$ years)	

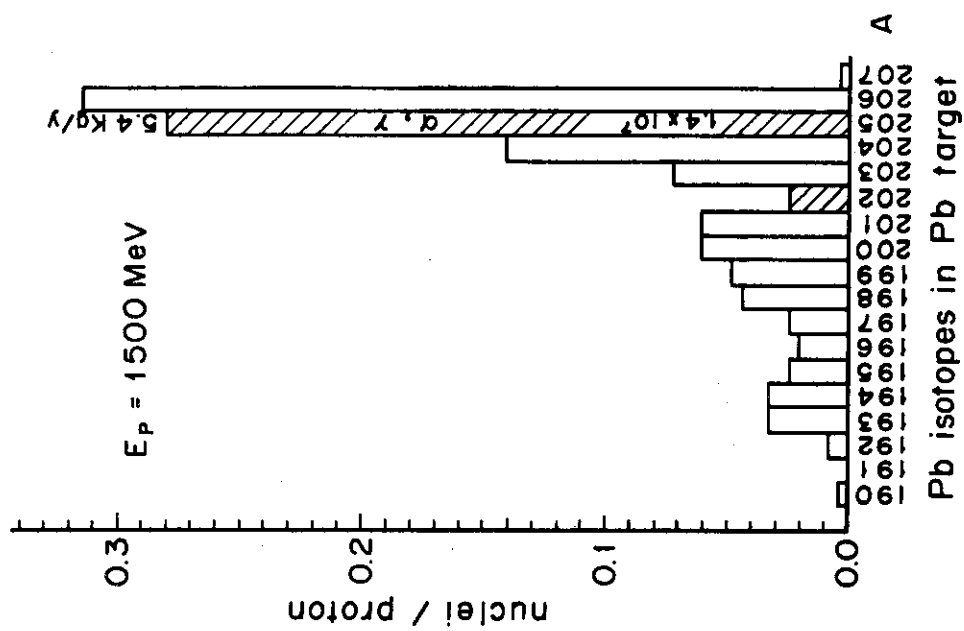


Fig. 1.5.1 Spallation of Pb isotope products  
in the Pb target

## 2. Theoretical Methods and Code Development

### 2.1 SRAC: A Standard Computer Code System for Lattice Cell and Core Calculations on Reactor Design and Analysis

K. Tsuchihashi, Y. Ishiguro, H. Takano, Y. Onuma, K. Kaneko\*  
and T. Hara\*\*

A code system SRAC is being developed as the nuclear design and analysis part of the JAERI standard thermal Reactor Code System, which aims to supply the standard means and data for reactor design and analysis and to present the standard values with high accuracy to the calculational methods used so far.

The SRAC is intended to accept the requirements, as much as possible, from the experimental analysis of the several type of the critical facilities at JAERI, the detailed core design for the modification of JAERI Research Reactors and also the safety analysis of light water reactors.

The SRAC system is designed to allow a variety of usages described as follows:

1) The fundamental group constant library has been produced from the ENDF/B-IV nuclear data file with the energy group structure of 107 groups (45 groups for thermal and 74 for fast energy ranges, respectively, with 12 groups overlapping). The library holds the Bondarenko type table for resonance shielding factors and keeps, additionally, the resonance parameters on the energy range between 130.7 to 0.4 eV for the optional use of the intermediate resonance approximation<sup>2),3)</sup> or the rigorous calculations using the collision probability method<sup>4)</sup>.

The thermal group-to-group transfer matrices are compiled on the ten assigned temperatures, whereas the interpolation for arbitrary temperature is not yet available.

2) The user must construct his own library from the fundamental library for the desired nuclei and temperatures with his own energy group structure, where the thermal cut off energy is also chosen from the

---

\* Japan Information Service Co., Tokyo.

\*\* Information System Laboratory Co., Tokyo.

overlapping energy range.

- 3) As shown in Fig. 2.1.1, the SRAC system can solve the fixed source problem in the partial energy range, which is mainly used for cell calculation, and can also solve the eigenvalue problem in the whole energy range which is used in cell and/or core calculation.
- 4) A variety of the transport codes are available for cell calculations (collision probability method with 14 type of geometries<sup>5)</sup>, 1D-SN<sup>6)</sup>, 2D-SN<sup>7)</sup>). The one space-point solution by  $B_1$  or  $P_1$  approximation<sup>8)</sup> is also available after smearing the cross sections.
- 5) For core calculations, the above mentioned transport codes and the 1-, 2- and 3-D<sup>9)</sup> diffusion codes are available.
- 6) Smearing and/or collapsing of macroscopic cross sections is done separately by the user's selection.
- 7) Double heterogeneity such as the grain effect in the burnable poison rod or the pin rod in a channel box can be treated by utilizing smeared cross sections obtained from homogenizing the microscopic heterogeneity into the macroscopic heterogeneity.
- 8) The several PDS (Partitioned Data Set) files are used for the data storage. The built-in FACOM utility program is used for the file control (LIST DIRECTORY, DELETE, CONDENSE, COPY, RENAME), and a few service programs are ready to read/write the contents of these files.

An informal working group is set up at the Tokai Establishment in order to debug the code system, to improve the I/O and to urge its usage. Moreover, the benchmark test will be done to assess the performance and the prediction accuracy in near future.

#### Reference

- 1) ENDF/B Summary Documentation, BNL-NCS-17541 (ENDF-201), 2nd Edition, Compiled by D. Garber, available from the National Nuclear Data Center, BNL, Upton, N.Y. (1975).

- 2) Ishiguro, Y. and Takano, H.: "Intermediate Neutron Resonance Absorption with Interference Scattering in heterogeneous systems", J. Nucl. Sci. Technol., 6 380 (1969).
- 3) Tsuchihashi, K., Ishiguro, Y. and Kaneko, K.: "Resonance Absorption in High-Temperature Gas-Cooled Reactor Fuel with Double Heterogeneity", Nucl. Sci. Eng., 74, 164 (1979).
- 4) Ishiguro, Y.: "PEACO-II: A Code for Calculation of Effective Cross Sections in Heterogeneous Systems, JAERI-M 5527 (1974).
- 5) Tsuchihashi, K.: "LAMP-B: A Fortran Program Set for the Lattice Cell Analysis by Collision Probability Method", JAERI 1259 (1979).
- 6) Engle, Jr, W.W.: "A User's Manual for ANISN", K-1693 (1967).
- 7) LATHROP, K.D. and Brinkly, F.w.: "Theory and Use of the General Geometry TWOTRAN Program", LA-4432 (1970).
- 8) Durek, J.S. et al.: "GAM-I: A Consistent P Multigroup Code for the Calculation of Fast Neutron Spectra and Multigroup Constants", GA-1850 (1961).
- 9) Fowler, T.B. et al.: CITATION: ORNL-TM-2496 (1969)..
- 10) Asai, K.: Private Communication (1974).

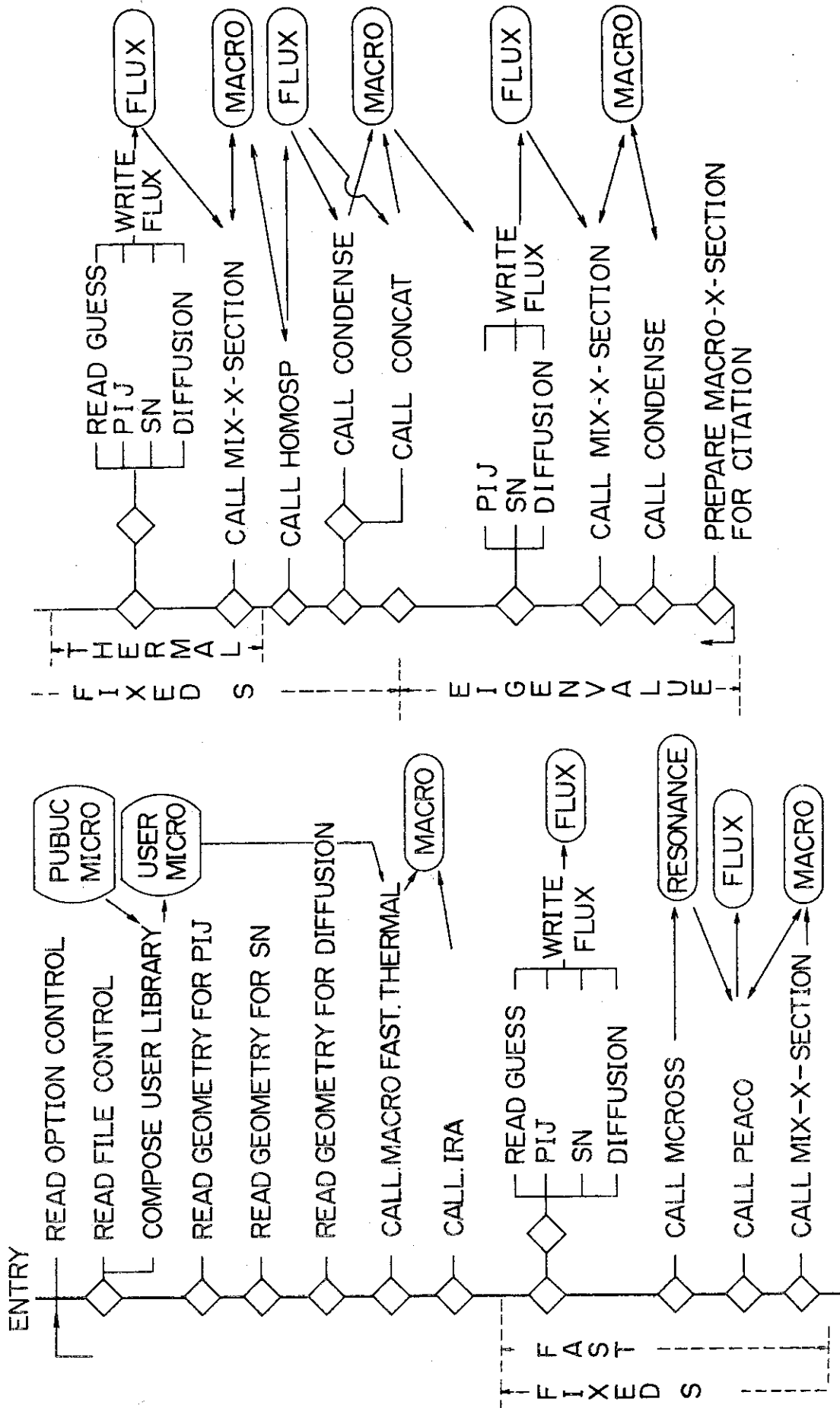


Fig. 2.1.1.1 SRAC flow diagram



## 2.2 Finite Element Method to Solve the Three-Dimensional Neutron Transport Equation

Y. Nakahara

A double finite element method algorithm has been formulated to solve the three dimensional multigroup neutron transport equation. Both angular and spatial variable domains are approximated by the finite element subdomains, from which comes the terminology of the double finite element method (DFEM).

The  $S_N$  method has been the most popular and practical method to solve the transport equation and is still the most effective one available at present for one and two dimensional reactor configurations. It is well known, however, that the  $S_N$  method has a intrinsic shortcoming, i.e., the ray effect in the medium where anisotropic neutron transport is dominant. This results from the discretization of the angular space. The ray effect would be reduced by taking a large number of  $N$ , but in the three-dimensional calculations this skyrockets the total number of entire meshes (energy  $\times$  space  $\times$  angle) and is actually impracticalble. In order to mitigate this difficulty the finite element method has been applied to the angular domain, subdomains of which are spanned by the continuous basis functions.

The spatial domains are treated in the same way as in the FEM-BABEL, finite element program for three-dimensional neutron diffusion equation<sup>1)</sup>.

A Vladimorov-Ritz-Galerkin type approximation<sup>2)</sup> has been employed in formulating the solution algorithm. At first we define an angular flux  $u(\vec{r}, \vec{\Omega})$  symmetrized in the angle  $\vec{\Omega}$ :

$$u(\vec{r}, \vec{\Omega}) = \frac{1}{2} [\psi(\vec{r}, \vec{\Omega}) + \psi(\vec{r}, -\vec{\Omega})] \quad (1)$$

where  $\psi$  is the angular flux in the common meaning. The approximate solution  $\bar{u}(\vec{r}, \vec{\Omega})$  can be expressed as

$$\bar{u}(\vec{r}, \vec{\Omega}) = \sum_{i=1}^I \sum_{j=1}^J c_{ij} \phi_i(\vec{r}) \chi_j(\vec{\Omega}) \quad (2)$$

where  $\phi_i$  and  $\chi_j$  are bases for the spatial and angular domains, respectively.

A choice of the angular bases remains to be investigated. In the

present formulation the bicubic spline polynomial bases are tried, following the arguments given by Kaper et al.<sup>2)</sup> The angular bases are decomposed further to

$$\chi_j(\vec{\Omega}) = \lambda_k(\phi)\tau_\ell(\xi), \quad (3)$$

where  $0 \leq \phi \leq \pi$  and  $0 \leq \xi \leq 1$ ,  $\lambda_k$  and  $\tau_\ell$  being the cubic spline functions.

The detailed description of the algorithm is too lengthy to be reproduced here. The programming work is scheduled to start in the next fiscal year.

#### References

- 1) Ise T., Yamazaki T., Nakahara Y.: "FEM-BABEL: A Computer Program for Solving Three-Dimensional Neutron Diffusion Equation by the Finite Element Methods", JAERI 1256 (1978).
- 2) Kaper H.G., Leaf G.K., Lindenman A.J.: "Application of Finite Element Methods in Reactor Mathematics, Numerical Solution of Neutron Transport Equation", ANL-8126 (1974).

### 2.3 Acceleration of Convergence of Iterations in Neutron Diffusion Codes

T. Fujimura and Y. Matsui\*

It is well known that the multi-group neutron diffusion equation is solved by the iterative method which is composed of outer (source) and inner (flux) iterations. The applications of an adaptive acceleration method to the inner iterations are studied<sup>1)</sup> numerically, investigating how it accelerates the convergence of outer iteration.

Let us consider now the  $g$ -th energy-group equation

$$L_g \phi_g = S_g,$$

where  $L_g$ ,  $\phi_g$  and  $S_g$  are the loss, flux and source of neutron, respectively. Then, the inner iteration by the first order stationary linear iteration is given as follows

$$\phi_g^{k+1} = B_g(\omega) \phi_g^k + C_g(\omega) S_g \quad (k = 0, 1, 2, \dots), \quad (1)$$

where  $B_g(\omega) = I - C_g(\omega) L_g$  is the iteration matrix with a fixed acceleration parameter  $\omega$ . The acceleration algorithm for Eq. (1), originally by Tanabe<sup>2)</sup>, is defined as follows:

$$e_k = \phi_g^{k+1} - \phi_g^k,$$

$$f_k = B_g(\omega) e_k,$$

$$\alpha_k = (e_k, e_k - f_k) / \|e_k - f_k\|^2,$$

$$\phi_g^{k+2} = \phi_g^{k+1} + \alpha_k f_k.$$

It is known that the method works effectively when the iteration matrix is non-negative definite and the parameter  $\omega$  is not chosen optimally.

In order to show the effect of the method for acceleration, we take up two three-dimensional diffusion codes that were developed in JAERI.

---

\* Japan Information Service Co. Ltd., Tokyo

The above method is applied to the SSOR iteration of FEM-BABEL<sup>3)</sup>, and to the ADI iteration of DIFFUSION-ACE<sup>4)</sup>.

First, we adopt an example which comes from a slight modification<sup>3)</sup> of a PWR of 1420 MW given in the IAEA benchmark book. The calculation by the FEM-BABEL was performed with average mesh width of 5 cm and the SSOR parameter  $\omega = 1.1$ , that seem adequate in our experience. As shown in Fig. 2.3.1, remarkable improvement of convergence is seen in the eigenvalue  $k_{\text{eff}}$ .

Next, we propose that the acceleration method can be applied to the case where the iteration matrix  $B_g(\omega)$  is not non-negative definite, using DIFFUSION-ACE code. The outer iteration is controlled by the maximum block-source deviation:

$$\text{MBSD} = \max_{\ell} |(\theta_{\ell}^{m+1} - \theta_{\ell}^m) / \theta_{\ell}^{m+1}| \quad (2)$$

where  $\theta_{\ell}^m$  is the source at the  $m$ -th outer iteration on the  $\ell$ -th block (coarse mesh). We chose here a thermal reactor which has the size of  $78.8 \times 78.8 \times 200.6 \text{ cm}^3$ . The parameter  $\omega$  of ADI is taken again 1.1. The source deviation versus execution time, in this case, is shown in Fig. 2.3.2. As seen from this figure, the present method reduces the source deviation to the same degree by consuming only two-third of the time for ADI.

#### References

- 1) Fujimura T., Matsui Y.: submitted to Nucl. Sci. Eng.
- 2) Tanabe K.: "An Adaptive Acceleration of General Linear Iterative Process for Solving Systems of Linear Equations", RM-43 (The Institute of Statistical Mathematics, Tokyo) (1971).
- 3) Ise T., Yamazaki T., Nakahara Y.: "FEM-BABEL A Computer Program for Solving Three-Dimensional Neutron Diffusion Equation by the Finite Element Method", JAERI-1256 (1978).
- 4) Naito Y., Maekawa M., Shibuya K.: "A Three-Dimensional Neutron Diffusion Calculation Code: DIFFUSION-ACE", JAERI 1262 (1979).

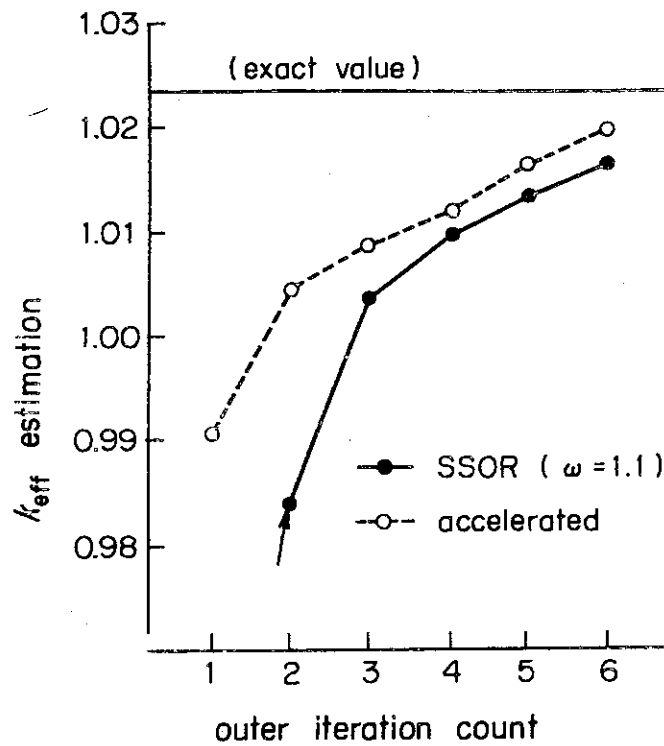


Fig. 2.3.1 Acceleration of convergence of  $k_{\text{eff}}$  for a 1420 MW PWR problem

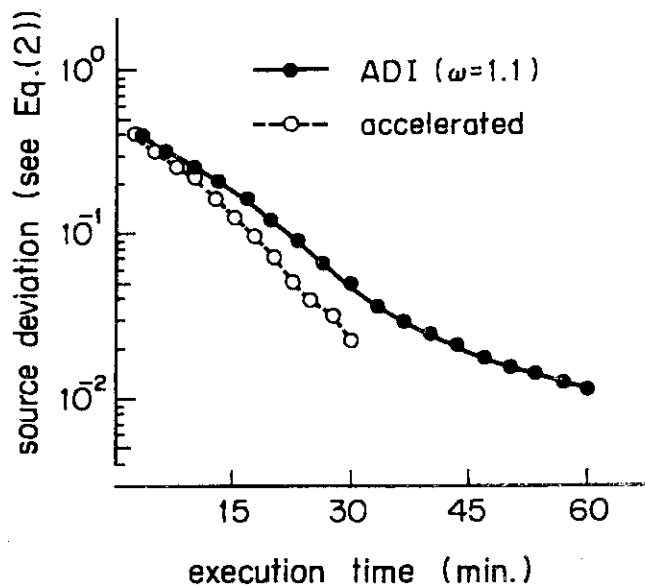


Fig. 2.3.2 Effect of acceleration for the calculation of a thermal reactor shown versus execution time

## 2.4 Detailed Analysis of Reactor Cell and Core Calculations of VHTR

K. Tsuchihashi and Y. Gotoh

A new collision probability routine CLUPH was added to the LAMP-B<sup>1)</sup> to analyze the hexagonal VHTR fuel and control rod blocks, where in addition to the annular array of fuel pin rods the asymmetric insertions of burnable poison rods and control rods are characteristic

The perfect reflective boundary condition is no more realistic to consider the arrangement of the asymmetric hexagonal blocks. The periodic and rotational arrangements of blocks were surveyed to study the interference effect between the burnable poison rods. Both gave the identical results due to the relatively transparent cross section of intervening graphite. The cylindrical approximation with isotropic boundary condition was also tried, which gave the practically identical results as the exact hexagonal pattern.

The effects of a grain of coated fuel particles in fuel rod, and of a B<sub>4</sub>C grain in burnable poison rod, are investigated. The neglect of the grain structure of burnable poison results in the underestimate of  $\eta f$  value of the standard full block from 1.49 to 1.42. The average cross sections of control rod block were derived from the calculation of a super cell which is composed of one control rod block and of the surrounding six fuel blocks. A care was taken to deal with the control rod block located at core-reflector boundary by replacing a part of the surrounding material by reflector graphite.

Using the two energy group constants obtained by the process described above, the core calculations were executed by the code CITATION, to investigate the reactivities of the control rods. The specifications of the calculation are as follows: The geometry is two dimensional triangle, zone number per block 6, mesh number per block 24, boundary condition 60° rotational, and the black absorber is placed beyond the reflector. All possible combinations are surveyed by changing the number of control rods inserted in the center, the first and the outer (second and third) ring control rod blocks, and by keeping the 60° rotational symmetry around the core axis. The typical neutron flux distribution in the 1/6 sector is shown in Fig. 2.4.1. The change of  $k_{eff}$  associated with the draw of a rod from the central control rod block are plotted

versus the  $k_{\text{eff}}$  of the initial state in Fig. 2.4.2, where the three numbers in parentheses are the number of control rods in the central, the first and the outer ring control rod blocks, respectively.

#### Reference

- 1) Tsuchihashi K.: "LAMP-B: A Fortran Program Set for the lattice Cell Analysis by Collision Probability Method", JAERI 1259 (1979).

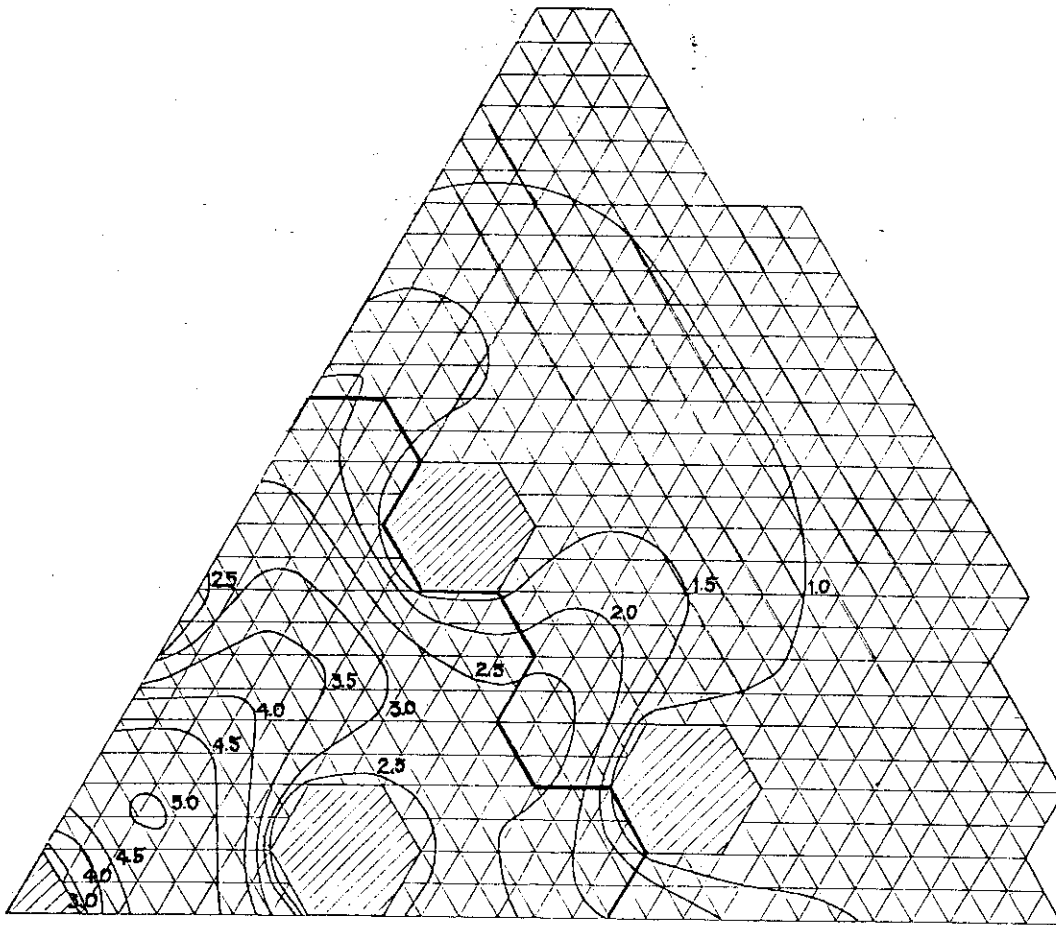


Fig. 2.4.1 Neutron flux distribution in VHTR (1/6 sector)

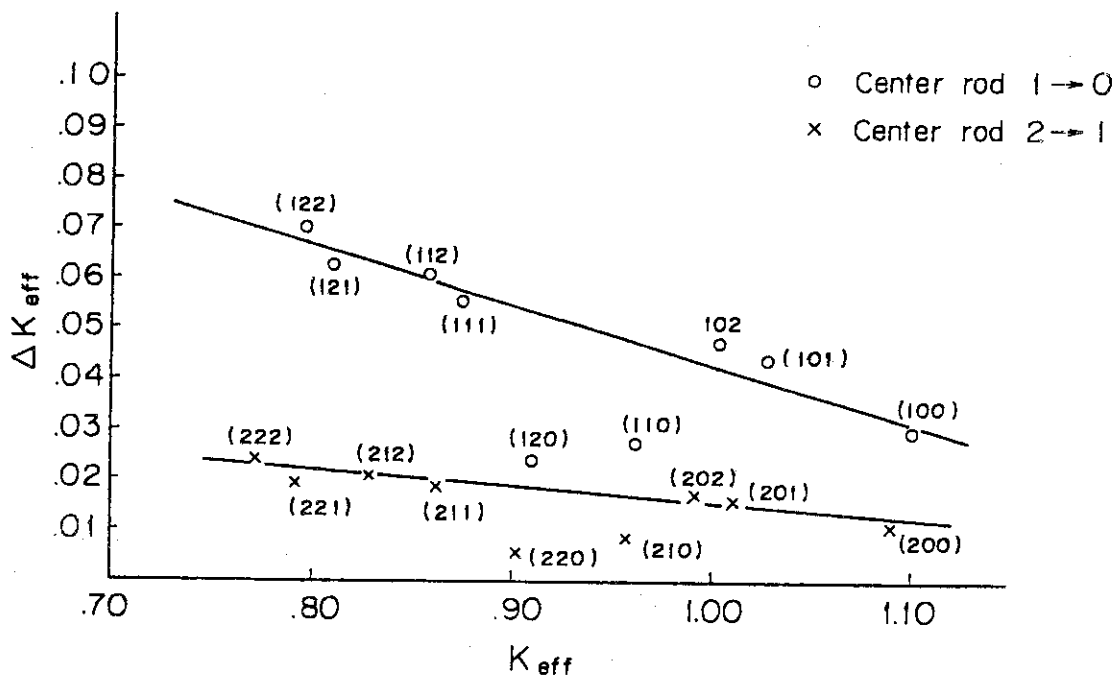


Fig. 2.4.2 Control rod worth of the central control rod block



## 2.5 Probabilistic Method for Evaluation of Reactivity Margin of VHTR

Y. Kaneko

A probabilistic method is proposed to evaluate the possibility in core design stage that the safety criteria in reactivity margin are satisfied, taking account of the uncertainties in design calculation<sup>1)</sup>. For application of the present method to the design-study-cores of Experimental Very High Temperature Reactor, investigations are made for the relation between the design accuracy and the probability that the safety criteria in both shut-down and operation margins are satisfied. The results are shown in Fig. 2.5.1. In conclusion, for the MARK-III core, with the correlation disregarded, the ratio of the standard deviations to the design values must be less than 0.79 and 5.3 %, respectively, for the cold clean effective multiplication factor and the reactivity worths of control rods, burnable poisons and core temperature rise, in order that the probability is larger than 99.7 % (three times the sigma limit). With the correlation regarded, the ratios must be considerably smaller.

## Reference

- 1) Kaneko Y.: "Probabilistic method for evaluation of reactivity margin of VHTR", JAERI-M 8847 (1980)

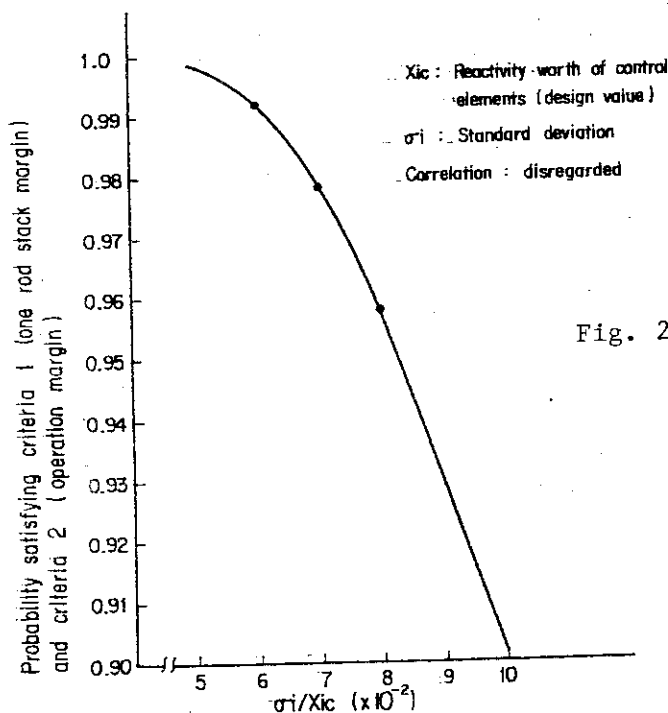


Fig. 2.5.1 Dependence of probability satisfying criteria 1 (one rod stack margin) and 2 (operation margin) on the ratio of standard deviation to design reactivity worth of control elements

## 2.6 Determination of Order of Priority among Nuclear Data of Actinides by Means of Nonlinear Optimization Technique

H. Mitani

The present status of actinide cross sections is not satisfactory especially in fast energy region. It is, therefore, necessary to measure and evaluate these cross sections with high accuracy. For the purpose, it is useful to make clear the required accuracy of nuclear data of actinides and the order of priority among these data quantitatively.

In general, the required accuracy and the order of priority can be determined by solving nonlinear optimization problem. This is expressed in a form of minimizing a nonlinear objective function under linear constraints, that is,

$$\text{minimize} \quad Q = \sum_{j=1}^N \frac{\omega_j}{\Delta_{a,j}^2} \left( \frac{1}{y_j} - 1 \right), \quad (1)$$

$$\text{subject to} \quad g_i = \sum_{j=1}^N A_{i,j} y_j - D_i \leq 0, \quad (2)$$

$$(i = 1, \dots, M)$$

$$0 < y_j \leq 1, \quad (3)$$

where

$$y_j = \frac{x_{r,j}^2}{\Delta_{a,j}^2}, \quad A_{i,j} = \frac{S_{i,j}^2 \Delta_{a,j}^2}{\sum_{k=1}^N S_{i,k}^2 \Delta_{a,k}^2}, \quad D_i = \frac{d_i^2}{\sum_{k=1}^N S_{i,k}^2 \Delta_{a,k}^2}. \quad (4)$$

In Eqs. (1) ~ (4),

- $x_{r,j}$  : required accuracy of nuclear data  $j$ ,
- $\Delta_{a,j}$  : achieved accuracy of nuclear data  $j$ ,
- $S_{i,j}$  : sensitivity coefficient of physics parameter  $i$  due to nuclear data  $j$ ,
- $d_i$  : target accuracy of physics parameter  $i$ ,
- $\omega_j$  : a proportional constant.

From Eqs. (1) ~ (3), it is apparent that, if the number of cross sections  $N$  is equal to that of physics parameters  $M$ , then, the required

accuracy and order of priority can be determined by solving only Eq. (2). On the other hand, if  $N$  is larger than  $M$ , Eq. (2) has no unique solution. In the case, it becomes necessary to solve the nonlinear optimization problem given by Eqs. (1) ~ (3).

In the present study, it is assumed that a cost function is proportional to the quantity of information obtained from the experiment. According to Fisher's definition, the quantity of information is given by  $I_{\Delta_j} = 1/\Delta_j^2$  where  $\Delta_j$  is the standard deviation or the accuracy in the measurement of nuclear data  $j$ . Then, the improvement of accuracy of cross section  $j$  from  $\Delta_{a,j}$  to  $x_{r,j}$  requires the cost of  $Q_j = \omega_j(1/x_{r,j}^2 - 1/\Delta_{a,j}^2)$ , so that the total cost is given by Eq. (1).

The similar cost functions were also used by Usachev et al.<sup>1)</sup> and Miki et al.<sup>2)</sup>. They obtained the desirable accuracy of nuclear data for minimizing the design margin in fast reactor nuclear designs and also Usachev et al.<sup>3)</sup> obtained required accuracy of transactinide nuclear data for burn-up calculation in fast reactors.

The required accuracy of nuclear data of actinides and order of priority among these data for estimating actinide production in a 1000 MWe fast reactor with Pu fuel discharged from BWR were calculated by using the code CORASE<sup>4)</sup>. This code solves the nonlinear optimization problem by using "controlled random search method". The order of priority among nuclear data of actinides is given in Table 2.6.1, which is obtained by assuming a plausible target accuracy for production of 10 actinides other than major uranium and plutonium isotopes.

The order of priority seems to be strongly dependent on the assumed target accuracy, so that a careful examination is needed to determine the target accuracy. A numerical examination is also necessary for finding out the best method of solving the nonlinear optimization problem given by Eqs. (1) ~ (3).

#### References

- 1) Usachev L.N., Bobkov Yu.G.: "Planning an Optimum Set of Microscopic Experiments and Evaluations to Obtain a Given Accuracy in Reactor Parameter Calculations", INDC(CCP)-19/U, (1972).
- 2) Miki K., Inoue K.: "Evaluation of Desirable Accuracy for Nuclear Data in Fast Reactors by Optimization Method", J. Nucl. Sci. Technol., 14[1], 58 (1977).

- 3) Usachiev L.N., et al.: private communication (1978).
- 4) Suzuki Ta.: "Comparative Evaluation of Various Optimization Methods and Development of An Optimization Code System SCOOP", JAERI-1263 (1979) [in Japanese].

Table 2.6.1 Order of priority among nuclear data of actinides

Order	Nuclide	Reaction	$x_r/\Delta_a$
1	Pu-242	$\sigma_c$	0.157
2	Am-243	$\sigma_c$	0.165
3	U-238	$\sigma_{n,2n}$	0.168
4	Am-241	$\sigma_c$	0.256
5	Am-243	$\sigma_f$	0.295
6	Pu-242	$\sigma_f$	0.296
7	Cm-242	$\sigma_f$	0.302
8	Pu-239	$\sigma_{n,2n}$	0.324
9	Cm-242	$\sigma_c$	0.352
10	Cm-244	$\sigma_c$	0.354
11	U-236	$\sigma_c$	0.382
12	Pu-240	$\sigma_c$	0.430
13	Pu-238	$\sigma_c$	0.448
14	Am-241	$\sigma_f$	0.495
15	Am-242m	$\sigma_f$	0.499
16	Pu-241	$\sigma_f$	0.516
17	Am-242m	$\sigma_c$	0.534
18	Cm-245	$\sigma_f$	0.536
19	Pu-238	$\sigma_f$	0.557
20	Pu-241	$\sigma_c$	0.563

## 2.7 Study of the Stochastic Point Reactor Kinetic Equation

Y. Gotoh

Recently, the effect of fluctuating reactivity noise in point kinetic equation, was investigated by Quabili and Karasulu<sup>1)</sup> by using Bouret's approximation and logarithmic linearization. Once the author<sup>2)</sup> had attempted to solve the stochastic point reactor kinetic equation using a diagrammatic method. The method has been applied to a white noise for which the exact result was obtained by Akcasu and Karasulu<sup>3)</sup>, and to a non-white noise also. A Green's function dressed with the clouds of noise is defined, which is a transfer function of point reactor with fluctuating reactivity. It is shown easily that the condition that the mean power does not diverge is the same one obtained by Akcasu and Karasulu for a white noise.

The integral equation for correlation function can be derived by using the following assumptions: 1) Green's function should be dressed with noise, 2) The ladder type diagrams only contributes to the correlation function of power. The condition of non-divergence of  $\langle N^2(t) \rangle$  can be obtained from this integral equation in case of white noise. The integral equation for power spectral density is modified so that the transfer function is one of point systems with fluctuating reactivity. For a white noise and the one delayed neutron approximation, the norm of the integral equation is exactly evaluated. The variance to mean-squared ratio can be obtained by integrating the power spectral density, and is exactly integrated for a white noise. To evaluate precisely the variance to mean squared ratio for a non-white noise, the integral equation for power spectral density should be solved, but the approximate solution was integrated. The following noise correlation function was used to evaluate the variance to mean squared ratio.

$$\phi(t) = \frac{G_k \Lambda}{2\tau} e^{-t/\tau}$$

In Fig. 2.7.1 the variance to mean squared ratio to the various noise amplitudes are shown, by changing the correlation time of noise, where  $\ell = 10^{-4}$  sec,  $\lambda = 0.318 \text{ sec}^{-1}$  and  $\Delta k = -1.0\%$ .

It is shown that the diagrammatic method applied to the stochastic point reactor kinetic equation is successful to yield the exact result

known for a white noise. For a non-white noise, the variance to mean squared ratio decreases as the correlation time of noise increases, and for the short correlation time of noise the numerically evaluated value approaches to the exact one of white noise.

#### References

- 1) Quabili F.R. and Karasulu M.: Ann. Nucl. Energy 6 133 (1979).
- 2) Gotoh Y.: Ann. Nucl. Energy 2 119 (1975).
- 3) Akcasu A.Z. and Karasulu M.: Ann. Nucl. Energy 3 11 (1976).

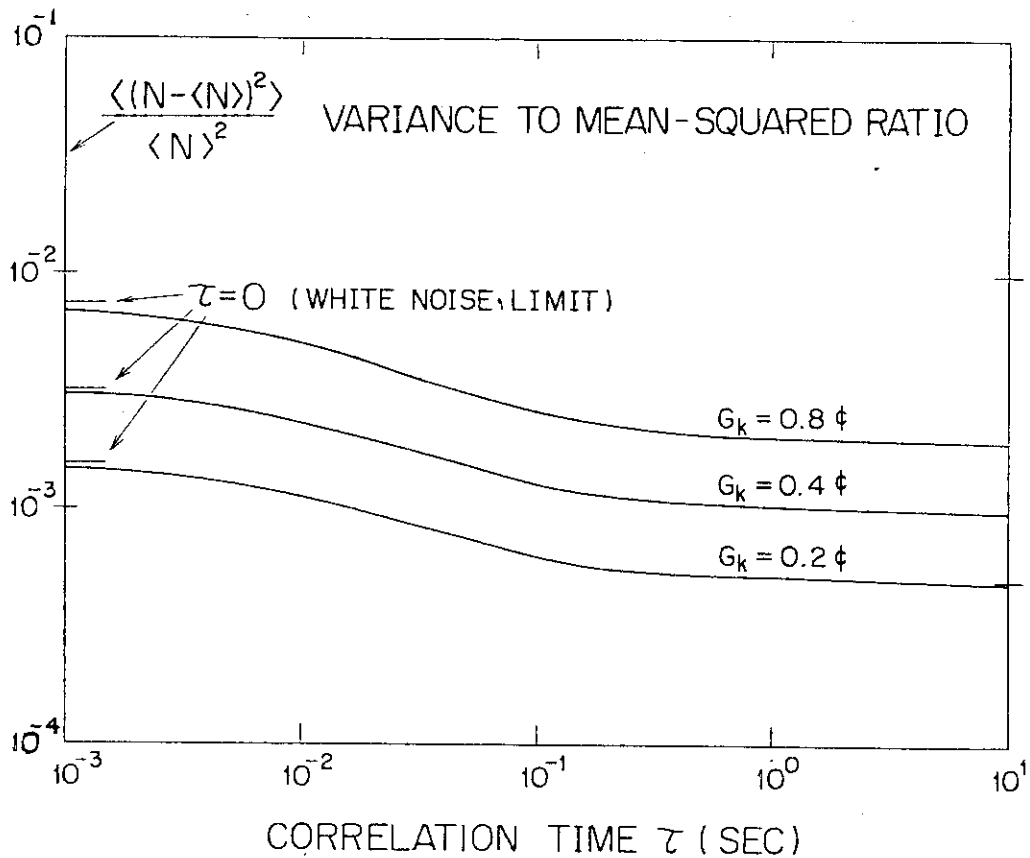


Fig. 2.7.1 Variance to mean-squared ratio as a function of the correlation time of noise.

## 2.8 Kinetics of Anisotropic Particle-Transport in Dense Gases

Y. Taji

It is well known that the transport equation of neutron in a medium is based on the Boltzmann equation. This equation has been used successfully for transport of not only the classical particles but also the quasi-particles in solid state physics. In spite of the usefulness of this equation, however, it cannot be said that this equation has been explored completely from the first principle of classical mechanics. It depends on some assumptions. Also in the experimental observations it seems to appear some discrepancies between the experimental and theoretical results.

A correction for the theory of neutron transport has been already proposed by the author<sup>1)</sup> though rather intuitively. Then, for the justification of the proposal, the following three problems are to be investigated: (a) to find a general method to derive the Boltzmann equation for the rarefied gases from the first principle of classical mechanics, (b) to show that on the basis of the method it is possible to derive a kinetic equation for dense gases where the triple collisions are not negligible and (c) to derive, in the similar manner as in (b), a kinetic equation for the binary mixtures, i.e., the system of rarefied gases in a dense medium. The last (c) will become the answer for the problem of neutron transport in a medium. Our study has almost accomplished the items (a) and (b) at present<sup>2,3)</sup>.

Problem (a). We start with the well-known B.B.G.K.Y. equation and a time reversed B.B.G.K.Y. equation which is derived from the time reversed Liouville equation. The only one assumption introduced in this case is to cut off the terms of triple collisions because it is rarefied gas. The macroscopic distribution function is defined as the time average of the microscopic one according to Kirkwood's method as

$$\bar{f}(r, p; t / f(;t)) = \frac{1}{\tau} \int_0^{\tau} ds f(r, p; t+s), \quad (1a)$$

$$\bar{f}(r, -p; t / f(;t+\tau)) = \frac{1}{\tau} \int_0^{\tau} ds f(r, -p; t+\tau-s), \quad (1b)$$

in the forward and the reverse form, respectively, and  $f(;t)$  and  $f(;t+\tau)$

in  $\bar{f}$  represent the initial condition of the time integral. The integral value must be independent of the integral direction. Therefore, the condition for the two averages of (1a) and (1b) to coincide with each other corresponds to the very condition for the deterministic expression of the distribution function. The result is obtained as follows, (1) the spatial distribution to be uniform in the spatial interval corresponding to  $\tau$  and (2) the momentum distribution to be independent of the sign of momentum, i.e., isotropic also in  $\tau$ . However,  $\tau$  remains arbitrary.

Problem (b). In rarefied gases the binary encounter is subjected to the four relations of the conservation law of momentum and energy. Then the two degrees of freedom among the six of  $p_1, p_2$  are undetermined or degenerated. The effect of triple collisions in dense gases is introduced for this two degrees of freedom to be determined. It has been cleared that the effect results in a force against the dissipation of the momentum  $p_1+p_2$ , i.e., the viscosity. The force is introduced newly into the Boltzmann equation in the form of the average force field to obtain a new kinetic equation. The  $\tau$  is cleared to be the mean free time.

#### References

- 1) Tajiri Y.: J. Phys. Soc. Jpn., 41, 2020 (1976).
- 2) Tajiri Y.: Proc. Spring Meeting of Phys. Soc. Jpn., 29aR5 (1980).
- 3) Tajiri Y.: Proc. Spring Meeting of Phys. Soc. Jpn., 1aF3 (1980).



## 2.9 High Resolution Structure Images of a Simple Defect in a Silicon Crystal Oriented in (110)

T. Nishida, K. Izui, S. Furuno and H. Otsu

We had searched the structure images in a perfect crystal of silicon oriented in (110) and sought the optimum conditions to obtain the best images on a high resolution electron microscopy<sup>1),2)</sup>. Based on those results, we advanced to the studies of simulating the structure images of a simple defect such as a vacancy or an interstitial cluster included in a crystal, and of searching the physical and optical conditions to observe it at the experiments of a radiation damage. There are a number of problems to be solved for the proper interpretation of the images of lattice defects in terms of atom configurations, as pointed out by some researchers<sup>3),4)</sup>. As the first step, we began the study on making the modification of the current multi slice method of electron diffraction for its application to the simulation of defect lattice images.

### a) Slight modification of multi-slice method and a model of a simple defect lattice

We took the superlattice based on the assumption of periodic continuation at its boundaries in the lateral dimensions. Figure 2.9.1(a) shows the configuration of a superlattice which is  $3 \times 3$  times the original unit cell of silicon oriented in (110). Here the cross symbol denotes a vacancy and the black circle the atom location without relaxation. A model of divacancy clusters is assumed to be a stacking of slices representing a perfect lattice and ones containing a divacancy with the thickness of  $\Delta Z$  as illustrated in Fig. 2.9.1(b). Thus, this cluster may be expressed as the following symbol  $3P4V_23P$ . Figure 2.9.1(c) is the diffraction pattern of a silicon oriented in (110). For the case of a  $(3 \times 3)$  superlattice, diffuse waves  $3 \times 3$  times Bragg reflections should be sampled to calculate the defect image in addition to them. Concentric circles seen in this figure indicate objective apertures used in the present calculations.

By use of the multi-slice theory, as well known, the propagation of an electron through the crystal is calculated from a convolution form of an amplitude  $U_{n-1}$  of the wave function multiplied by the propagation

factor  $P$ , and the structure amplitude  $G_n$  of each slice as follows:

$$U_n(h,k) = [U_{n-1}(h,k) \cdot P(h,k)] * G_n(h,k), \quad (1)$$

$$P(h,k) = \exp[-i\pi\lambda\Delta z\{(\frac{h}{A})^2 + (\frac{k}{B})^2\}], \quad (2)$$

$$(n = 2, 3, \dots, N)$$

and the image intensity  $I_n$  is given by

$$I_N(h,k) = |F^{-1}[U_N(h,k) \cdot e^{-i\chi_{h,k}} \cdot H(h,k)]|^2, \quad (3)$$

$$\chi_{h,k} = \pi\lambda\Delta f\{(\frac{h}{A})^2 + (\frac{k}{B})^2\} - \frac{\pi}{2} C_s\lambda^3\{(\frac{h}{A})^2 + (\frac{k}{B})^2\}^2. \quad (4)$$

In the above equations, symbols  $*$  and  $F^{-1}$  denote convolution operation and inverse Fourier Transformation respectively, and  $H(h,k)$  the pupil function representing the objective aperture.  $C_s$  and  $\Delta f$  are the spherical aberration coefficient and the quantity out of focus for an objective lens. The values of  $G_n$  are calculated from Lynch's approximation, depending on the change of the defect structure in the depth direction. The cell constants  $A$  and  $B$  used in the superlattice calculations are given to be  $3a$  and  $3b$  respectively, where  $a$  and  $b$  represent the dimensions of the original cell.

- b) Size dependence of a divacancy cluster images formed with an ideal lens ( $\Delta f = 0$ ,  $C_s = 0$ )

In the present paper, the images of a divacancy cluster without relaxation are mainly searched. The contrast of the image formed with an ideal lens at 100 kV seems to increase with increasing the size of a divacancy cluster as simulated in Fig. 2.9.2. The curves just below them show the image intensity profiles along the traverse line on the divacancy and the values of percentage give the reduction ratios of the peak intensity due to the divacancy clusters with 16, 10, 4 and 2 defect slices respectively. As seen from these figures, the image of a cluster with a larger size than ten disappears completely, although the  $2V_2$  image is barely detectable.

c) Real images of divacancy clusters ( $\Delta f \neq 0$ ,  $C_s \neq 0$ )

For real images of a defect, there are mainly two requirements to be considered in defocusing. Both are to form the real image of the defect at its exact location and to obtain the high resolution images of crystal structure to which a defect is imbedded. It is not easy to search the defocus condition which fulfills simultaneously both requirements. Figure 2.9.3 shows the through focus images of a divacancy cluster  $[3P4V_23P]$  with  $C_s = 0.7$  mm and the objective aperture  $G_3$  indicated in Fig. 2.9.1(c). Among those images, the best one is obtained for the defocus  $500 \text{ \AA}$ , so-called Scherzer focus, at which we can see the shape of a divacancy at its exact location in a (110) lattice due to the reduction of contrast. A divacancy could not be distinguished on the images formed for the optimum defocus  $-68 \text{ \AA}$  reported already<sup>2)</sup> and the other defoci. In Fig. 2.9.4, the structure images of  $[P4V_25P]$  for Scherzer focus are simulated with several sizes of the aperture  $G_0 \sim G_3$  and the cosine curve of  $\chi$  in Eq. (4) given for the same focus. Figure 2.9.4(b) tells us that there is a defect in the exact location although it cannot be recognized to be a divacancy cluster because of the unresolved image of the nearest pair atoms. From Figs. 2.9.4(c) and (d), no information about the crystal structure could be gotten but we can know only the existence of some defect and roughly its position. Further researches should be carried out to obtain the optimum conditions for imaging the defect crystal in an electron microscopy.

## References

- 1) Izui K., Furuno S., Nishida T., et al.: "High Resolution Electron Microscopy of Images of Atoms in Silicon Crystal Oriented in (110)", J. Electron Microscopy, 27, No.3, 171 (1978).
- 2) Nishida T.: "Electron Optical Conditions for the Formation of Structure Images of Silicon Oriented in (110)", Japan J. Appl. Phys., 17, No.5, 799 (1980).
- 3) Fields P.M., Cowley J.M.: "Computed Electron Microscope Images of Atomic Defect in F.C.C. Metals", Acta Cryst., A34, 103 (1978).
- 4) Spence J.C.H.: "Approximation for Dynamical Calculation of Micro-diffraction Pattern and Images of Defects", Acta Cryst., A34, 112 (1978).

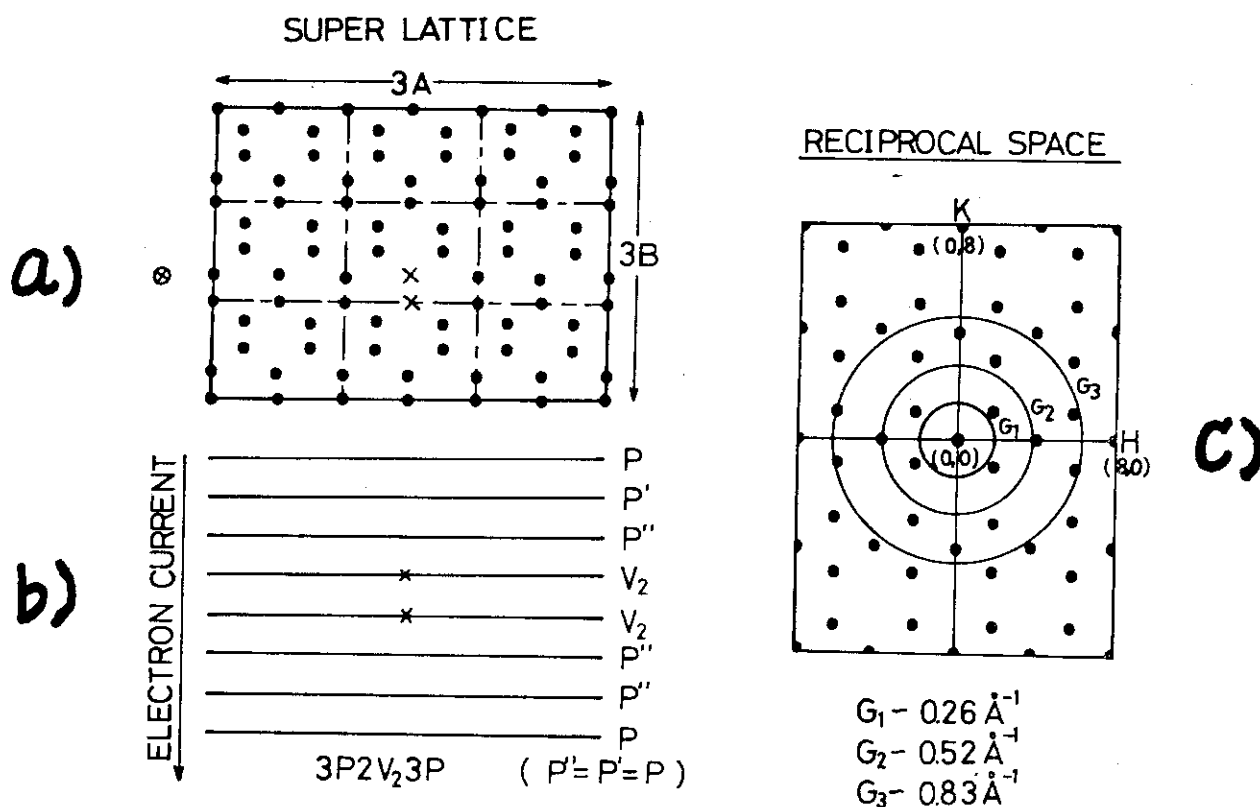


Fig. 2.9.1 A superlattice model used in the multi slice calculation for a simple defect image in a silicon crystal oriented in (110).

- (3x3) superlattice on (110) including a divacancy. Black circles and crosses denote the atom and the divacancy positions in a lattice.
- stacking model of a divacancy cluster composed from the perfect (P) and defect (V<sub>2</sub>) slices in the direction of electron current.
- diffraction pattern in the reciprocal space calculated for a perfect lattice of silicon oriented in (110). G<sub>1</sub> to G<sub>3</sub> indicate the sizes of the aperture used in the present calculation.

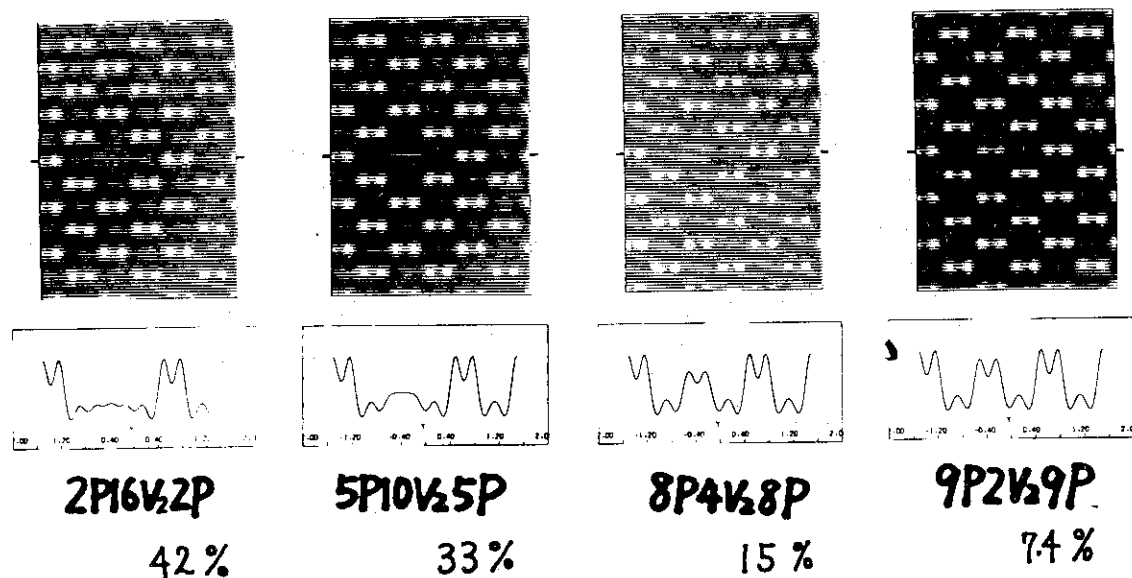


Fig. 2.9.2 Size dependence of the ideal images ( $\Delta f=0$ ,  $C_s=0$ ) of divacancy clusters with 16, 10, 4 and 2 defect slices in a 20 slices of (110) silicon. The values of percentage are the reduction ratios of the peak intensity on  $V_2$ -cluster at 100 kV.

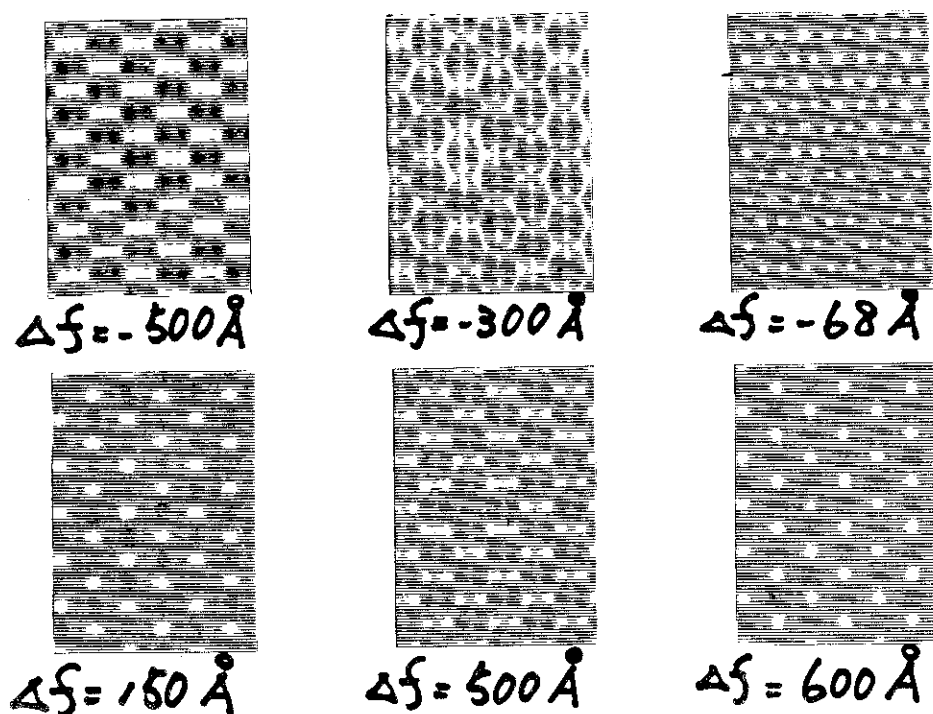


Fig. 2.9.3 A through focus series of simulated images of a divacancy cluster [3P4V<sub>2</sub>3P], where  $\Delta f = 500 \text{ \AA}$  is Scherzer focus. ( $C_s=0.7 \text{ mm}$ ,  $G_3$ , 100 kV)

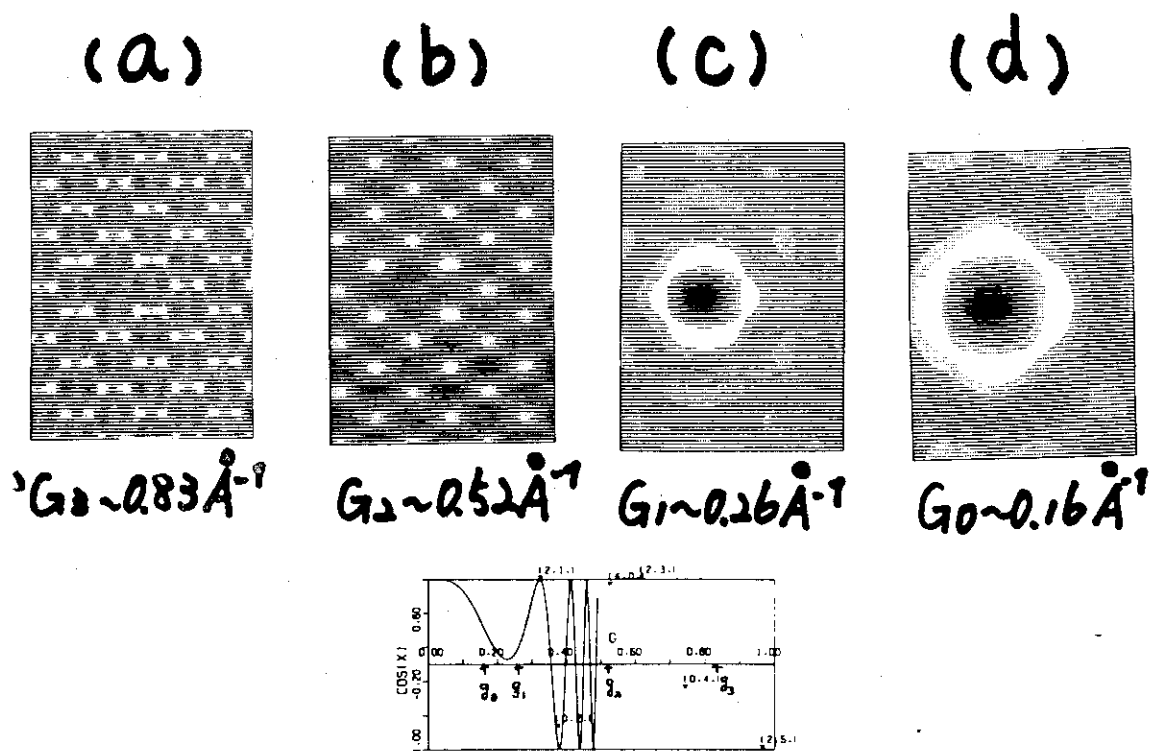


Fig. 2.9.4 Variation of [P4V<sub>2</sub>5P] image with sizes of the objective aperture ( $G_3$  to  $G_0$ ) ( $\Delta f = 500 \text{ \AA}$ ,  $C_s = 0.7 \text{ mm}$ , 100 kV). The curve and dots in the under figure represent the distribution of  $\text{Cos } \chi$  against  $|g|$  less than 0.5 and the values of the function to (2,1), (4,0), (2,3) and (0,4) reflections respectively.  $g_0, g_1, g_2$  and  $g_3$  denote the sizes of the aperture.

### 3. Integral Experiment and Analysis

#### 3.1 Measurement of Reactivity Worths of Burnable Poison Rods in SHE-14 Core

F. Akino, M. Takeuchi, K. Kitadate, H. Yoshifuji and Y. Kaneko

As core design for the Experimental Very High Temperature Gas Cooled Reactor progresses, evaluation of design precision has become increasingly important. For a high precision design, adequate group constants based on accurate nuclear data, as well as calculation method properly describing the physical behavior of neutrons, are required. We, therefore, assembled a simulation core for VHTR, SHE-14, using a graphite-moderated 20 %-enriched uranium Semi-Homogeneous Experimental Critical Facility (SHE), and obtained experimental data useful in evaluating design precision. The VHTR is designed to accommodate burnable poison and control rods for reactivity compensation. Accordingly, the experimental burnable poison rods which are similar to those to be used in the experimental reactor were prepared, and their reactivity values were measured in the SHE-14 core. The experimental burnable poison rods were made by inserting 114 absorbing pellets in hollow graphite rod of 1180 mm in length. The absorbing pellets with 8 mm diameter, 10 mm height and 4.5 w/o boron content were formed by sintering  $B_4C$  particles of 425 ~ 710  $\mu m$  in diameter with graphite powder.

Specifications of  $B_4C$  particle size and boron content are as follows:

$B_4C$ particle diameter	:	~3 $\mu m$
		250 ~ 355 $\mu m$
		425 ~ 710 $\mu m$
		710 ~ 1000 $\mu m$
Boron content	:	2.25 w/o
		4.5 w/o
		9.0 w/o

One to three rods of the above experimental burnable poison rods were inserted into the central column of the SHE-14 core, and the reactivity values were measured by the period and fuel rod substitution method. The results of the measurements are shown in Fig. 3.1.1. It is clearly shown

that due to the self-shielding effect of  $B_4C$  particles the reactivity value decreases with increasing particle diameter. For the particle diameter, the reactivity value is found to increase linearly with the logarithm of boron content.

The measured values and those calculated are found to agree with each other within 5 %. These results indicate that the reactivity of the burnable poison rod can be estimated fairly accurately if the self-shielding effect of  $B_4C$  particles and the heterogeneity of the lattice cell are taken into account.

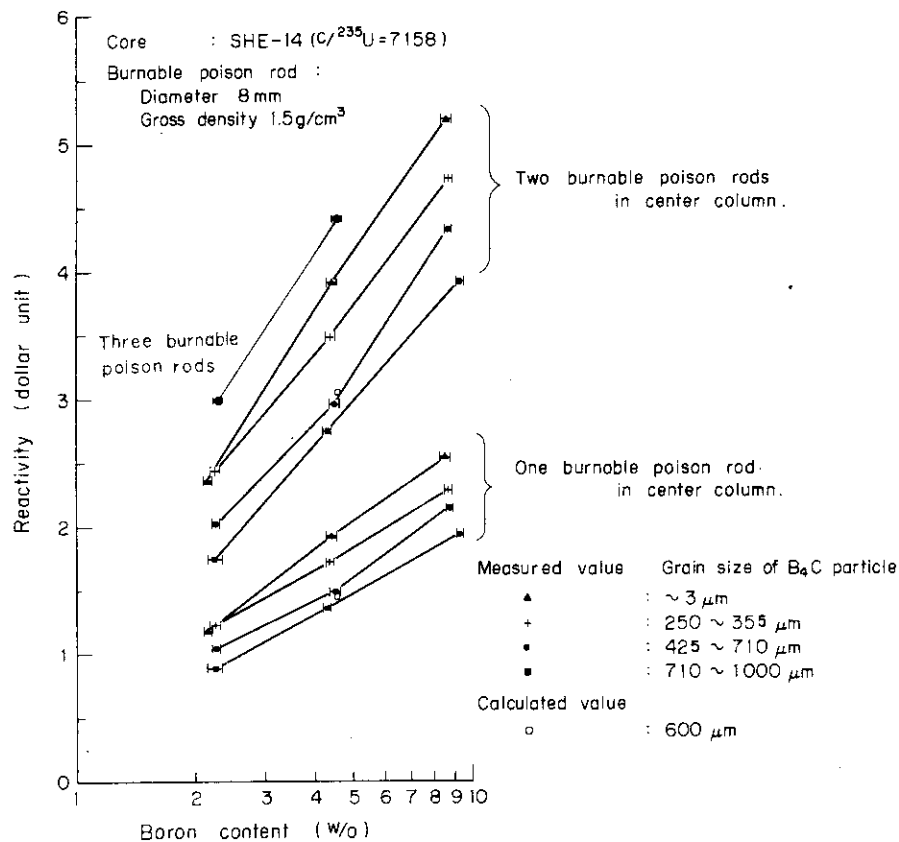


Fig. 3.1.1 Reactivity worths of burnable poison rods in central column of SHE-14 core.



### 3.2 Fuel Slumping Experiment on FCA Assembly VIII-2 (I): Reactivity Change

M. Nakano, H. Tsunoda\* and J. Hirota

A series of experiments have been made on FCA Assembly VIII-2 to examine the calculation method for the reactivity effect due to axial displacement of fuel/cladding. In the present study, emphasis was placed on the systematic measurement of reactivity changes in simple configurations rather than the simulation of a possible accident sequence.

R-Z configuration of Assembly VIII-2 is shown in Fig. 3.2.1. The assembly consisted of a central test region which simulates the prototype FBR "MONJU" in axial dimension and composition and a uranium fueled driver region. Axially asymmetric and symmetric displacements of fuel were made in the central 3x3 drawers (equivalent radius 9.3 cm) with sodium expelled. Four configurations studied are illustrated in Fig. 3.2.2. In the axially asymmetric displacement, fuel materials in a subregion above the midplane were slumped to the corresponding subregion under the midplane. Therefore, the reactivity change is mainly due to the lump effect of fuel material and the neutron streaming effect through the void region. The region of fuel displacement was successively widened from the midplane to the core edge in three steps. The compacted fuel is formed by removal of the stainless steel spacers resulting in the increase of fuel density by a factor of two, while the void region consists of the stainless steel spacers. In order to estimate the effect of the spacers, measurements were also made in the reduced stainless steel system where the density of the stainless steel spacer was reduced to 20 % of the normal one.

The reactivity effect is positive for all the asymmetric configurations studied. The reactivity change in the reduced stainless steel system is less positive than that in the normal stainless steel system, the difference between the two increasing rapidly with expansion of the fuel slumping region to the core edge. Therefore, it can be concluded that reactivity change due to fuel slumping is sensitive to the amount of structural material in the region where the fuel displacement takes place.

The initial analysis has been made using the JAERI-Fast Set Version II<sup>1)</sup> with 25 group structure. The R-Z diffusion calculation was carried

---

\* Tohoku Univ.

out with the CITATION code<sup>2)</sup>, using the cell averaged 25 group cross section prepared by the collision probability method. To take the neutron streaming effect into account, anisotropic diffusion coefficients were obtained with the Benoist's method<sup>3)</sup>. The calculation was made with both the conventional and the modified diffusion coefficients derived from the formula given in Ref. (4) for the void region (low density region). The calculated reactivity change for the respective fuel displacements is compared with the experiment in Table 3.2.1. The conventional calculation underestimates considerably the experimental values when the neutron streaming effect is large. Much improvement is achieved by using the modified diffusion coefficient for the void region. However, there still remains the tendency of underestimation which increases with extension of the fuel slumping region to the core edge.

#### References

- 1) Takano H., et al.: JAERI Fast Reactor Group Constants Set, Version II, JAERI 1255 (1978).
- 2) Fowler T., et al.: Nuclear Reactor Core Analysis Code: CITATION, ORNL-TM\_2496 (1969).
- 3) Benoist P.: Streaming Effects and Collision Probabilities in Lattices, Nucl. Sci. Eng. 34 (1968).
- 4) Collins P.G., Ingram G., Codd J.: Proc. Int. Symp. Phy. Fast Reactors, Tokyo, Oct. 16-19, A40 (1973).

Table 3.2.1 Calculated and experimental reactivity changes for the fuel slumping of normal SS system

Pattern	Calculation ( $10^{-4} \Delta k/k$ )		Experiment ( $10^{-4} \Delta k/k$ )	C - E ( $10^{-4} \Delta k/k$ )	
	Conventional D	Modified* D		Conventional D	Modified D
A1	3.3	3.7	5.3±0.2	-2.0	-1.6
A2	6.2	8.6	12.6±0.3	-6.4	-4.0
A3	1.6	9.1	15.2±0.3	-13.6	-6.1
S	-6.3	-6.2	-4.1±0.2	-2.2	-2.1

\* Modified diffusion coefficients for a cavity containing a dilute material (Ref. 4) are used for the SS spacer region.

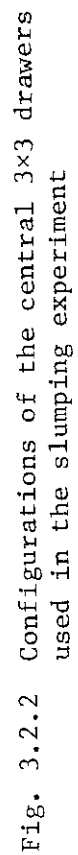


Fig. 3.2.1 RZ configuration of Assembly VIII-2

### 3.3 Fuel Slumping Experiment on FCA Assembly VIII-2 (II): Flux Distribution Change

M. Nakano, H. Tsunoda\* and J. Hirota

A study has been made of the distortion of neutron flux distribution due to fuel slumping in fast reactors, measuring fission rate, fission rate ratio and sample worth distributions in FCA Assembly VIII-2. A series of the experiments were performed on four patterns of the central 3 rows by 3 columns (equivalent radius 9.3 cm) different in the axial position and size of the fuel slumping region (A1, A2, A3 and S patterns)<sup>1)</sup>.

Axial fission rate distributions for  $^{238}\text{U}$  and  $^{235}\text{U}$  were measured by traversing micro fission chambers of depleted and enriched uranium in the center drawer and off-center one adjacent to the slumping region ( $r = 15.6$  cm). Axial distribution of Pu sample worth was measured using central four drawers in the slumping region. The main experimental results can be summarized as follows:

- i) Distortion of  $^{238}\text{U}$  fission rate distribution is 40 % at maximum both in the compacted and voided region.
- ii) Although  $^{235}\text{U}$  fission rate distribution is less distorted, it has a positive peak near the outside boundary of the voided region.
- iii) Distortion of neutron spectrum indicated by  $^{238}\text{U}/^{235}\text{U}$  fission rate ratio spreads over the fuel slumping region even into the axial blanket.
- iv) Pu sample worth distribution is distorted similarly to  $^{238}\text{U}$  fission rate distribution.

The analysis has been made using JAERI Fast Set Version II<sup>2)</sup>. In order to check the adoptability of computational methods used in analyzing core disruptive accidents, the results obtained by the three methods, transport (Sn), conventional and modified diffusion methods, were compared with the measured ones.

Figure 3.3.1 shows the axial distributions of  $^{235}\text{U}$  and  $^{238}\text{U}$  fission rate along the axis of Assembly VIII-2 A2. Agreement is good for  $^{235}\text{U}$  fission rate distribution, although a little discrepancy is observed in

---

\* Tohoku Unive.

the fuel slumping region. Conventional diffusion theory does not represent the measured  $^{238}\text{U}$  fission rates both in the fuel compacted and voided region. No significant improvement is achieved by the use of the modified diffusion method of changing the diffusion coefficient in the voided region<sup>3)</sup>, although it considerably improves the prediction of reactivity change<sup>1)</sup>. The results obtained by the transport theory with  $\text{S}_4\text{P}_0$  approximation fairly well agree with the measured ones.

Calculated and measured fission rate ratios in Assembly VIII-2 A2 are compared in Fig. 3.3.2. The diffusion calculation mispredicts the fission rate ratio F8/F5 in the slumping region, however it gives satisfactory results outside of the slumping region. For Pu sample worth, problems still remain in the fuel compacted region which need a more detailed analysis, although the use of transport theory improves the agreement to a large extent.

#### References

- 1) Nakano M., et al.: 3.2 of this report.
- 2) Takano H., et al.: "JAERI Fast Reactor Group Constants Set, Version II", JAERI 1255 (1978).
- 3) Collins P.G., et al.: Proc. Int. Symp. Phy. Fast Reactors, Tokyo, A40 (1973).

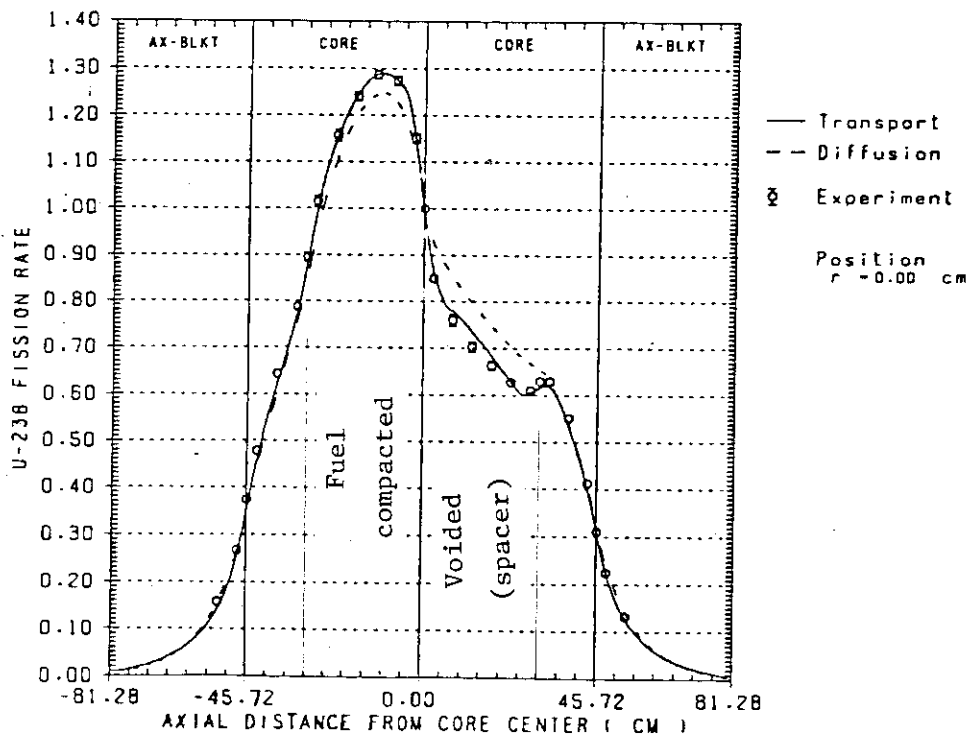
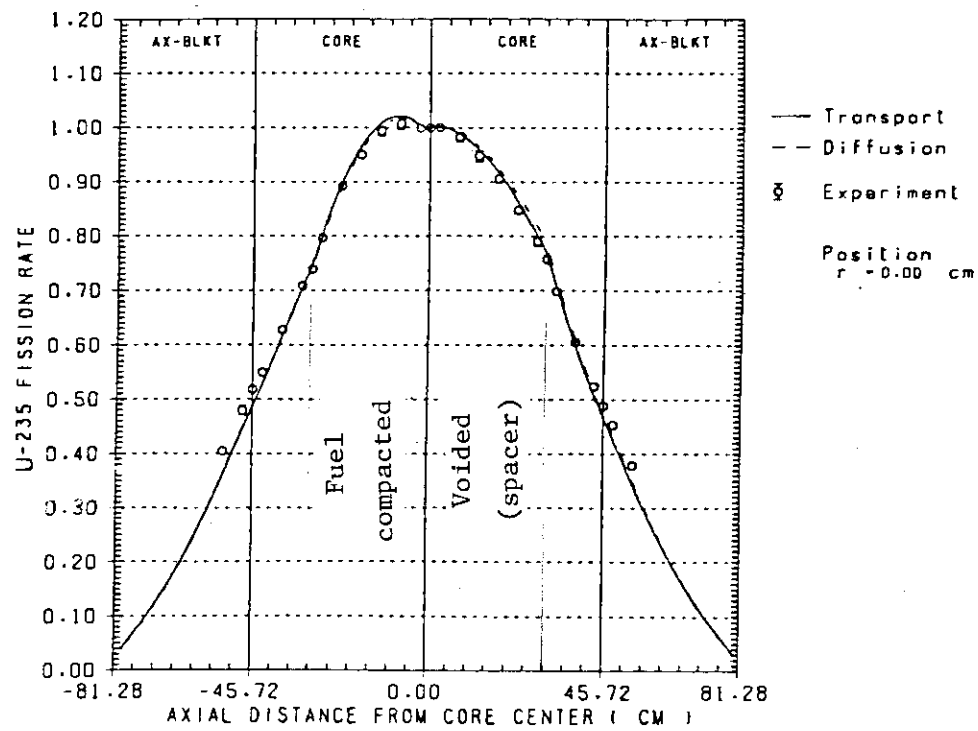


Fig. 3.3.1 Axial distribution of  $^{235}\text{U}$  and  $^{238}\text{U}$  fission rate in FCA VIII-2 A2 (center).

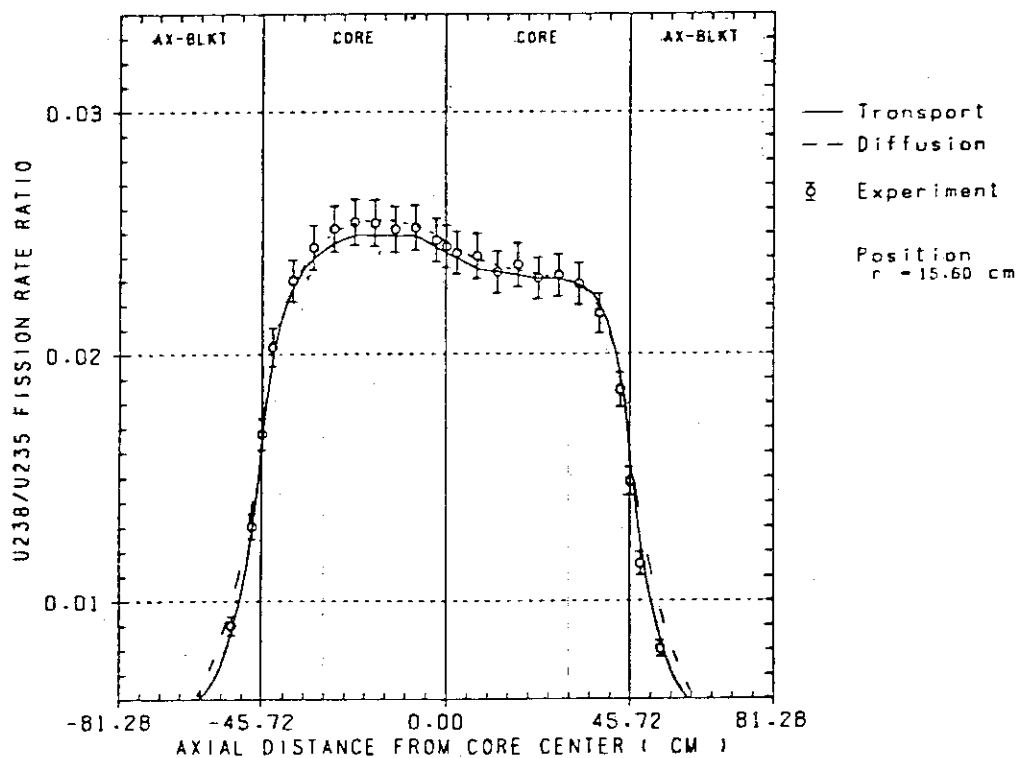
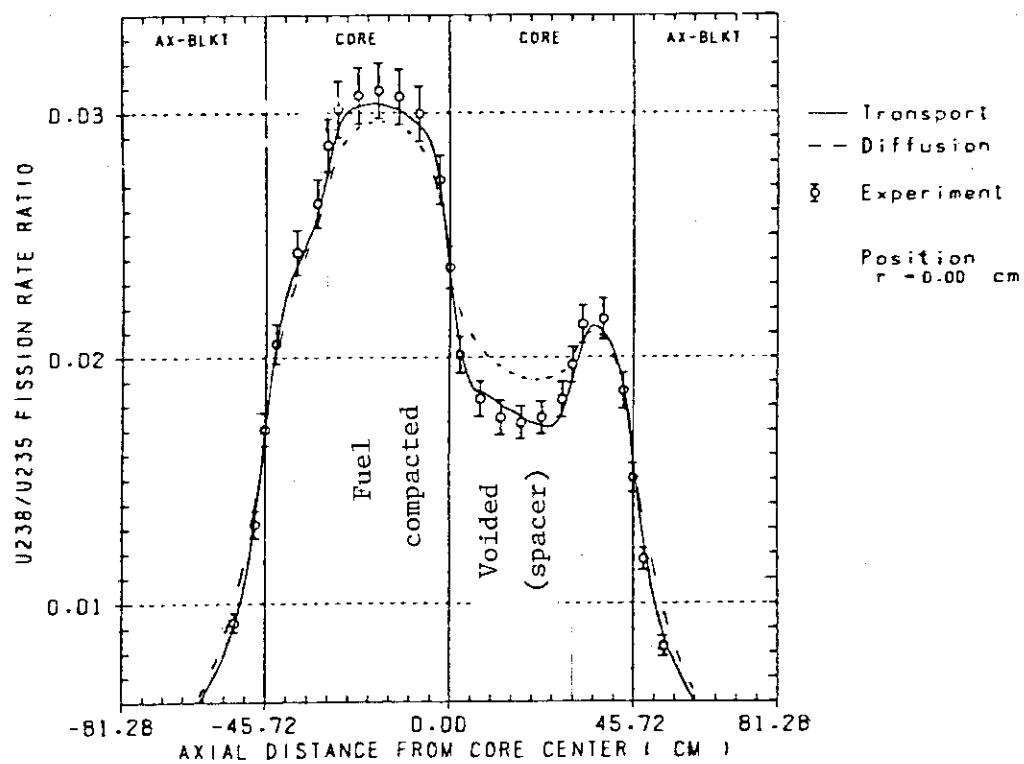


Fig. 3.3.2 Axial distribution of fission rate ratio  $F8/F5$  in FCA VIII-2 A2.

### 3.4 Analysis of Reaction Rate Distribution in Fast Critical Assemblies ZPPR-2, ZPPR-3 Phase 2 and MZB

M. Nakagawa, M. Hirota\* and Y. Matsui\*

Reaction rate distribution measured in fast critical assemblies has been analysed to evaluate the prediction accuracy and to examine the cause of the discrepancies between calculations and measurements. The selected assemblies are ZPPR-2<sup>1)</sup>, ZPPR-3 phase 2, MZB(2) and MZB(3)<sup>2)</sup>. The assembly ZPPR-2 is a benchmark core with a volume of 2400 litres, and ZPPR-3 phase 2 is an engineering mock-up assembly with six control rods and twelve sodium channels. The assemblies MZB(2) and MZB(3) are the mock-ups of the prototype fast reactor, MONJU.

The analysis has been performed by using the JAERI Fast set version 2 with 70 group structure<sup>3)</sup>. To estimate the influence of anisotropic scattering,  $P_3$  elastic scattering matrices have been produced with the use of the ENDFB/4 file. At first, the plate heterogeneity calculations were carried out by the SLAROM code<sup>4)</sup> to obtain the cell averaged effective cross sections. Then, they were collapsed into twenty groups by being weighted with neutron flux obtained in one dimensional diffusion or transport calculations. The two dimensional neutron flux has been calculated in x-y geometry by using the CITATION and TWOTRAN-2 codes.

The typical results are shown in the following. The mean values of C/E for ZPPR-2 are represented in Table 3.4.1. It shows that the calculations are in a good agreement with the measurements in the inner and outer core, and the standard deviations are less than 3 %. In the blanket region, the C/E for  $^{239}\text{f}$  decreases from 1.0 with increasing radius. In Fig. 3.4.1, the transport and anisotropic scattering effect is shown for the fission reaction of  $^{238}\text{U}$ . In the outer core and radial blanket, these effects are significant, but on  $^{239}\text{f}$  and  $^{238}\text{c}$ , they are several percents even in the outer-most part of the blanket.

In Table 4.3.2 the mean values of C/E are presented for  $^{235}\text{f}$  in ZPPR-3 phase 2. The measurements were made only in the core region. The table shows a good agreement between the calculation and the measurement over the whole region of core. The minimum values of C/E appear in the outer edge of the outer core.

---

\* Japan Information Service Co. Ltd. (Tokyo)



Table 3.4.3 shows the results for  $^{239}\text{f}$  and  $^{238}\text{f}$  in MZB(2) and MZB(3), respectively. The assemblies MZB(2) and MZB(3) have the same core configurations but their composition of the sector blanket are different. The table compares the results for the fission chamber measurements. It shows a fairly good agreement in the inner and outer cores for both the assemblies. In the blanket region, the quantity  $^{238}\text{f}$  is overestimated about 10 ~ 20 %. Though the C/E of  $^{239}\text{f}$  is almost constant in the blanket of MZB(2), it decreases gradually in the outer part of MZB(3). The difference of the composition in the sector blankets considerably influences the tendency of C/E. The results for  $^{235}\text{f}$  is similar to those for  $^{239}\text{f}$ .

The present work was performed under the contracts between Power Reactor and Nuclear Fuel Development Corporation and Japan Atomic Energy Research Institute.

#### References

- 1) Davey W.G., et al.: "Rod Plate Heterogeneity Studies in ZPPR-2", ANL-7961 (1974).
- 2) Ingram G., et al.: Tokyo conf. of fast reactor physics, A-16 (1973).
- 3) Takano H., et al.: "JAERI Fast Reactor Group Constants set, Version II", JAERI 1255 (1978).
- 4) Nakagawa M. and Tsuchihashi K.: "SLAROM: A Code for Calculation of Heterogeneous Core in Fast Reactor", JAERI-M 5916 (1974) (in Japanese)

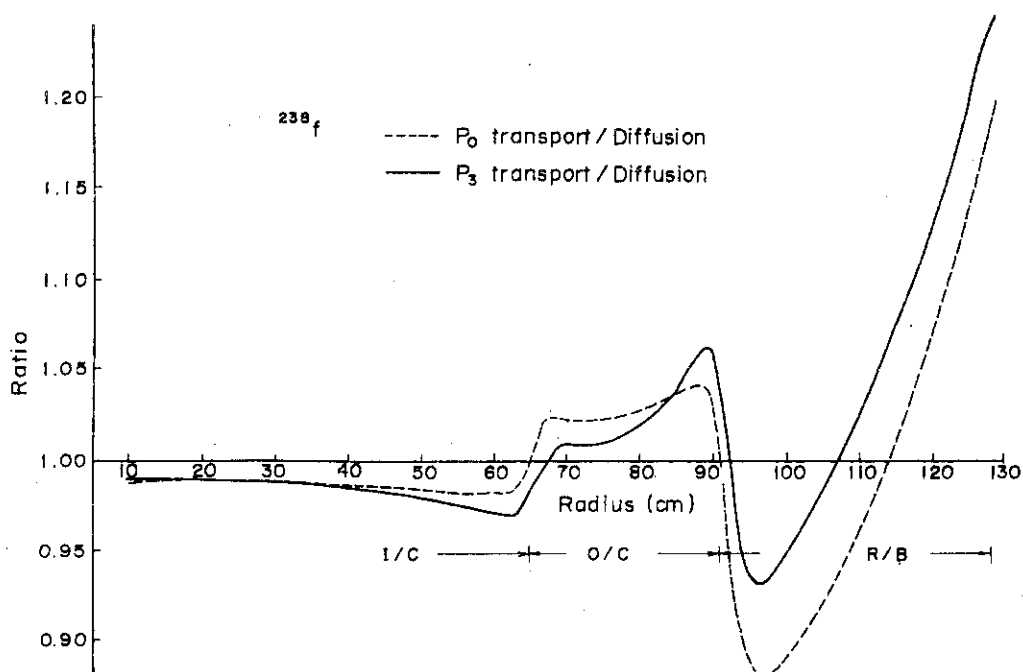


Fig. 3.4.1 Transport and anisotropic scattering effect of fission reaction rate distribution of  $^{238}\text{U}$

Table 3.4.1 Averages of (C/E) in ZPPR-2

	$^{239}\text{f}$	$^{238}\text{f}$	$^{238}\text{c}$
Inner core	$1.014 \pm .018^*$	$1.015 \pm .014$	$1.016 \pm .025$
Outer core	$1.028 \pm .029$	$1.006 \pm .016$	$1.016 \pm .027$
R/blanket	$1.021 \pm .048$	$0.965 \pm .063$	$0.965 \pm .069$

$$* \text{ one standard deviation } = \sqrt{\frac{\sum \frac{(1-C/E)^2}{N}}{N}}$$

Table 3.4.2 Averages of (C/E) for  $^{235}\text{f}$  in ZPPR-3 phase 2

	C/E	Max.	Min.
Inner core	1.002±.012	1.035	0.967
Outer core	0.990±.020	1.033	0.953
Core total	0.996±.017	1.035	0.953

Two dim. diffusion calculation

Table 3.4.3 Comparison of  $^{239}\text{f}$  and  $^{238}\text{f}$  reaction rate radial traverse in MZB(2) and MZB(3) (counter)

C/E Distance (cm)		$^{239}\text{f}$		$^{238}\text{f}$	
		MZB(2)	MZB(3)	MZB(2)	MZB(3)
I/C	0.0	1.00	1.00	1.00	1.00
	16.4	1.01	1.00	1.00	1.00
	32.5	1.00	1.00	1.00	1.00
	48.9	1.00	0.99	0.99	1.00
	57.5	1.00	0.99	0.99	1.01
	59.6	1.00	1.00	0.99	1.00
	61.8	0.99	0.99	0.98	0.99
	63.9	1.00	1.00	0.97	0.99
O/C	66.1	0.99	0.99	0.97	0.99
	70.6	0.98	0.97	0.98	0.99
	73.9	0.96	0.96	0.95	0.96
	76.0	0.96	0.94	0.94	0.96
	78.1	0.97	0.96	0.98	0.99
	80.3	0.97	0.96	1.07	1.05
	82.5	0.98	0.96	1.11	1.12
	86.7	0.98	0.96	1.05	1.00
R/B	92.0	0.98	0.92	1.15	1.06
	97.7	0.96	0.89	1.19	1.01
	103.1	0.98	0.84	1.21	0.97
	108.5	1.05	0.84	1.28	0.95

Two dim.  $P_3$ ,  $S_8$  transport calculation

### 3.5 Actinides Cross Section Evaluation by Integral Data and Experimental Program proposed at FCA<sup>1)</sup>

T. Mukaiyama, H. Mitani, K. Koyama, M. Obu and H. Kuroi

The assessment of the actinide recycle concept requires the reliable fission and capture cross section data of the actinide isotopes over the whole energy spectrum of potential actinide recycling systems. The reliability of the prediction of reactor physics parameters depends upon "the data and the method" used. As far as actinides are concerned, the "data" available at present are much less reliable than the "method".

For the assessment of the actinide recycle concept, the actinide element 25-group ENDL set was generated<sup>2)</sup> using the Evaluated Nuclear Data Library of Lawrence Livermore Laboratory<sup>3)</sup> as the source data. The different sets of one-group cross sections of actinides were compared to know the status of actinide cross sections<sup>2)</sup>. Considering the effect of differences in weighting functions used when collapsing multi-group cross sections into one-group set, there still exist big differences between the sets especially in the capture cross section. The uncertainties in the cross sections of actinides are assumed (Table 3.5.1) as the reference uncertainty set to study the cross section uncertainty effect upon the characteristics of the actinide transmutation system.

Actinide Burning Reactor ABR is chosen as the actinide transmutation system. ABR utilizes the oxide of actinide mixture recovered from the wastes generated by reprocessing LMFBR fuel of 80,000 MWD/MT and LWR fuel of 33,000 MWD/MT. Recycling calculation has been made for the irradiation of  $1 \times 10^{16}$  neutron/sec $\cdot$ cm<sup>2</sup> for 300 days and 300 days cooling per cycle using the code system developed for this study (Fig. 3.5.1). At the beginning of each cycle, the criticality is adjusted by feeding the fresh actinide mixture from the reprocessing. The effect of the cross section uncertainties upon the atom density of ABR is calculated for the cross section uncertainties given in Table 3.5.1 and the atom density uncertainties in the final state of 1st and 20th cycle are given in Table 3.5.2. This atom density uncertainties cause 3 % and 17 % actinide fuel volume uncertainties at the final state of 1st and 20th cycle, respectively. The multiplication factor uncertainty due to errors of actinide cross sections is calculated under the different

correlation conditions and for the cross section uncertainties of Table 3.5.1. The result is shown in Table 3.5.3.

#### Program of Integral Experiments in FCA to improve the Accuracy of Actinide Cross Sections

Contribution of the integral data to the improvement of the multi-group cross section data is shown by the theory of least square fitting of cross sections utilizing integral data<sup>4)</sup>.

The small sample perturbation and the reaction rate ratio are the realistic integral data of the actinide elements because of the high reactivity of actinides and the difficulty of obtaining pure samples. The integral measurements are very accurate, but the information with respect to the energy dependency is not so straightforward. Therefore, the choice of appropriate variety of neutron spectra where integral measurements are taken place is most important to obtain a successful result for improving cross section data.

The six to eight cores are to be built at FCA to cover a wide range of neutron spectra. Iron, graphite and natural uranium are to be used for shifting neutron spectrum appropriately. The sample perturbations of 15 ~ 20 gr of  $^{238}\text{Pu}$ ,  $^{240}\text{Pu}$ ,  $^{237}\text{Np}$ ,  $^{241}\text{Am}$  and  $^{243}\text{Am}$ , and the fission rate ratios are to be measured in these cores.

The uncertainty of the group cross section can be reduced by factor 2 to 5 for the important energy region of fast reactors after adjusted by the least square fitting of integral data when measured with 3 % error.

#### References

- 1) Mukaiyama T., et al.: "Evaluation of Actinide Cross Sections by Integral Experiments in Fast Critical Assembly FCA" Proceeding of Intnl. Conf. on Nuclear Cross Sections for Technology ED3 (Knoxville, Oct. 1979).
- 2) Mukaiyama T., Koyama K. and Kuroi H.: "Generation of Actinide Isotopes Cross Section Set for Fast Reactor Calculations using Data from ENDL and ENDF/B-IV". JAERI-M 8310 (1979).
- 3) Howerton R.J., et al.: "The LLL Evaluated Nuclear Data Library (ENDL)", UCRL-50400 Vol.15 Part A (1975) and Part B (1976).
- 4) Mitani H. and Kuroi H.: J. Nucl. Sci. Technol. 9, 383 (1972).

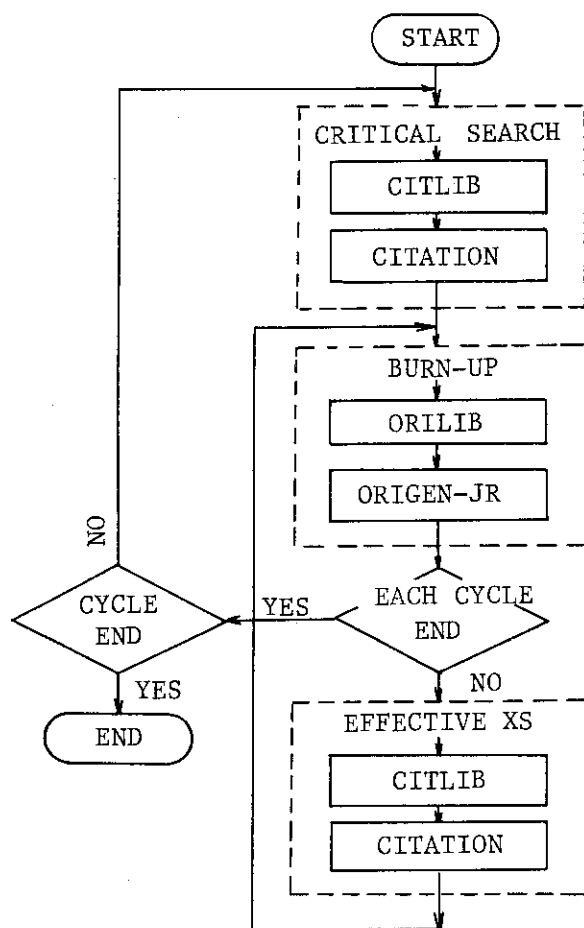


Fig. 3.5.1 Flow of actinide transmutation analysis code system

Table 3.5.1 Estimated Cross Section and Decay Constant Uncertainties (%)

Nuclide	$\lambda$	$\sigma_f$	$\sigma_c$	$\sigma_{n,2n}$
U-235	2	5	5	40
U-236	2	15	25	50
U-237	1	25	50	
U-238	3	5	5	40
Np-236	1	30	50	
Np-237	2	20	40	50
Np-238	1	30	50	
Np-239	1	30	50	
Pu-238	1.5	20	50	
Pu-239	1	5	5	40
Pu-240	5	10	20	40
Pu-241	5	10	20	40
Pu-242	5	20	30	50
Am-241	2	30	40	
Am-242m	2	30	50	50
Am-242	1	30	50	50
Am-243	2	30	50	
Cm-242	2	30	50	
Cm-243	3	30	50	50
Cm-244	3	30	50	
Cm-245	3	30	50	

Table 3.5.2 Effect of Cross Section Uncertainties<sup>a</sup> on Actinide Atom Density in ABR (%)

Isotope	Uncertainty of Atom Density (%)	
	1st cycle	20th cycle
U-235	2.2	5.4
U-236	29.1	17.6
U-237	8.6	26.3
U-238	11.9	32.4
Np-237	7.4	30.5
Pu-238	18.9	32.9
Pu-239	2.4	41.7
Pu-240	2.5	26.4
Pu-241	7.2	26.0
Pu-242	10.9	31.5
Am-241	5.6	25.9
Am-242m	39.2	39.2
Am-243	4.9	31.7
Cm-242	29.2	29.8
Cm-243	52.7	61.7
Cm-244	25.7	39.3
Cm-245	52.8	63.9

a. cross section uncertainties given in Table 1  
one cycle; 300days irradiation ( $1 \times 10^{16} \text{ n/sec} \cdot \text{cm}^2$ ),  
300days cooling

Table 3.5.3 Uncertainty in Multiplication Factor of ABR due to Cross Section Uncertainties<sup>a</sup>

CASE <sup>b</sup>	1st cycle		20th cycle	
	cap. fiss.		cap. fiss.	
A	7.3%	11.%	8.5%	17.%
B	4.6	6.0	7.0	12.0
C	2.4	4.2	3.0	6.5
D	1.6	2.3	2.5	4.4

a. cross section uncertainties given in Table 1

b. Case A: full correlation between errors in different energy groups and between errors in different nuclides,

Case B: full correlation between errors in different energy groups only,

Case C: full correlation between errors in different nuclides only,

Case D: no correlation.

#### 4. Shielding

##### 4.1 Effect of Iron Cross Section Valley at 24.4 keV on Neutron Penetration

N. Yamano\* and K. Koyama

The self-shielding factor method<sup>1)</sup> for preparing group cross sections has been widely used, particularly for fast reactor design and for the analysis of critical experiments. However, it was reported that calculations for shielding problems containing iron had often failed to achieve the expected accuracy<sup>2,3)</sup>. In this study, validity of self-shielded cross section for neutron penetration problems of iron 27.67 keV resonance has been evaluated by comparing the results of transport calculations with ultra-fine group cross sections based on the infinite dilution approximation.

The ultra-fine group cross sections and effective ones with coarse group structures used for the calculations were generated by FAIR-CROSS module of RADHEAT-V4<sup>4)</sup> code system by processing the evaluated nuclear data in JENDL-2. Group structures of the cross sections are described in Table 4.1.1. Calculated total cross sections and the Bondarenko-type self-shielding factors of natural iron are shown in Fig. 4.1.1. It was shown that the effect of self-shielding on the total cross section can be ignored except for the 22.8 keV p-wave resonance in the ultra-fine group structure. On the contrary, the self-shielding contributions increased according as the energy width of each group cross section became large. Penetration calculations with the group structures shown in Table 4.1.1 were performed in the case of iron sphere by using one dimensional  $S_N$ -transport code DIAC<sup>5)</sup> with  $S_{16}$  approximation. Neutron source with a flat energy distribution of 29.7 keV through 31.8 keV was considered up to 2 cm from the center of sphere.

Calculated neutron spectra and inverse total cross sections in the sphere of natural iron and of pure  $^{56}\text{Fe}$  are shown in Figs. 4.1.2 and 4.1.3, respectively. In these figures, the energies of the spectral dips of the ultra-fine group fluxes agree with those of the dips of the inverse total cross sections. However, the energies of the spectral peaks do

---

\* Sumitomo Atomic Energy Industries, Ltd.



not agree even though the results obtained with the fine-group structures.

In the Bondarenko method, the weighting flux is assumed to vary in proportion to  $(\sigma_0 + \sigma_t)^{-1}$ , where  $\sigma_t$  is the total microscopic cross section and the parameter  $\sigma_0$  is used to allow for other materials and heterogeneity. In this study, the parameter  $\sigma_0$  is zero because of a very large assembly of pure iron so that the self-shielding factor is produced by the weighting flux expressed as the inverse total cross section. However, calculated neutron fluxes are not shown by the narrow resonance approximation so that the self-shielding effect is not expressed accurately in the coarse-energy-grained group cross sections.

Maximum reaction rate changes comparing the results of the ultra-fine group calculations for  $1/v$ -absorber, flat-energy absorber and dosimeter are shown in Tables 4.1.2 and 4.1.3. The errors caused by the self-shielding factor are clearly shown in these tables.

It was shown in this study that the penetrating neutrons over the large s-wave resonances were not calculated correctly by using the self-shielding factor method. To eliminate the errors, it is necessary to estimate the weighting fluxes within the ultra-fine group structures. However, the weighting fluxes vary for the spatial region in each problem, so that a difficulty exists to estimate the correct values of weighting spectra.

It was concluded that the adequate energy group structures must be considered to evaluate penetrating neutrons for iron which has many resonance structures.

#### References

- 1) Bondarenko I.I., Ed.: "Group Constants for Nuclear Reactor Calculations", Consultants Bureau, New York (1964).
- 2) Malaviya B.K., et al.: Nucl. Sci. Eng., 47, 329 (1972).
- 3) MacFarlane R.E. and Becker M.: Trans. Am. Nucl. Soc., 22, 668 (1975).
- 4) Koyama K., et al.: Preprint 1979 Annu. Meeting of AESJ, F33, (1979).
- 5) Yamano N., Koyama K. and Minami K.: J. Nucl. Sci. Technol., 16[12], 919 (1979).

Table 4.1.1 Group structures<sup>+</sup> used in the calculations

I.	100 groups with an equi-lethargy width of 0.00625
II.	50 groups with an equi-lethargy width of 0.0125
III.	25 groups with an equi-lethargy width of 0.025
IV.	10 groups with an equi-lethargy width of 0.0625

+ Energy ranges of the group cross sections are same values of 17.036 keV through 31.828 keV.

Table 4.1.2 Maximum changes of reaction rates in natural iron

Reaction type	Changes of reaction rates	
	II/I (7 cm)*	IV/I (14 cm)
1/v-absorber	+0.60 %	+12.18 %
flat-absorber	+0.62	+12.89
dosimeter	+0.66	+14.06

\* means the change of result at the distance of 7 cm from the center of sphere with group structure II compared with the result of group structure I, described in Table 4.1.1.

Table 4.1.3 Maximum changes of reaction rates in <sup>56</sup>Fe

Reaction type	Changes of reaction rates	
	II/I (6 cm)*	IV/I (29 cm)
1/v-absorber	+0.39 %	+30.56 %
flat-absorber	+0.43	+31.70
dosimeter	+0.49	+33.52

\* Same means of Table 4.1.2.

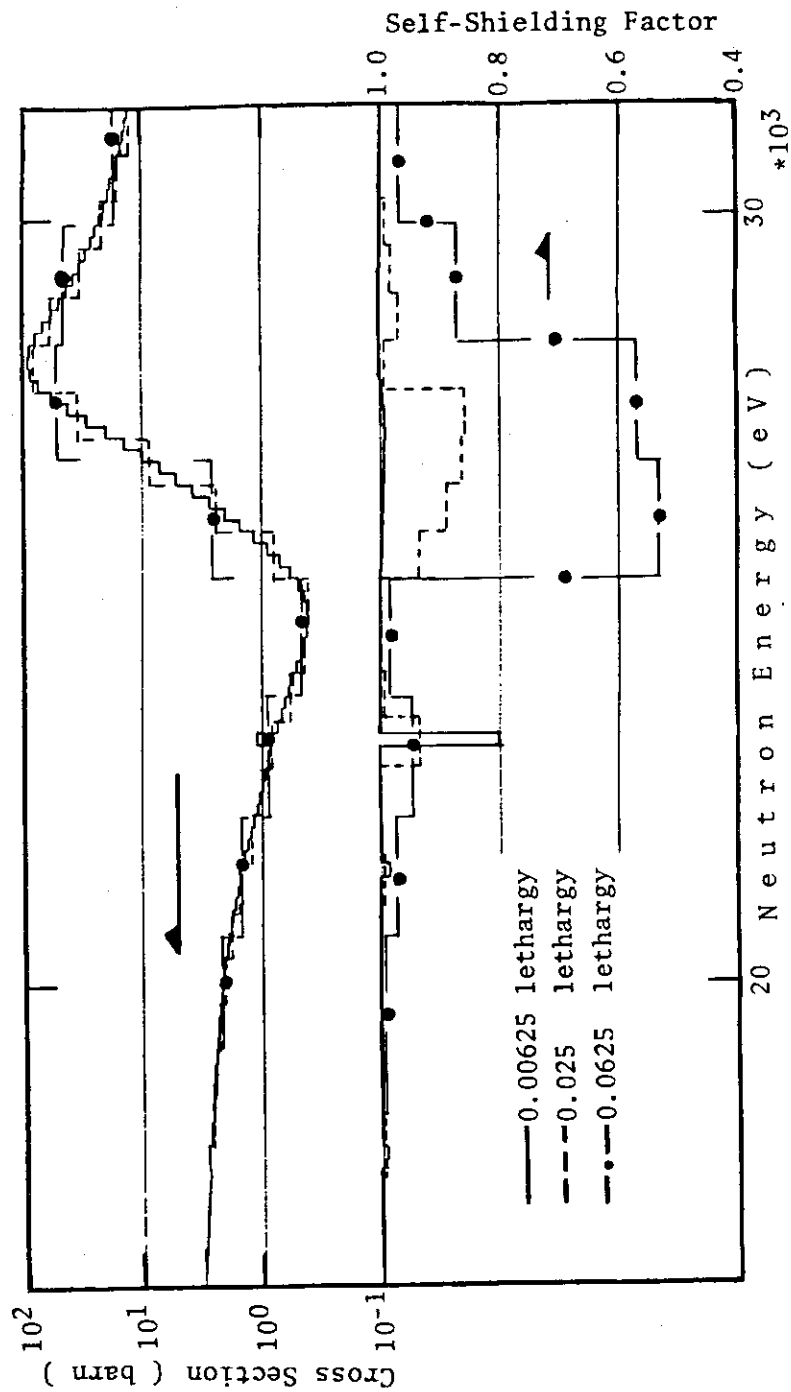


Fig. 4.1.1 Cross section and self-shielding factor of natural iron

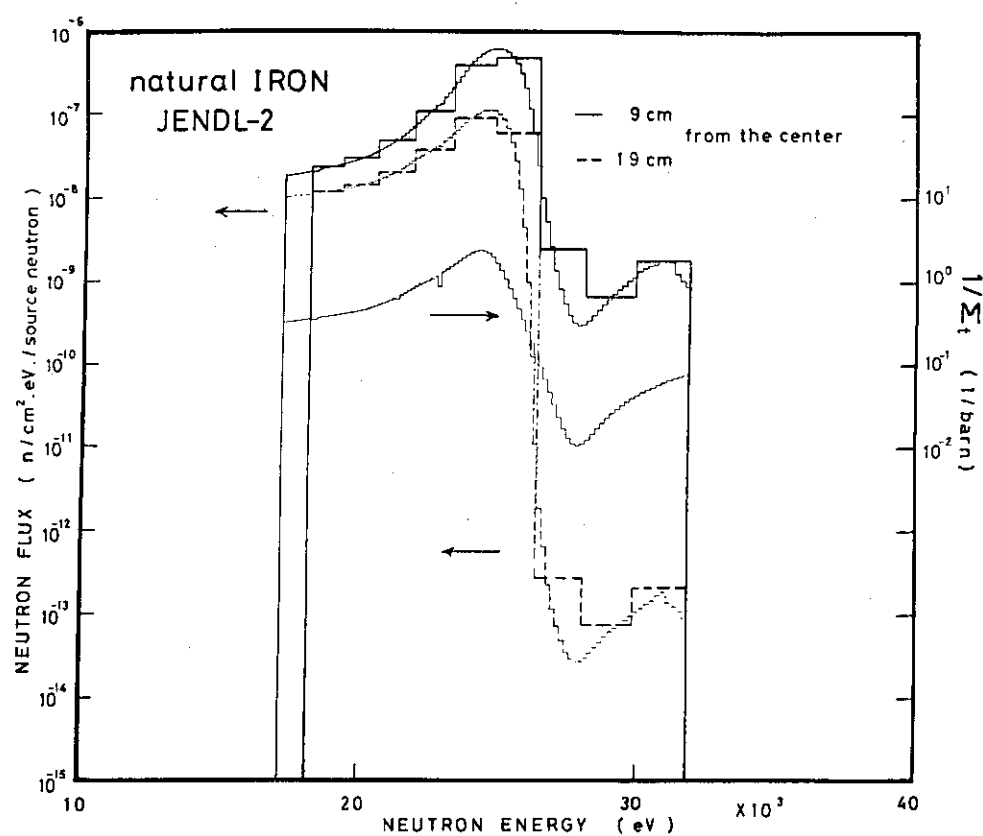
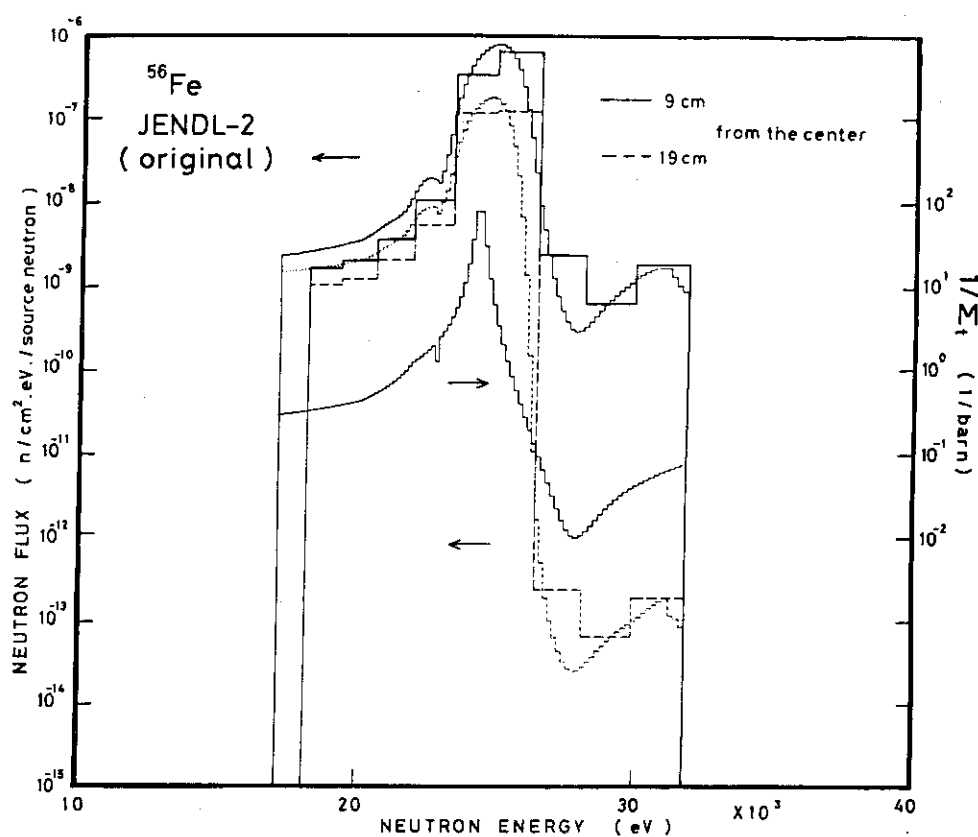


Fig. 4.1.2 Neutron spectra of natural iron calculated by DIAC

Fig. 4.1.3 Neutron spectra of  $^{56}\text{Fe}$  calculated by DIAC

4.2 Effect of  $^{56}\text{Fe}$  Angular Anisotropy of Neutron Penetration

N. Yamano\*, K. Koyama and M. Kawai\*\*

Neutron penetration into  $^{56}\text{Fe}$  with angular anisotropy over the 27.67 keV resolved resonance minimum has been investigated. Angular distributions of elastic scattering cross sections over the large s-wave resonances of  $^{56}\text{Fe}$  were measured with high resolution and it was shown that the angular anisotropy exists over the resonance<sup>1)</sup>. To calculate the angular distributions, theoretical formula<sup>2)</sup> is used as follows:

$$\sigma(E, \theta) = \frac{\sigma_0}{4\pi} \sum_{L=0}^{\infty} B_L(x) P_L(\cos\theta), \quad (1)$$

where  $x = (E - E_0)/(\Gamma/2)$  and  $\sigma_0 = 4\pi/k_0^2$ .

The components of Legendre coefficients are given as follows:

$$B_L = \frac{\Gamma_{\text{no}}}{\Gamma} \frac{1}{1+x^2} \delta_{L,0} + H_L + \frac{\Gamma_{\text{no}}}{\Gamma} \frac{2(2L+1)}{1+x^2} \sin \delta_L \{ x \cos(2\delta_0 - \delta_L) - \sin(2\delta_0 - \delta_L) \}, \quad (2)$$

$$H_L = \sum_{\ell=0}^{\infty} \sum_{\ell' = |\ell-L|}^{\ell+L} (2\ell+1)(2\ell'+1)(\ell\ell'00|L0)^2 \sin \delta_\ell \sin \delta_{\ell'} \cos(\delta_\ell - \delta_{\ell'}), \quad (3)$$

and the phase shift  $\delta_\ell$  for hard sphere scattering is given by

$$\tan \delta_\ell = -j_\ell(\rho)/n_\ell(\rho), \quad (4)$$

where  $\rho = k_0 R'$   $R'$  being the scattering radius.

Numerical calculation was performed for  $^{56}\text{Fe}$  up to eighth order of Legendre coefficients by assuming  $R' = 5.4 \text{ fm}^2$ ) and  $\Gamma_\gamma \ll \Gamma \ll E_0$ . Adopted resonance parameters of  $\Gamma$ ,  $\Gamma_\gamma$  and  $E_0$  are 1300 eV, 1.4 eV and 27.67 keV, respectively. Total cross sections calculated by Eq. (1) and experimental data<sup>3)</sup> are shown in Fig. 4.2.1. A good agreement is obtained.

---

\* Sumitomo Atomic Energy Industries, Ltd.

\*\* Nippon Atomic Industry Group Co., Ltd.

Figure 4.2.2 shows the ratios of  $B_L$  to  $B_0$ . The nature of the angular anisotropy is expressed by rapid changes of  $B_1/B_0$  and  $B_2/B_0$ . It is clearly shown that the forward scattering components are extremely large for the neutron energy just below the resonance minimum. To assess the effect of the angular anisotropy on the penetrating neutrons, temporary nuclear data were produced by editing the angular information into evaluated nuclear data in JENDL-2 and one-dimensional transport calculations were performed in the case of  $^{56}\text{Fe}$  bulk sphere of 50 cm radius. Group cross sections with ultra-fine group structure (an equi-lethargy width of 0.00625) were produced by FAIR-CROSS module of RADHEAT-V4 code system. The transport calculations were performed by DIAC<sup>4)</sup> code with  $S_{16}$  approximation. Neutron source with a flat energy distribution over 29.7 keV through 31.8 keV was given up to 2 cm from the center of sphere.

Penetrating neutron spectra and the ratio of the spectrum with considering angular anisotropy to the result with original data of  $^{56}\text{Fe}$  in JENDL-2 are shown in Figs. 4.2.3 and 4.2.4, respectively. Spectral peak was shifted from 24.6 keV to 24.4 keV by considering the angular anisotropy. Neutron fluxes at the energy of the spectral peak and below the resonance minimum increased no more than 10 percent except for the energies of 21.6 and 22.9 keV at the distance of 50 cm from the center of sphere. Two peaks at the energies of 21.6 and 22.9 keV in Fig. 4.2.4 may be due to the effect of the back scattering contributions just above the resonance minimum but not of the p-wave resonance at the energy of 22.8 keV. The contributions of the angular anisotropy for dosimeter and  $1/v$ -absorber which located at the 18 cm from the center of sphere were about 2.0 and 2.2 percent, respectively. These results may be true for other  $^{56}\text{Fe}$  resonances, although a kind of detector and source condition were limited in this study. It seems that the effects of the angular anisotropy over other  $^{56}\text{Fe}$  resonances are not so remarkable because the resonance minima are not deep like the 27.67 keV resonance. Therefore, it has been concluded that the angular anisotropy over the resonance minima does not affect much on neutron penetrations such as shielding problems.

#### References

- 1) Perey F.G., et al.: "Neutron Data of Structural Materials for Fast Reactors", Proc. Specialist Meeting, Geel, p.530 (1977), Pergamon Press.

- 2) Iijima S. and Yamakoshi H.: J. Nucl. Sci. Technol., 17[6], 474 (1980).
- 3) Liou H.I., et al.: Nucl. Sci. Eng., 70, 150 (1979).
- 4) Yamano N., Koyama K. and Minami K.: J. Nucl. Sci. Technol., 16[12], 919 (1979).

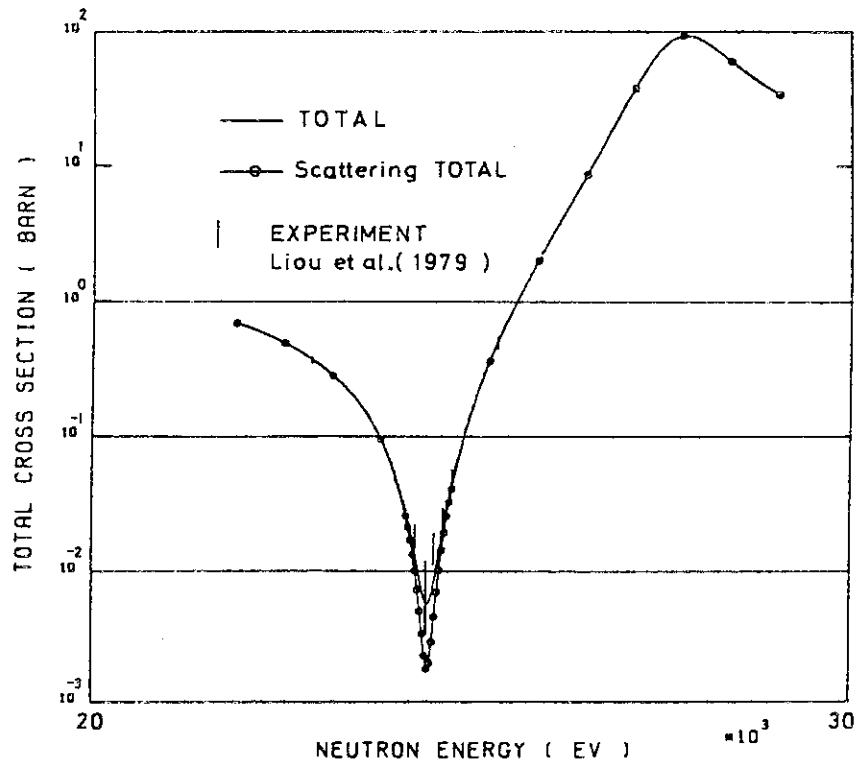


Fig. 4.2.1 Total cross section of  $^{56}\text{Fe}$  calculated by the analytical formula

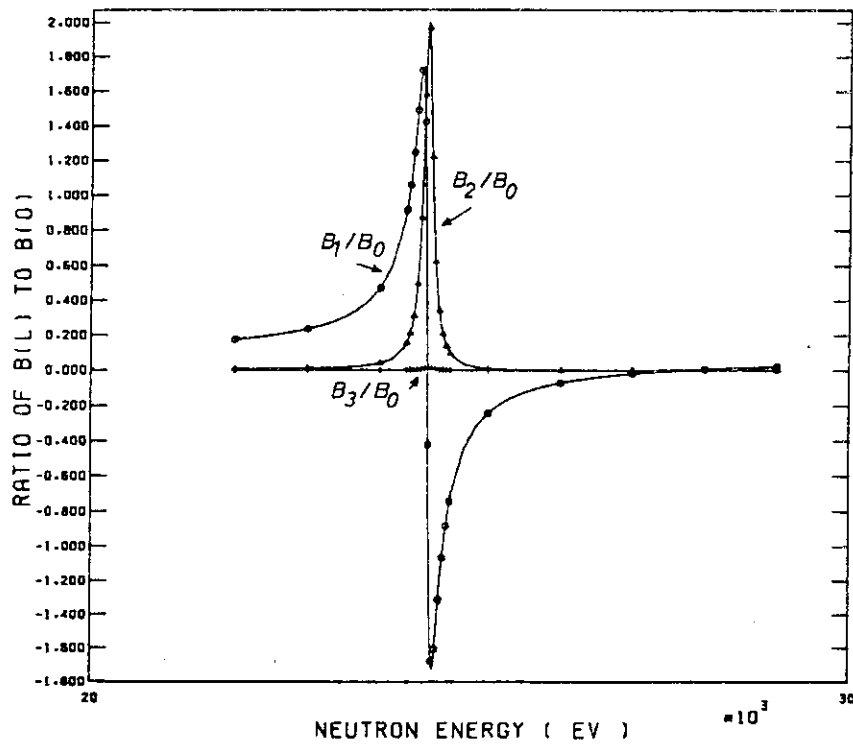


Fig. 4.2.2 Values of  $B_1/B_0$  calculated by the analytical formula



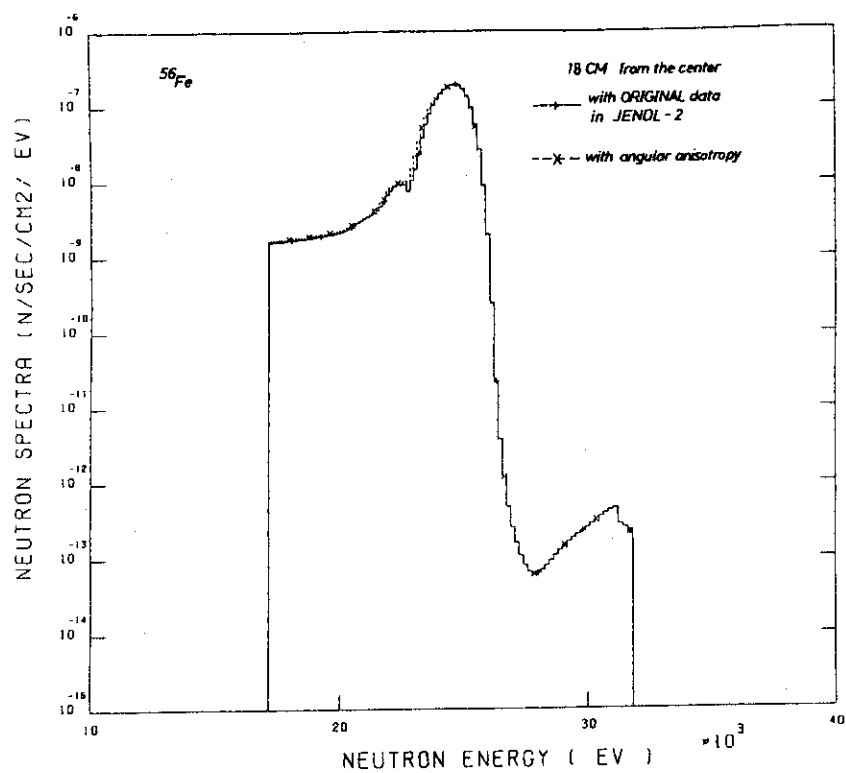
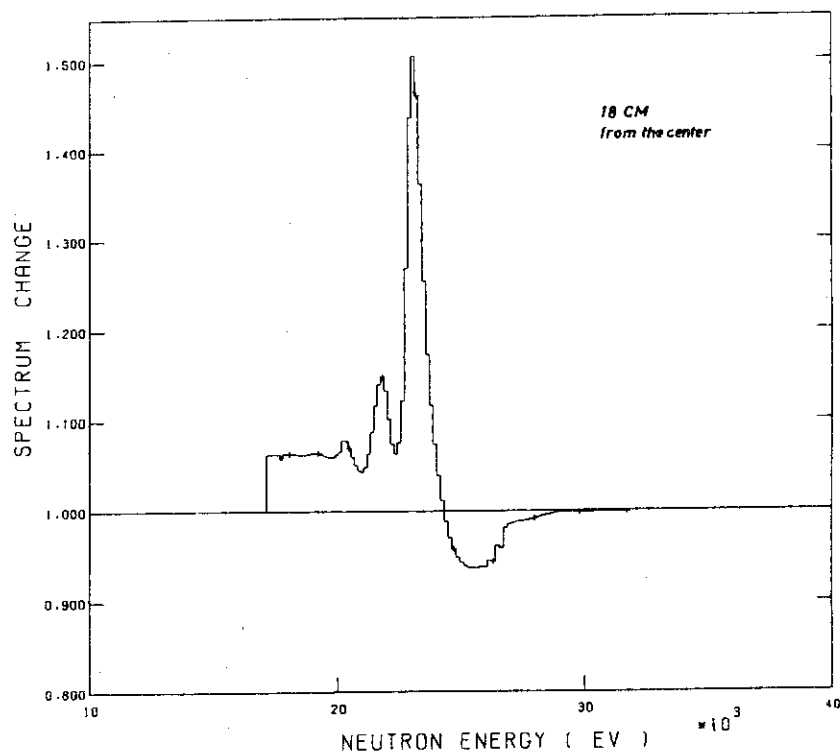


Fig. 4.2.3 Calculated neutron spectra

Fig. 4.2.4 Spectrum change by considering the angular anisotropy of  $^{56}\text{Fe}$

### 4.3 A Computational Method for Anisotropic Transmission Problems by $S_N$ -Transport Code

N. Yamano\*, K. Koyama and K. Minami\*\*

In many deep-penetration transport and streaming calculations, the angular flux distribution is a basic quantity for evaluating the radiation current in shield regions. Various attempts have been made for describing more precisely the anisotropic scattering of radiations in order to determine the angular flux distributions. One of the recent outstanding results is the use of the discrete ordinate  $S_N$ -transport calculation by expressing the anisotropic scattering cross section with the Legendre expansion of the cosine of the scattering angle.

However it is known<sup>1,2,3)</sup> that the  $S_N$ -transport calculation gives the negative angular fluxes remarkably when a strong anisotropic source is present in the shielding material.

To perform more precise evaluation of the angular fluxes, a new one-dimensional  $S_N$ -transport method has been developed. The method makes use of the probability function  $P_{i,m' \rightarrow m,j' \rightarrow j}$  to eliminate the fitting error due to the finite Legendre expansion. Scattering sources are given by integrating directly the probability function about energy  $E_j' \rightarrow E_j$  and solid angle  $\mu_m' \rightarrow \mu_m$ . The probability function  $P$  is generated from the group to group transfer cross sections as a function of scattering angle, by RADHEAT-V4<sup>4)</sup> code system.

In the present study, the scattering integral  $Q$  is defined as follows:

$$Q(\vec{r}, \mu_m, E_j) = \sum_j \sum_m W_m' \phi(\vec{r}, \mu_m', E_j') P(\vec{r}, \mu_m' \rightarrow \mu_m, E_j' \rightarrow E_j). \quad (1)$$

where

$$P(\vec{r}, \mu_m' \rightarrow \mu_m, E_j' \rightarrow E_j) = \frac{1}{W_m W_m'} \int_{\Delta\mu_m} \int_{\Delta\mu_m'} \int_0^\pi \Sigma_s(\vec{r}, E_j' \rightarrow E_j, \eta) d\phi' d\mu' d\mu \quad (2)$$

= probability function which a particle having an energy  $E_j'$  and a direction cosine  $\mu_m'$  is scattered to energy  $E_j$  and a direction cosine  $\mu_m$  at a position  $\vec{r}$ ,

---

\* Sumitomo Atomic Energy Industries, Ltd.

\*\* Fujitsu Limited.

and  $w_m$  is a weight function for the angular mesh.

For applying this method to the conventional  $S_N$ -transport code using the Legendre expansion, any changes in the algorithm are not needed. We have introduced the present approach to the  $S_N$ -transport code, ANISN-JR<sup>5)</sup> and the improved version is named DIAC.

In order to grasp the characteristics of the method, a test calculation was carried out and compared with exact solution.

The uncollided scalar flux from a plane source with a cosine angular distribution is calculated in an infinite medium. As shown in Fig. 4.3.1, a good agreement is obtained between the DIAC result and the exact solution. The difference between these results is only 0.5 %.

The next problem deals with a paraffin slab configuration with a plane monodirectional source incident normally to the left surface of the slab as shown in Fig. 4.3.2, where the angular flux is not symmetric due to a strong anisotropy of the source. The angular flux calculated by ANISN-JR in the  $P_5$ - $S_{16}$  approximation takes negative values in some angles due to the fitting error of the scattering source by the finite Legendre expansion. The angular flux calculated by DIAC, however, does not take any negative value for all directions.

From above test calculations, it is shown that the method applied to DIAC is effective for eliminating negative values and oscillations of the angular flux in anisotropic  $S_N$ -transport calculations. In order to evaluate the accurate angular flux in a medium having an anisotropic source or a strong streaming, it will be necessary to use the method which can calculate the radiation transport without using the Legendre expansion for expressing the anisotropic components.

#### References

- 1) Timmons D.H.: Trans. Am. Nucl. Soc., 16 350 (1973).
- 2) Yamano N., et al.: 1977 Fall Meeting of the Atomic Energy Society of Japan, C34 (1975).
- 3) Takahashi A., et al.: J. Nucl. Sci. Technol., 16 (1), 1 (1979).
- 4) Koyama K., et al.: 1979 Annual Meeting of the Atomic Energy Society of Japan, F33 (1977).
- 5) Koyama K., et al.: "ANISN-JR, A One-Dimensional Discrete Ordinates Code for Neutron and Gamma-ray Transport Calculations", JAERI-M 6954 (1977).

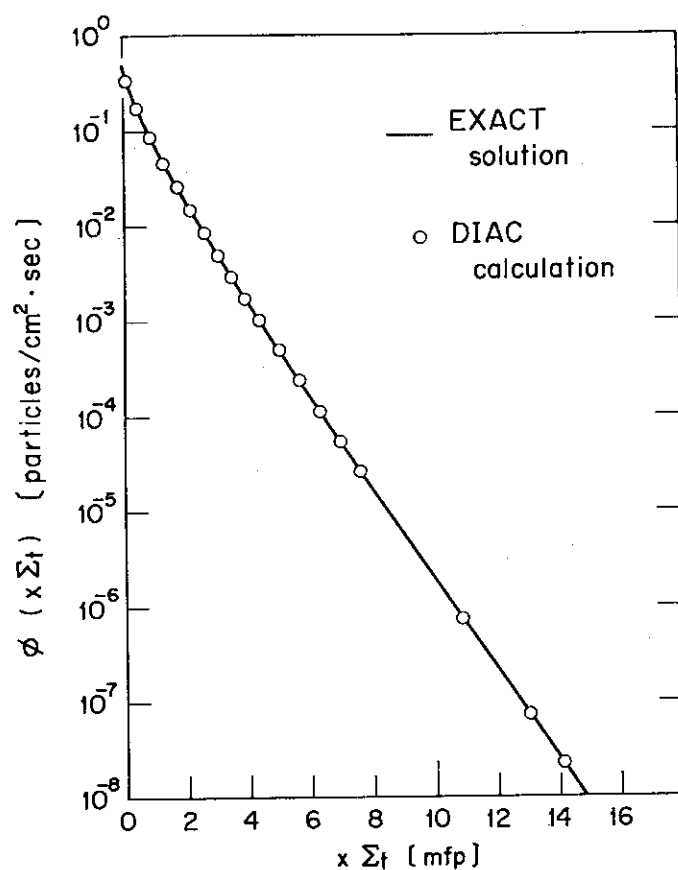


Fig. 4.3.1 Comparison between exact solution and DIAC calculation for the uncollided scalar flux in an infinite medium with a cosine distributed plane source. The exact solution is denoted by  $E_2(\times \Sigma_t)/2$ .

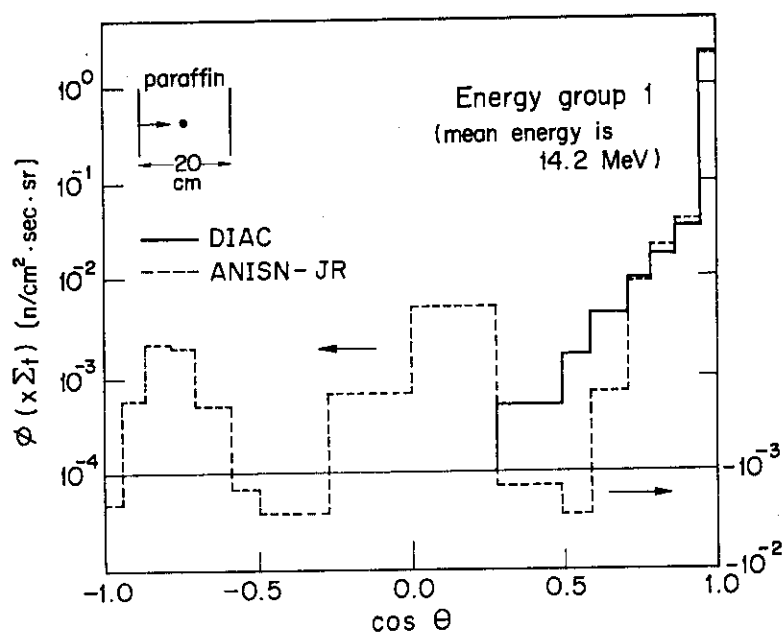


Fig. 4.3.2 Comparison between the angular fluxes at the center of paraffin calculated by DIAC and ANISN-JR for an paraffin slab with a plane monodirectional source incident normally to the left surface of the slab.

## 4.4 An Improvement of the PALLAS Discrete Ordinates Transport Code

N. Sasamoto and K. Takeuchi

An improvement was made in the approximation of the spatial distribution of the source term in the PALLAS discrete ordinates code by a combination of linear and exponential functions<sup>1)</sup>.

By integrating Boltzmann transport equation over a space variable along the direction of radiation motion, we obtain the analytical solution as

$$\begin{aligned} \Phi(\bar{r}, \bar{\Omega}_{pq}, E_j) &= \Phi(\bar{r}-R_0 \bar{\Omega}_{pq}, \bar{\Omega}_{pq}, E_j) \\ &\times \exp\left[-\int_0^{R_0} \Sigma_t(\bar{r}-R'' \bar{\Omega}_{pq}, E_j) dR''\right] \\ &+ \int_0^{R_0} Q(\bar{r}-R' \bar{\Omega}_{pq}, \bar{\Omega}_{pq}, E_j) \\ &\times \exp\left[-\int_0^{R_0} \Sigma_t(\bar{r}-R'' \bar{\Omega}_{pq}, E_j) dR''\right] dR' , \end{aligned} \quad (1)$$

where  $R_0$  is the distance from  $\bar{r}$  along the trajectory of particles.

We introduce here a new approach of exponential function approximation for a source term  $Q(\bar{r})$  in Eq. (1) instead of linear approximation which has already been implemented in the PALLAS code.

$$Q(R') = Q(\bar{r}_i) \cdot \exp\left[\frac{1}{R_0} \cdot \ln \frac{Q(\bar{r}_{i-1})}{Q(\bar{r}_i)} \cdot R'\right]. \quad (2)$$

Substituting Eq. (2) into Eq. (1), we obtain the following angular flux:

$$\begin{aligned} \Phi(\bar{r}_i, \bar{\Omega}_{pq}, E_j) &= \Phi(\bar{r}_{i-1}, \bar{\Omega}_{pq}, E_j) \exp[-\Sigma_t(\bar{r}_{i-1}, E_j) R_0] \\ &+ \frac{R_0 Q(\bar{r}_i)}{\ln \frac{Q(\bar{r}_{i-1})}{Q(\bar{r}_i)} - R_0 \Sigma_t} \\ &\times \left\{ \exp\left[\ln \frac{Q(\bar{r}_{i-1})}{Q(\bar{r}_i)} - \Sigma_t(\bar{r}_{i-1}, E_j) R_0\right] - 1 \right\} . \end{aligned} \quad (3)$$

We have adopted a compromise between linear and exponential representations with the criterion of selection based on the ratio of source intensities at each set of adjacent mesh points.

Figure 4.4.1 represents the numerical errors of PALLAS calculated fast neutrons due to spatial meshes, where LP denotes original PALLAS algorithm with the linear function representation and EP denotes modified PALLAS algorithm with the source term represented by a combination of linear and exponentail functions. In Fig. 4.4.2 are given numerical errors of ANISN calculations, where LM denotes standard ANISN algorithm based on the diamond difference scheme and EM means modified ANISN algorithm based on the exponential scheme proposed by Barbucci et al.<sup>2)</sup> In these figures, reference solutions are defined as solutions obtained by calculations using the finest mesh size.

By comparing the results of EP with those of other methods, it will be found that the use of the improved approximation gives reasonable solutions with small numerical errors irrespective of the spatial mesh size. This enables the PALLAS code to apply to deep penetration problems within a reasonable computer time by virtue of the use of large spatial mesh intervals. In addition to neutron calculations, gamma-ray penetration calculations were also investigated. As a result, the advantage of EP method was found to be greater in gamma-ray calculations than in neutron calculations.

#### References

- 1) Sasamoto N. and Takeuchi K.: "An Improvement of the PALLAS Discrete-Ordinates Transport Code", Nucl. Sci. Eng., 71, 330-342 (1979).
- 2) Barbucci P. and Di Pasquantonio F.: "Exponential Supplementary Equations for  $S_N$  Method: The One-Dimensional Case", Nucl. Sci. Eng., 63, 179-187 (1977).

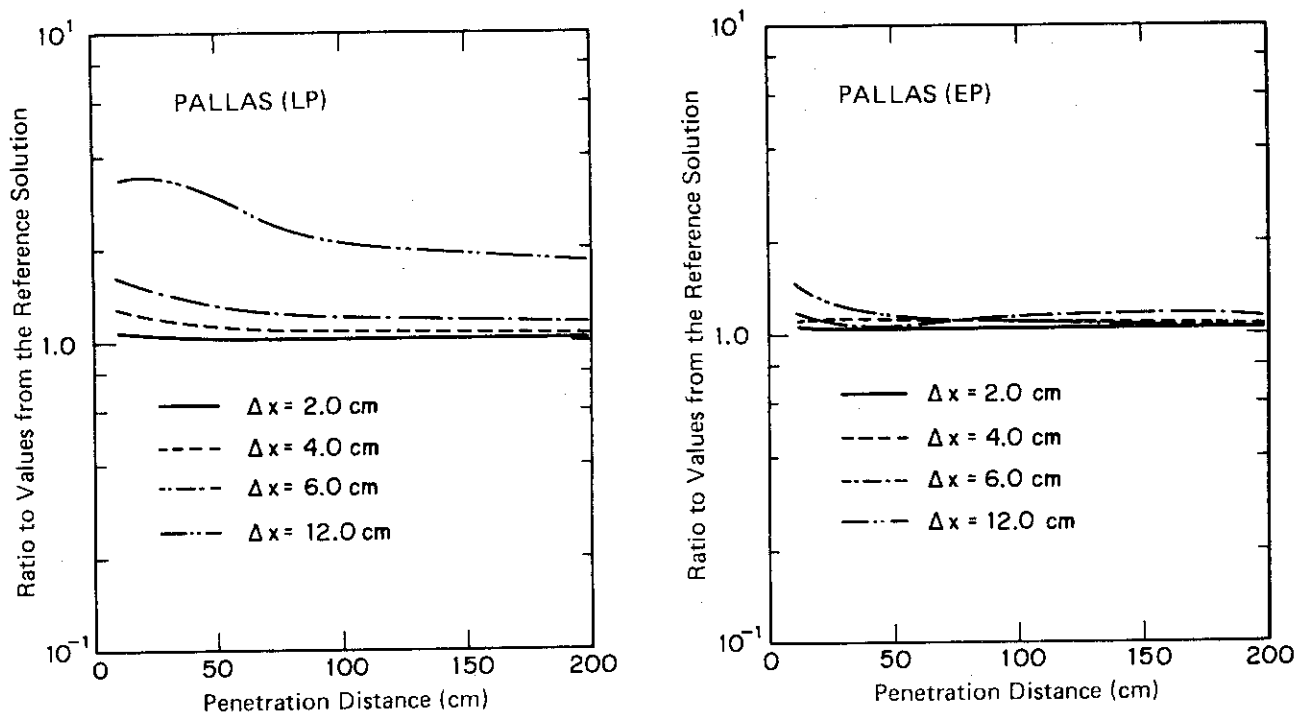


Fig. 4.4.1 Numerical errors of PALLAS due to mesh sizes for a problem of normally incident fission neutrons penetrating a 200-cm-thick water slab. LP and EP denote numerical schemes to represent the source distribution by linear function and combination of linear and exponential functions, respectively.

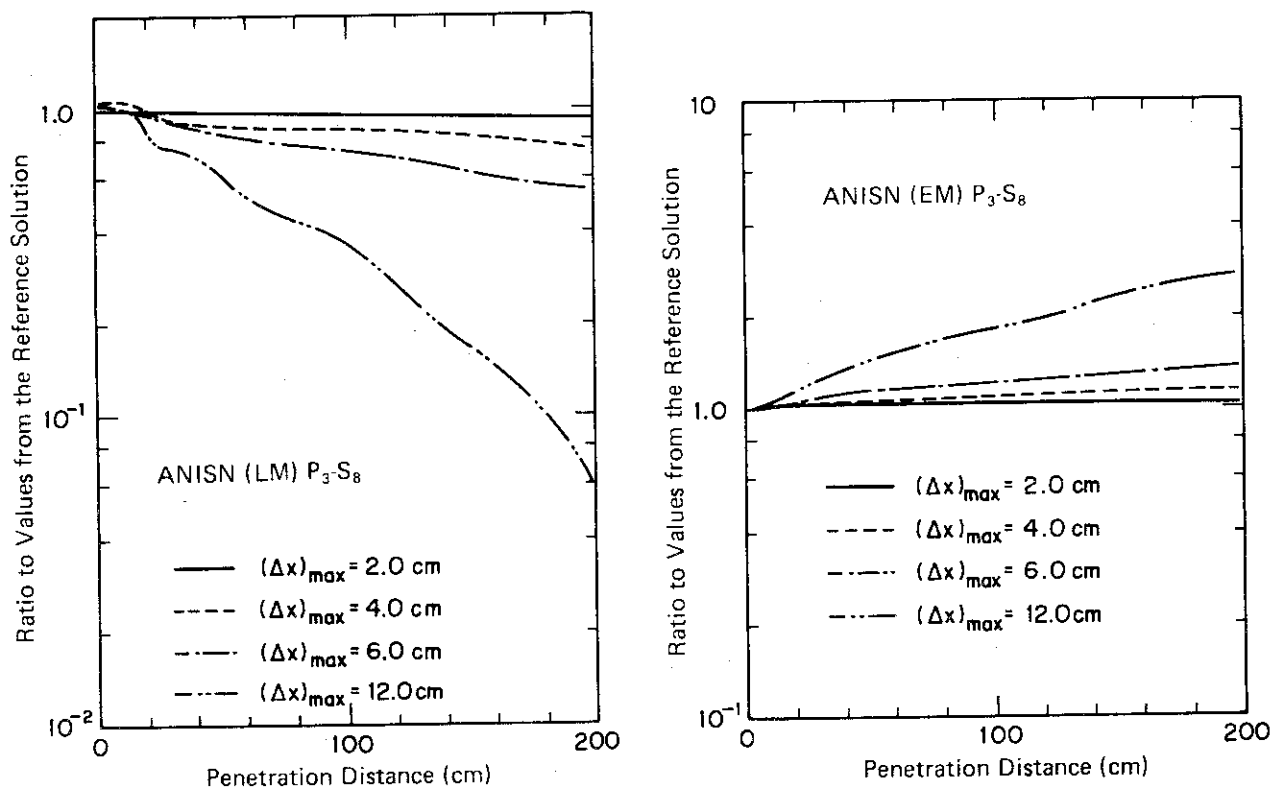


Fig. 4.4.2 Numerical errors of ANISN calculation due to mesh sizes for a problem of normally incident fission neutrons penetrating a 200-cm-thick water slab. LM and EM denote diamond scheme plus step and exponential scheme, respectively.

#### 4.5 PALLAS-2DCY-FC, a Calculational Method and Radiation Transport Code in Two-Dimensional (R,Z) Geometry

K. Takeuchi

A computer code, PALLAS-2DCY-FC<sup>1)</sup> has been written in FORTRAN-IV on FACOM 230/75 and CDC 6600, which is based on the method of direct integration of the steady state transport equation for neutrons and photons to describe the radiation transport in (r,z) two-dimensional geometry. As this method is fundamentally based on the discrete ordinates method, the Boltzmann transport equation is approximated by a set of equations describing relation between solution and variables on each mesh point of network in a phase space of energy, space and angles. In the network, an energy mesh approximation is used and the angular variables are meshed into a set of discrete directions with weights. The spatial variable is partitioned into (r,z) mesh points. Particle multiplication is not allowed in the current code. Only fixed source problem can be treated with the vacuum boundary condition at the outermost boundaries.

Inner iterations are not necessary for getting the solution. As a result, one can get always a solution without any fear of no convergence. Outer iterations are not allowed, so that its application is restricted to only radiation shielding problems. A Legendre expansion approximation is not used for treatment of anisotropy-calculation. Instead, the differential scattering cross section is used, which is formed by using the full data of Legendre coefficients for neutron from the ENDF/B file or by using the Klein-Nishina formula for photon. As a result, always positive reasonable scattering source is calculated, so that no negative fix-up technique is necessary. To mitigate ray-streaming effects an analytic first-collision source technique is utilized for various source configurations such as point, line, disk and cylindrical sources.

#### Reference

- 1) Takeuchi K.: Papers Ship Research Institute No. 57 (1979).



#### 4.6 A Computer Code FEM-3DP3 for Solving Three-Dimensional Radiation Transport $P_3$ Equation by Finite Element Method

T. Asaoka

For an efficient approach for dealing with irregular-shaped shielding problems, a computer code FEM-3DP3 has been developed for solving the multigroup  $P_3$  radiation transport equation in 3-dimensional (x,y,z) coordinate system by means of the finite element method.

By dividing the whole spatial system into prism- and/or box-shaped elements with the bases parallel to the (x,y) plane, the Galerkin type scheme of the finite element method results in the following system equation in the vector notation<sup>1,2)</sup>:

$$[H]\underline{\phi} = \underline{Q} . \quad (1)$$

Taking account of the tri-diagonal structure of the global matrix [H] of a large dimension, Eq. (1) is solved by applying the relaxation method successively to each (x,y) plane layer as follows:

$$\phi_{I,i}^{(t+1)} = \phi_{I,i}^{(t)} + \beta(\phi_{I,i}^{*(t+1)} - \phi_{I,i}^{(t)}), \quad (2)$$

where  $\phi_{I,i}^{(t)}$  is the flux moment at the i-th node of the I-th plane at the t-th iteration,  $\beta$  is the relaxation factor and  $\phi_{I,i}^{*(t+1)}$  is the solution of Eq. (1) obtained by using  $\underline{Q}$  at this iteration step.

For a verification of this FEM-3DP3 code, an external source problem was solved for the octantal system shown at the center of Fig. 4.6.1. The total source region has  $16 \times 16 \text{ cm}^2 \times 4 \text{ cm}$  height and it is surrounded completely by a black absorber of 4 cm thickness. The total system is divided into prism-shaped elements with a right triangle base of 4 cm side and with 4 cm height as shown in Fig. 4.6.1. The first-group fluxes obtained from 2-group FEM-3DP3 calculations are given in Fig. 4.6.1 for 2 points on the surface of the source region indicated in the figure, from which it is seen that the relaxation factor  $\beta = 0.4$  is most suited for achieving the flux convergence. Additional calculations were performed with the use of prism-shaped elements of 2 cm- and 1 cm-side, respectively. The results are summarized in Table 4.6.1, from which it is seen that the mesh width can be about the same as the mean-free-path

length and about twice as large as that required for finite difference calculations.

For a problem to deal with the total reactor system including the core, the  $k_{\text{eff}}$  calculation is required. The results obtained by the 2-group FEM-3DP3 calculation are summarized in Table 4.6.2 for a homogeneous medium with perfect reflective conditions for all boundaries. In this case, we can get the analytical solution which gives  $K_{\text{eff}} = 1.5434$ , first-group flux =  $8.378 \times 10^{-4}$ , second-group flux =  $7.093 \times 10^{-4}$ , while FEM-3DP3 has given the first-group flux =  $8.28 \sim 8.62 \times 10^{-4}$  and the second-group flux =  $6.94 \sim 7.29 \times 10^{-4}$ .

#### References

- 1) Asaoka T., Miyasaka S.: "A Numerical Solution of Three-Dimensional Radiation Transport  $P_L$  Equations by the Finite Element Method", in "Reactor Engineering Division Annual Report, 1977", JAERI-M 7844 (1978).
- 2) Asaoka T.: "A Computer Code for Solving Three-Dimensional Radiation Transport  $P_3$  Equations by the Finite Element Method", in "Reactor Engineering Division Annual Report, 1978", JAERI-M 8393 (1979).

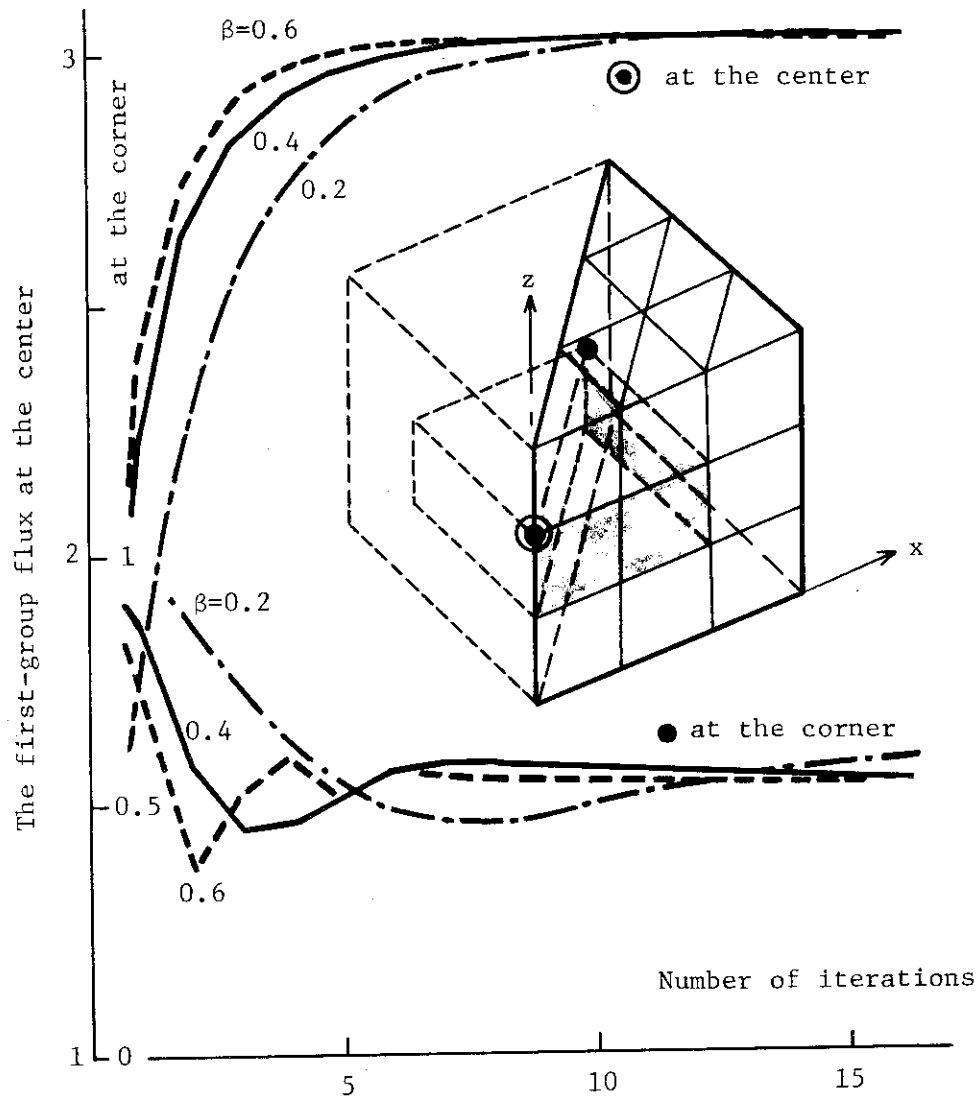


Fig. 4.6.1 The first-group fluxes at two points vs. number of iterations

Table 4.6.1 Calculation of an external source problem by FEM-3DP3

Mesh width	in cm	4	2	1
	in units of first-group mean-free-path	1.19	0.59	0.30
Total No. of elements		27	108	605
Total No. of node points		40	112	468
Required computer memory for data (Kwords)		4.1	14.0	60.8
Computation time per inner iteration (sec)		0.60	2.79	21.54
Average first-group flux over the source region		2.28	4.18	3.83

Table 4.6.2 Calculation of a  $k_{\text{eff}}$  calculation problem by FEM-3DP3

Outer iteration	Inner iteration error		Outer iteration error	$k_{\text{eff}}$
	1st-group	2nd-group		
1	$6.73 \times 10^{-2}$	$3.41 \times 10^{-2}$	—	1.5417
2	$7.87 \times 10^{-3}$	$2.92 \times 10^{-3}$	$1.07 \times 10^{-3}$	1.5434
3	$7.31 \times 10^{-4}$	$6.19 \times 10^{-4}$	$2.88 \times 10^{-5}$	1.5434

#### 4.7 Selection of Shielding Benchmark Problems for Evaluating the Data and Methods (II)

S. Tanaka and N. Sasamoto

Fourteen shielding benchmark problems are newly presented<sup>2)</sup>, in addition to the twenty-one problems already proposed<sup>1)</sup>, for evaluating the calculational algorithm and accuracy of computer codes based on discrete ordinates method and Monte Carlo method as well as for evaluation the nuclear data used in these codes.

In the present work, the selection was concentrated to shielding problems of the backscattering and streaming of neutrons and gamma rays in two- and three-dimensional configurations, which are essential for shielding design. Besides, this report also includes a few problems for calculation of the neutron deep penetrations in fast reactor shielding and for evaluation of the nuclear data used in 14 MeV neutron transport calculations.

The list of the benchmark problems is shown in Table 4.7.1.

#### References

- 1) Tanaka S., et al.: "Shielding Benchmark Problems", JAERI-M 7843 (1978).
- 2) Tanaka S., et al.: "Shielding Benchmark Problems (II)", JAERI-M 8686 (1980).

Table 4.7.1 The list of shielding benchmark problems (II)

1. Differential Number and Exposure Albedos for Semi-Infinite Media for Normally Incident Gamma Rays (Steyn)
2. Backscattered Gamma-ray Spectra from Various Materials (Hyodo)
3. Neutron Dose Albedo for Concrete and Iron for Incident Fission Neutrons (Meyer)
4. Differential Angular Thermal Neutron Albedos for Steel Reinforced Concrete (ORNL-TSF)
5. Fast Neutron Spectra of d-D and d-T Neutrons Backscattered by Iron Slabs (Durling)
6. Albedo of Neutrons for Concrete-Iron Layer and Neutron Streaming through Cylindrical Bent Duct of Concrete-Iron (YAYOI)
7. Neutron Streaming through Two-Legged Concrete Duct of Rectangular Geometry (Song)
8. Neutron Streaming along the Center Lines of One-, Two-, and Three-Legged Square Concrete Open Ducts (TSR-II)
9. Neutron and Gamma-ray Streaming through Annular Bent Ducts (JRR-4)
10. Neutron Streaming in Straight Air Slots through Graphite Shields (JRR-4)
11. Neutron Streaming through Cylindrical Ducts with Two Bends in Water (ETNA)
12. Attenuation of Neutrons in a Shield of Na and Stainless Steel Simulated the FFTF Radial Shield (CSEWG)
13. Leakage Neutron Spectra from Sphere of Some Materials Bombarded with 14 MeV Neutrons (LLL)
14. Energy Spectra and Dose Albedo of Photons Backscattered by Al Slabs (Vogt)

#### 4.8 Measurement and Calculation of Radiation Streaming through Annular Ducts<sup>1)</sup>

T. Miura\*, K. Takeuchi\* and T. Fuse\*

Experiments on the duct streaming were carried out in the pool of JRR-4, a swimming pool type research reactor installed at Japan Atomic Energy Research Institute. The behavior of the streaming radiation was investigated for two types of duct, the one is a straight annular duct in an unsymmetrical configuration and the other is an annular duct with one bend. The experiment for the former duct is denoted as experiment 1 and the one for the latter duct is denoted as experiment 2. In the both experiments, air or water was chosen as the material inside the inner pipe. Experimental configurations are shown in Figs. 4.8.1 and 4.8.2 together with measuring positions. There were four experimental configurations, which were denoted as i-j, where i corresponds to experimental number and j corresponds to the material inside the inner steel pipe, that is j=1 indicates air and j=2 indicates water. Reaction rate and dose rate distributions in and around the ducts were measured by using activation detectors and thermoluminescent dosimeters (TLDs). As the activation reactions,  $^{197}\text{Au}(n,\gamma)^{198}\text{Au}$ ,  $^{115}\text{In}(n,n')^{115\text{m}}\text{In}$ ,  $^{58}\text{Ni}(n,p)^{58}\text{Co}$ ,  $^{64}\text{Zn}(n,p)^{64}\text{Cu}$  and  $^{27}\text{Al}(n,\alpha)^{24}\text{Na}$  were used. Two or three pairs of  $^6\text{LiF}$  and  $^7\text{LiF}$  rod of Hawshaw Chemical Co. were used as the TLDs for each measuring position. The experimental errors in the measured values were less than 29% for reaction rate and less than 19% for dose rate. Thermal and epithermal neutron fluxes were also obtained from the measured reaction rates under the assumption of 1/E spectrum in the intermediate energy region. Also, isotropic or beam incidence were assumed in the calculation of the self-shielding factor of gold foil, depending on the measuring position.

---

\* Ship Research Institute

Some of the experimental results obtained in the experiment 1 are shown in Figs. 4.8.3 and 4.8.4 comparing with calculation. In the experiment 1, it was found that the fast neutron flux distribution in the annular gap was mainly determined by the component penetrating through the water shield from the reactor core. On the other hand, the thermal and the epithermal neutron flux distributions were mainly determined by the streaming component. The calculation was made with the aid of PALLAS-2D two-dimensional transport code, in which two steps of calculation were taken. First, the angular flux distribution was calculated in the water including the reactor core. Secondly, the neutron flux distribution was calculated in a symmetrical duct configuration. For the latter calculation, the boundary condition was decided by using the result of the former calculation. Although there is a discrepancy on attenuation rate between the calculation and the measurement as shown in Fig. 4.8.3, agreement is quite fair for the fast neutron flux distribution along the duct axis. In the case of lower energy neutron flux distribution along the duct axis, the calculation overestimates within a factor of 3, though fairly good agreement is obtained with respect to the attenuation rate. It is considered that these discrepancies are mainly arising from the insufficient boundary condition taken in the second step's calculation. For the experiment 2, some of the results are shown in Figs. 4.8.5 ~ 4.8.7. Fast neutron flux distributions are shown in Fig. 4.8.5 in terms of reaction rate for three kinds of threshold detectors. The threshold energies are  $\sim 1$  MeV for  $^{115}\text{In}(n,n')^{115\text{m}}\text{In}$ ,  $\sim 3$  MeV for  $^{58}\text{Ni}(n,p)^{58}\text{Co}$  and  $\sim 8$  MeV for  $^{27}\text{Al}(n,\alpha)^{24}\text{Na}$ . In the MeV energy region, the neutron flux of higher energy attenuates more slowly than those of lower energy in the first leg. On the contrary, the neutron flux of lower energy attenuates more slowly than those of higher energy



in the second leg. From the experimental results, it can be said that the bent part has appreciable shielding effect for fast neutron and gamma-ray, though this effect is small for the neutrons in the thermal and epithermal energy region. The results of experiment 2 was selected as the one of the benchmark problems<sup>2)</sup> by the Research Committee on Shielding Design in the Atomic Energy Society of Japan.

#### References

- 1) Miura, T., Takeuchi, K. and Fuse, T.: "Measurement and Calculation of Radiation Streaming through Annular Ducts", Rep. Ship Res. Inst. 16 [6] 17 (1979)
- 2) Tanaka. S., et al.: "Shielding Benchmark Problems (II)", JAERI-M 8686, (1980)

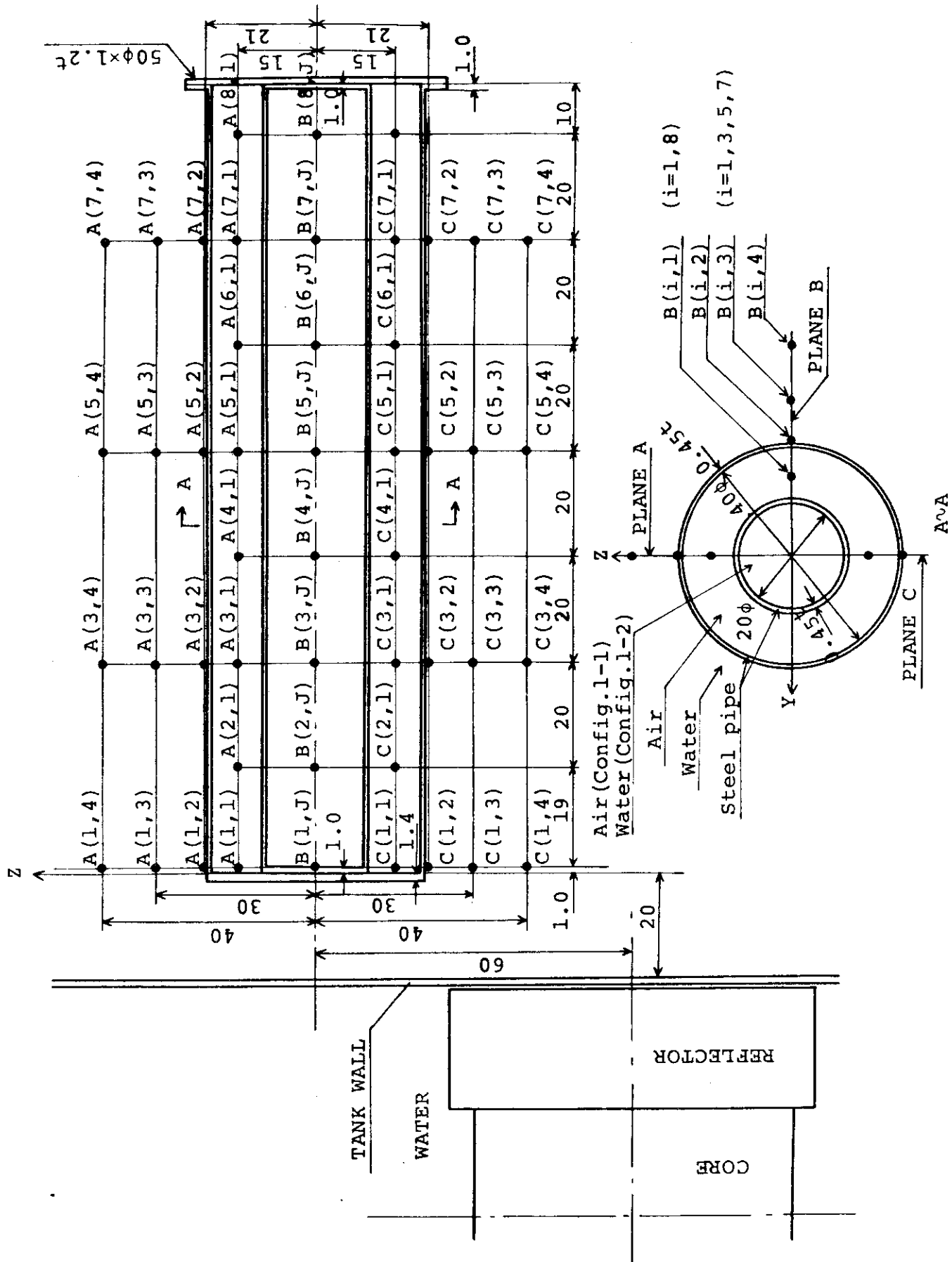


Fig. 4.8.1 Configuration and measuring positions of experiment 1

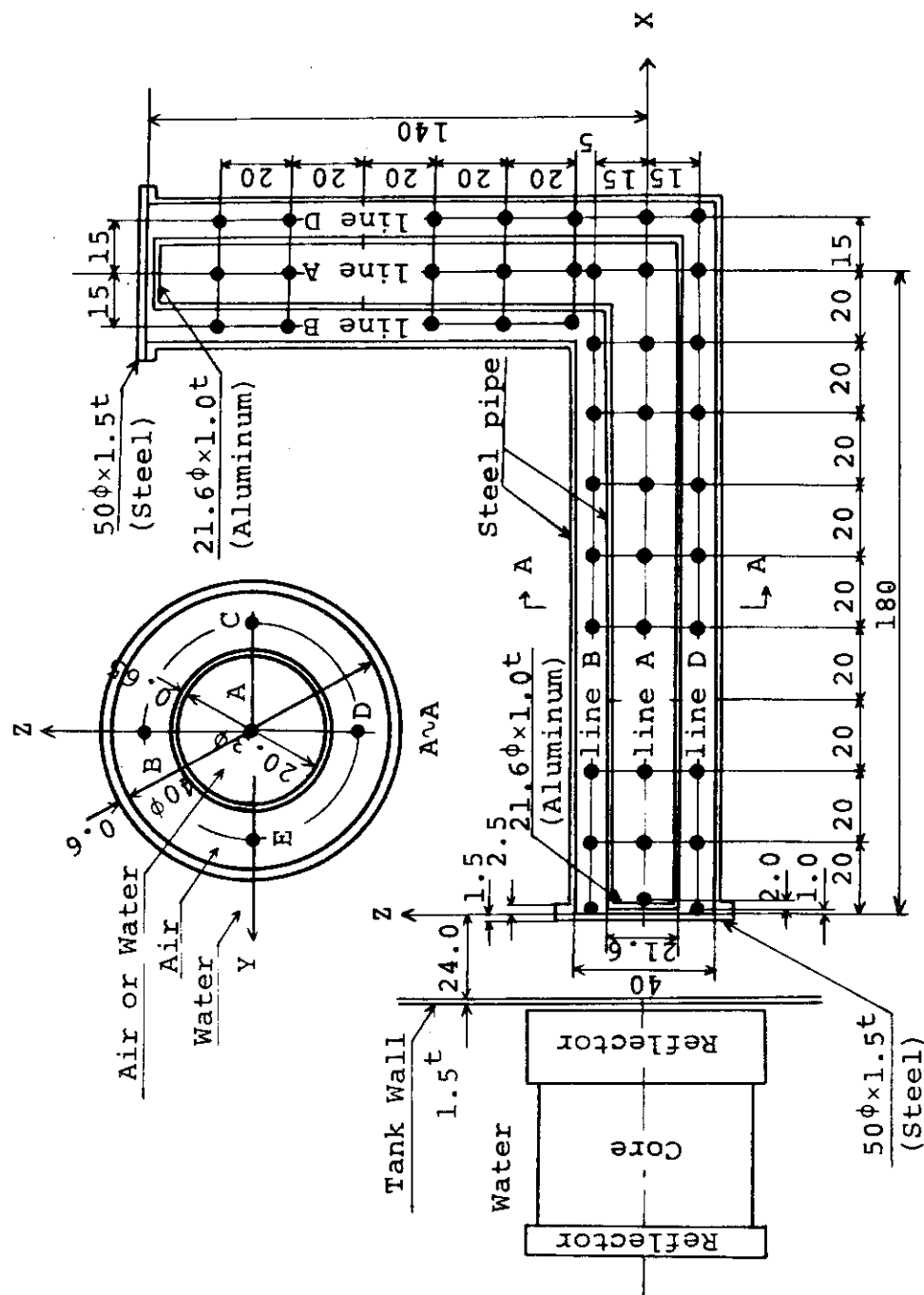


Fig. 4.8.2 Configuration and measuring positions of experiment 2

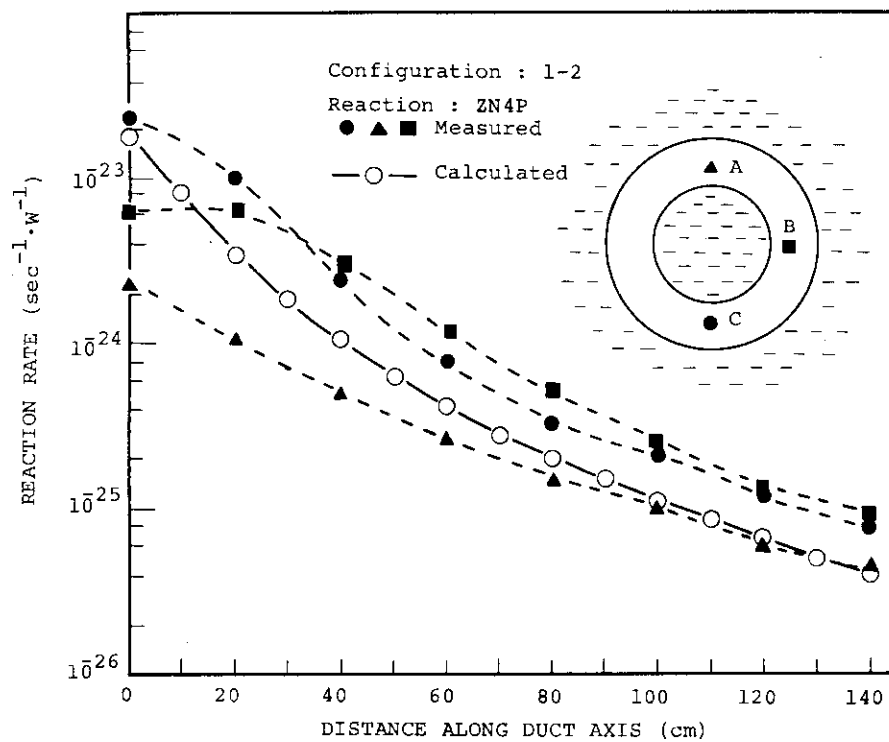


Fig. 4.8.3 Comparison of measured and calculated axial distributions of  $^{64}\text{Zn}(n,p)^{64}\text{Cu}$  reaction rate

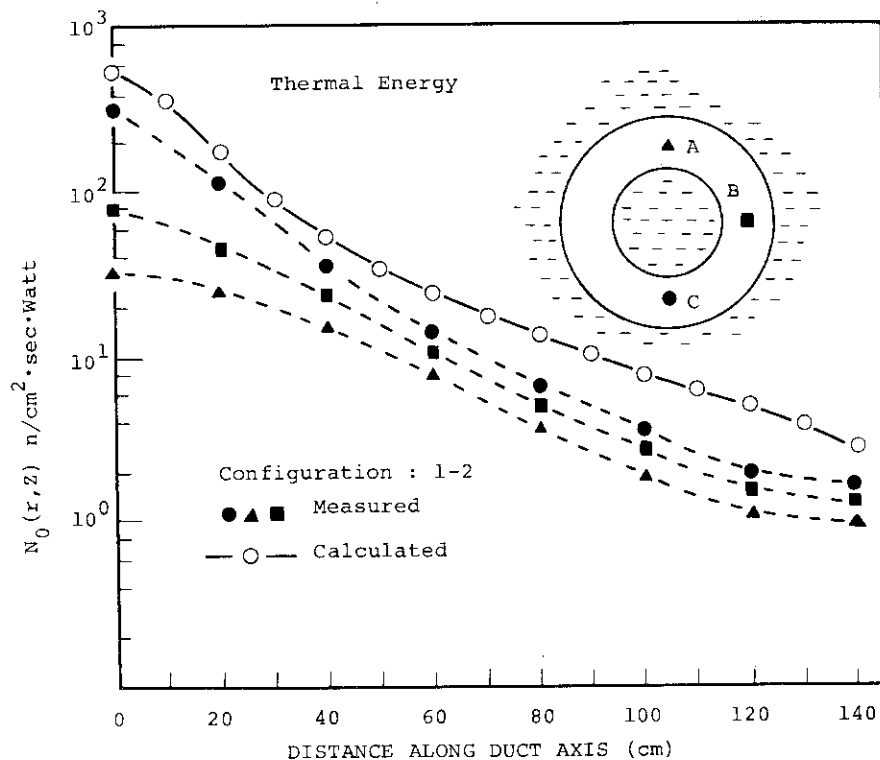


Fig. 4.8.4 Comparison of measured and calculated axial distributions of thermal neutron flux

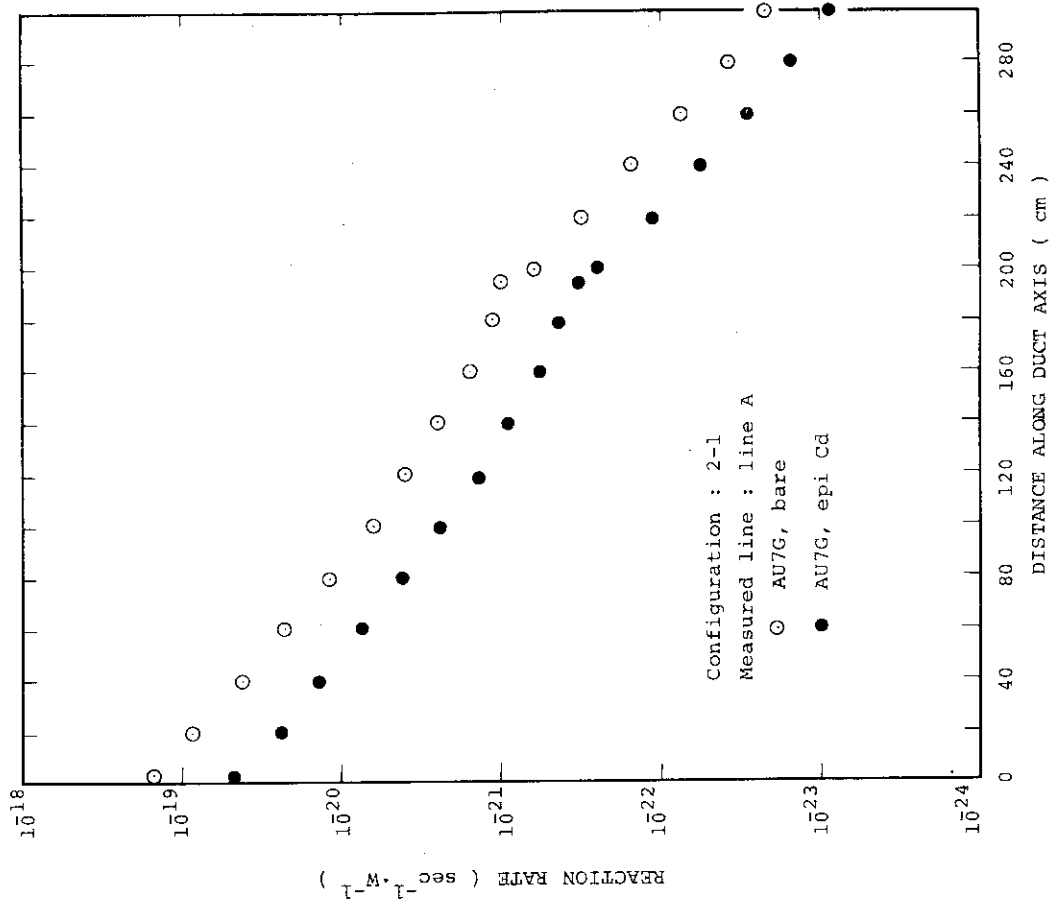


Fig. 4.8.5 Axial distributions of  $^{115}\text{In}$  ( $n,n'$ )  $^{115m}\text{In}$ ,  $^{58}\text{Ni}$  ( $n,p$ )  $^{58}\text{Co}$  and  $^{27}\text{Al}$  ( $n,\alpha$ )  $^{24}\text{Na}$  reaction rate measured in configuration 2-1

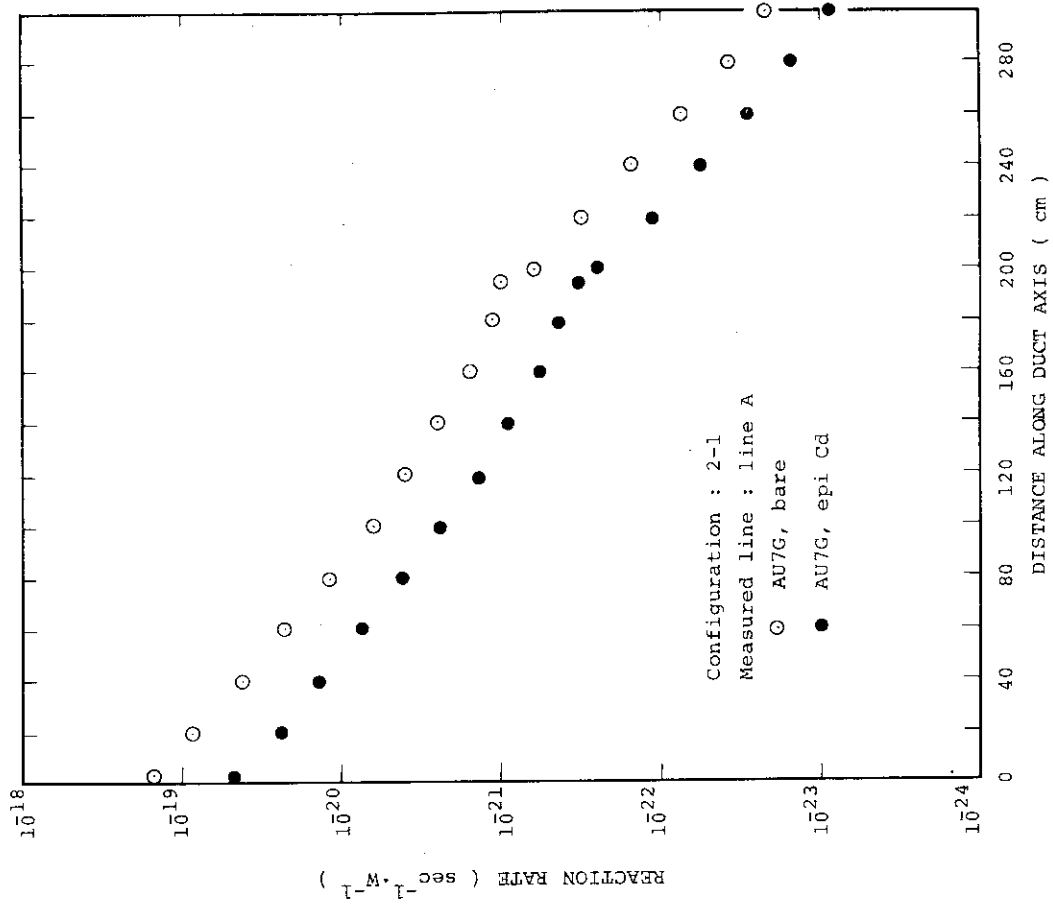


Fig. 4.8.6 Axial distributions of bare and Cd-covered  $^{197}\text{Au}$  ( $n,\gamma$ )  $^{198}\text{Au}$  reaction rate measured in configuration 2-1

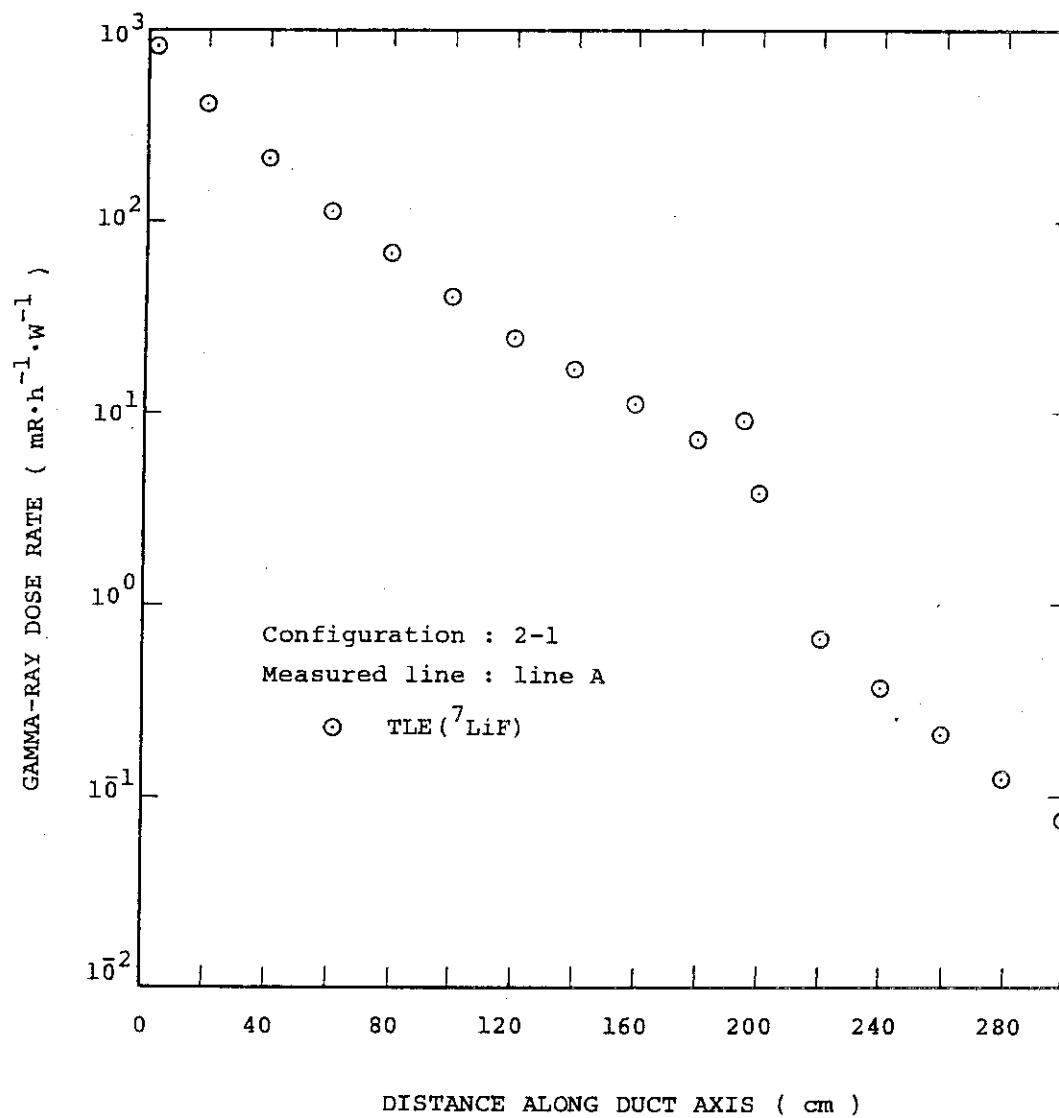


Fig. 4.8.7 Axial distributions of gamma-ray dose rate measured in configuration 2-1

4.9 Fast Neutron Transport through Laminated Iron Water Shield<sup>1)</sup>

T. Miura\*, K. Takeuchi\* and N. Yamano\*\*

In order to present a neutron transport benchmark experiment on an iron-water configuration and to access the one-dimensional discrete ordinates transport codes ANISN-JR<sup>(2)</sup> and PALLAS<sup>(3)</sup>, reaction rates were measured in a laminated iron-water shield by threshold detectors. Experiment was made in the pool of JRR-4, a swimming pool type research reactor installed at Japan Atomic Energy Research Institute. Experimental configuration and measuring positions are shown in Fig.4.9.1. Eight kinds of threshold reactions were used. They are  $^{115}\text{In}(n,n')$ ,  $^{115\text{m}}\text{In}$ ,  $^{58}\text{Ni}(n,p)$ ,  $^{58}\text{Co}$ ,  $^{64}\text{Zn}(n,p)$ ,  $^{64}\text{Cu}$ ,  $^{54}\text{Fe}(n,p)$ ,  $^{54}\text{Mn}$ ,  $^{27}\text{Al}(n,p)$ ,  $^{27}\text{Mg}$ ,  $^{56}\text{Fe}(n,p)$ ,  $^{56}\text{Mn}$ ,  $^{24}\text{Mg}(n,p)$ ,  $^{24}\text{Na}$  and  $^{27}\text{Al}(n,\alpha)$ ,  $^{24}\text{Na}$ . Reaction rate measurement was made within an accuracy of 25%.

Fast neutron spectra were obtained from the measured reaction rates by means of SAND-II code<sup>(4)</sup>. Iterative process in the SAND-II calculation was terminated when the iterative reaction rate satisfied the relation :

$$\sqrt{\sum_{i=1}^n \{(A_i - A_i^{[k]})/A_i\}^2} \leq \sqrt{\sum_{i=1}^n (\epsilon_i/A_i)^2},$$

where  $A_i$  : Measured reaction rate for i-th reaction  
 $A_i^{[k]}$  : k-th iterative reaction rate for i-th reaction  
 $\epsilon_i$  : Experimental error in  $A_i$   
 $n$  : Number of reactions used in measurement.

The reliability of the unfolded spectra was investigated by checking following items one by one: (1) The energy range in which the meaningful unfolding spectrum is obtained. (2) The effects of the difference of the cross section values between two available activation cross section sets and of the errors in the

\* Ship Research Institute

\*\* Sumitomo Atomic Energy Industries, Ltd.

measured reaction rates on the unfolded spectra. (3) Whether the unfolded spectra are reliable enough to access small differences found between calculated spectra by PALLAS and ANISN-JR for some measuring positions. (4) Comparison of the measured reaction rates and those obtained from the unfolded spectra. Through these error analysis, it was found that the measured spectra were obtained satisfactorily to access transport codes in the energy range of  $1 \sim 10.5$  MeV.

One-dimensional calculations were carried out with ANISN-JR and PALLAS discrete ordinates transport codes in a spherical geometry using the ENDF/B-IV file and the parameters of  $S_{16}$  and  $P_5$  for the former and an angular quadrature set of Gaussian 16 points and  $P_7$  to  $P_{12}$  for the latter.

A comparison of the measured and the calculated reaction rates is given in Table 4.9.1 in the form of  $\{((R.R.)_{\text{calculated}} - (R.R.)_{\text{measured}}) / (R.R.)_{\text{measured}}\} \times 100$ , where R.R. means reaction rate. Almost all calculated reaction rate agree with those of measured within the experimental error of 25%. In general, a very good agreement is obtained between the measured and the calculated spectra as shown in Fig.4.9.2. From these results, it was concluded that the selection of the parameters used in the calculations was adequate for this deep penetration problem.

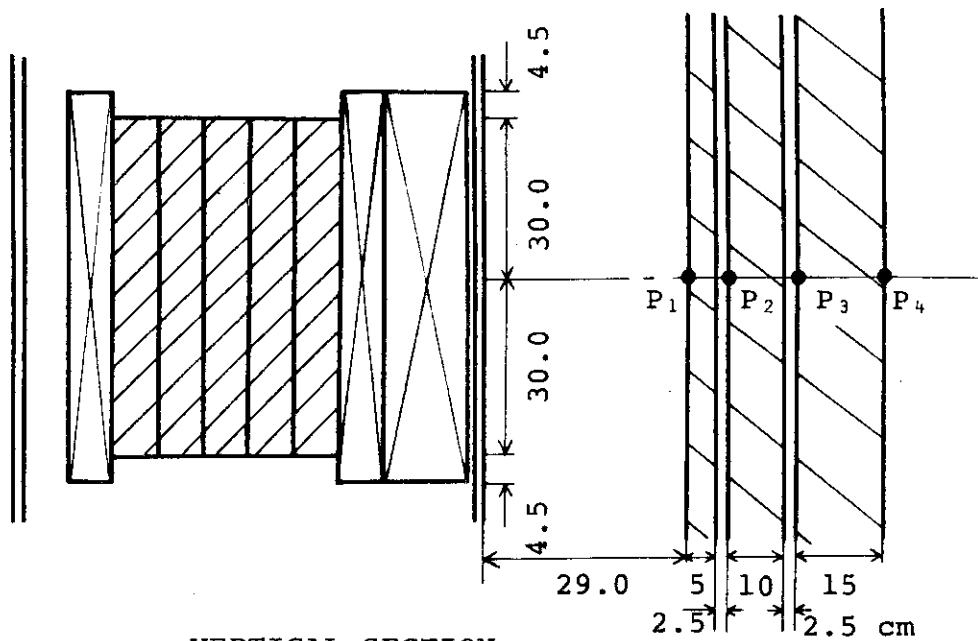
#### References

- 1) Miura, T. Takeuchi, K and Yamano, N.: "Fast Neutron Transport through Laminated Iron-Water Shield", J. Nucl. Sci. Technol., 16 [8] 563 (1979)
- 2) Koyama, K., et al.: "ANISN-JR, A One-dimensional Discrete Ordinates Code for Neutron and Gamma-ray Transport Calculations", JAERI-M 6954 (1977)
- 3) Takeuchi, K : "PALLAS-PL, SP A One Dimensional Transport Code". Pap. Ship Res. Inst. No.42 (1973)
- 4) McElroy, W. N.: "A Computer-Automated Iterative Method for Neutron Flux Spectra Determination by Foil Activation", AFWL-TR-67-41, (1967)

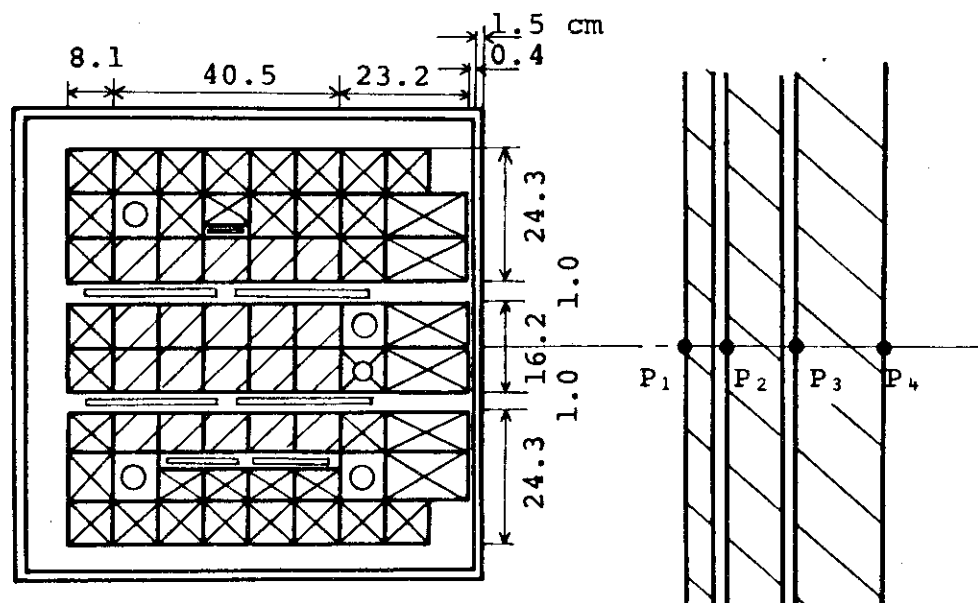


Table 4.9.1 Comparison of measured and calculated reaction rates

Reaction	$\frac{(\text{R.R.})_{\text{calculated}} - (\text{R.R.})_{\text{measured}}}{(\text{R.R.})_{\text{measured}}} \times 100$							
	$P_1$		$P_2$		$P_3$		$P_4$	
	PALLAS	ANISN	PALLAS	ANISN	PALLAS	ANISN	PALLAS	ANISN
$^{115}\text{In}(n,n')$	5	-8	11	-6	-8	-24	-5	-8
$^{58}\text{Ni}(n,p)$	17	5	26	10	-3	-18	-13	-26
$^{64}\text{Zn}(n,p)$	-2	-12	10	-5	11	-6	-14	-3
$^{54}\text{Fe}(n,p)$	3	-10	6	-10	-	-	-	-
$^{27}\text{Al}(n,p)$	<1	-10	-14	-22	-13	-20	-11	-15
$^{56}\text{Fe}(n,p)$	<1	-14	2	-9	-18	-22	-3	-22
$^{24}\text{Mg}(n,p)$	19	5	31	20	12	8	9	12
$^{27}\text{Al}(n,\alpha)$	8	-5	15	6	15	12	-5	1



VERTICAL SECTION



HORIZONTAL SECTION

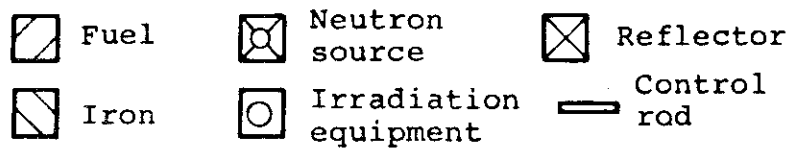


Fig. 4.9.1 Experimental configuration and measuring positions,  
 $P_1 \sim P_4$

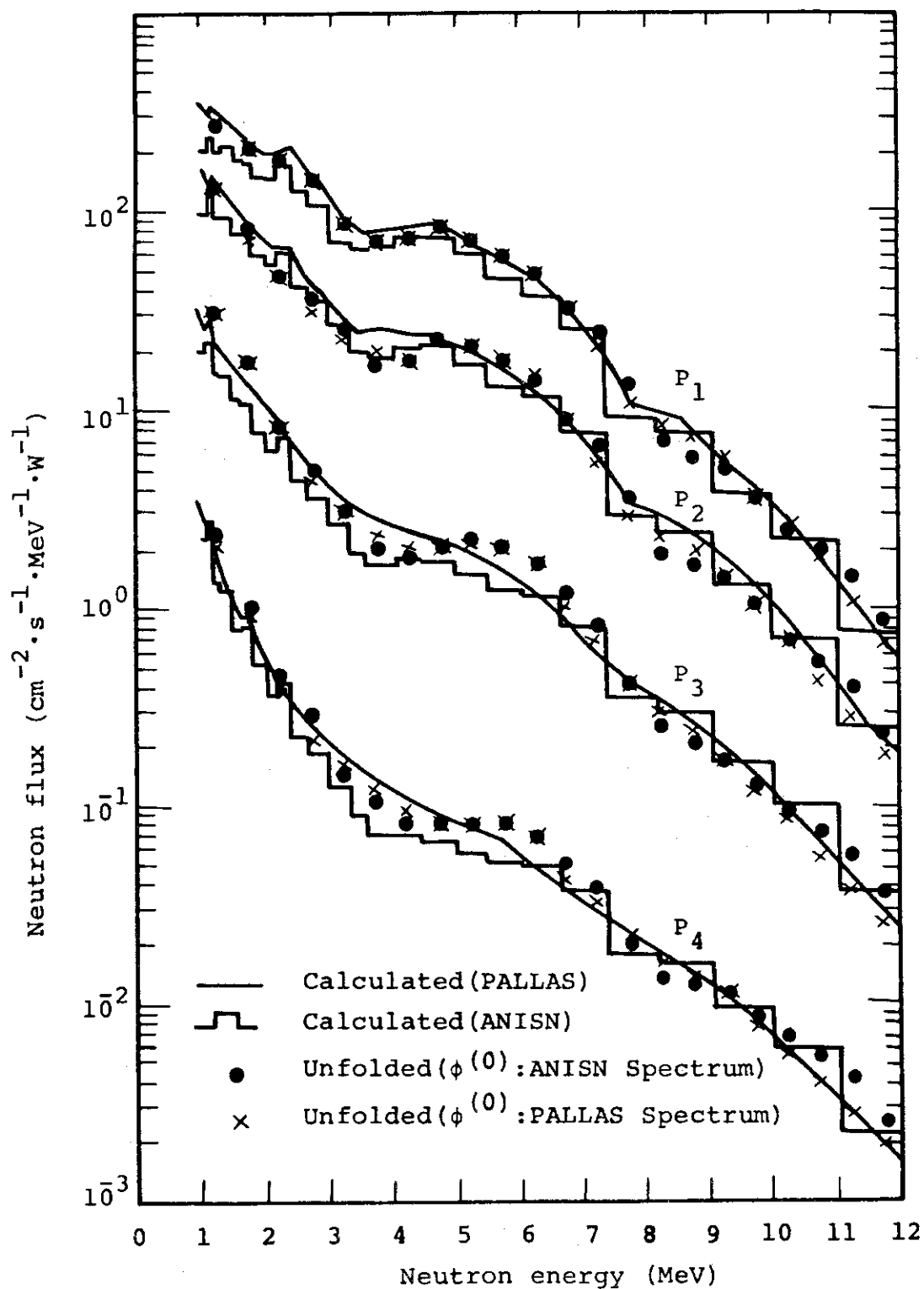


Fig. 4.9.2 Comparison of measured and calculated spectra in a laminated iron-water shield

## 5. Reactor and Nuclear Instrumentation

### 5.1 Development of High-Temperature Neutron Detectors

N. Wakayama, H. Yamagishi, H. Itoh, T. Tomoda\* and S. Fukakusa\*

High-performance and high-temperature fission counter-chambers which can be used in reactor vessel of VHTRs, HTGRs and large scale LMFBRs were developed, and tests of operating characteristics in high temperature and high gamma-ray environments were carried out to examine effects of neutron irradiation at high temperature<sup>1~6)</sup>. As the next item in the developmental works, a long-term in-reactor operating test at high temperature was started in the research reactor JRR-4.

Two fission counter-chambers, model FX-2A and FX-3, set up in high-temperature electric furnaces, were installed in the thermal column of the JRR-4 in March 1978. After various kinds of fundamental operating tests at the setting position in the JRR-4, the long-term in-reactor and real-time operating test was started: the chambers are in operation at 600 °C since December 1978.

No trouble have been observed on these chambers during test up to now. Figure 5.1.1 shows integral bias curves for the FX-2A chamber measured in an early stage and in March 1980, as an example of the test results obtained until now.

#### References

- 1) Wakayama N., Gotoh H., Tomoda T.: "Reactor Eng. Div. Annual Report (Apr. 1973 - Mar. 1974)", JAERI-M 5955, 131 (1975).
- 2) Wakayama N., Yamagishi H., Tomoda T.: "Reactor Eng. Div. Annual Report (Apr. 1975 - Mar. 1976)", JAERI-M 6710, 119 (1976).
- 3) Wakayama N., Yamagishi H., Tomoda T.: "Reactor Eng. Div. Annual Report (Apr. 1976 - Mar. 1977)", JAERI-M 7291, 132 (1977).
- 4) Wakayama N., Yamagishi H., Itoh H., Tomoda T.: "Reactor Eng. Div. Annual Report (Apr. 1977 - Mar. 1978)", JAERI-M 6844, 133 (1978).
- 5) Wakayama N., Yamagishi H., Tomoda T., Kawashima K.: "Development of Fission Chambers for High-Temperature Reactors", Symposium Proceedings on Nuclear Power Plant Control and Instrumentation, Vol.II, IAEA-SM-

---

\* Mitsubishi Electric Corporation

226/32, 243 (1978) IAEA

- 6) Wakayama N., Yamagishi H., Itoh H., Tomoda T., Fukakusa S.: "Reactor Eng. Div. Annual Report (Apr. 1978 - Mar. 1979)", JAERI-M 8393, 77 (1979).

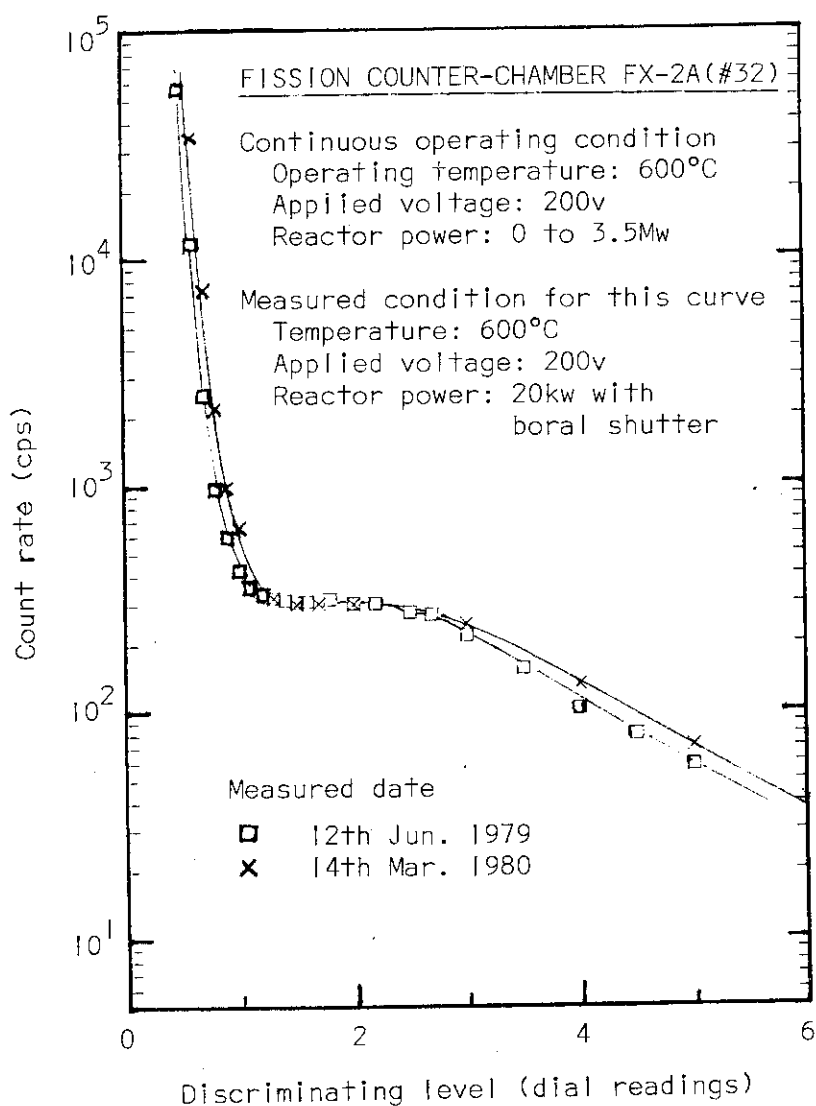


Fig. 5.1.1 A result of the long term, high temperature in-reactor operating test of fission counter-chambers developed.

## 5.2 Development of High-Temperature Thermocouples for VHTR

K. Ara, N. Wakayama and M. Yamada

Measurement of helium-gas temperature at the outlet of fuel region in the multi-purpose high-temperature gas-cooled reactor (VHTR) is very important for reactor operation, holding the key to the success of obtaining the outlet-gas temperature of 1000 °C in safe. This brings need of high-temperature sensor which can stand the maximum temperature of 1350 °C for a long term in the reactor core. However, there seems to be nothing of thermocouples which can meet this requirement. Development of high-temperature thermocouples for the multi-purpose VHTR have been, therefore, started; and the CA composite-type stranded W-Re thermocouple and the Pt-Mo thermocouple are now under development.<sup>1,2)</sup>

In the development of the former thermocouple, the efforts have been concentrated upon establishing the technique and the know-how for fabrication the reliable hot-junction, the reliable compensating-junction and the reliable double protection-tube, involving application techniques of the electron-beam welding and the micro-brazing. The trially produced thermocouples are now under in-pile and out-pile long-term high-temperature tests.

As for the latter thermocouple, the stability of thermocouple elements at a high-temperature and high-vacuum environment has been investigated after the previous study<sup>2)</sup>. The Pt-0.1%Mo element and the Pt-5%Mo one were exposed to the temperature of about 1200 °C in the vacuum of about  $10^{-6}$  Torr for 3000 hours, and the changes of electromotive force, mechanical strengths and metallographical structures were measured and observed. The results are shown in Photo. 5.2.1 and Figs. 5.2.1-3. Even though the remarkable grain growth and change of mechanical strengths, in both the elements, were observed in early 100 hours, these degradations did not develop largely thereafter. The electromotive force, on the other hand, varied very little; i.e., +0.05 % after the exposure of 100 hours, +0.1 % after 1800 hours and +0.18 % even after 3000 hours.

From these results, one can say that the Pt-Mo alloy elements must be very promising as the thermocouple for the multi-purpose VHTR, if oxidizing atmosphere is completely isolated from the vicinity of the elements and clean atmosphere can be kept during service.

## References

- 1) Ara K., Wakayama N.: JAERI-M 7844, pp.137-140 (1978).
- 2) Ara K., Wakayama N., Yamada M.: JAERI-M 8393, pp.88-91 (1979).

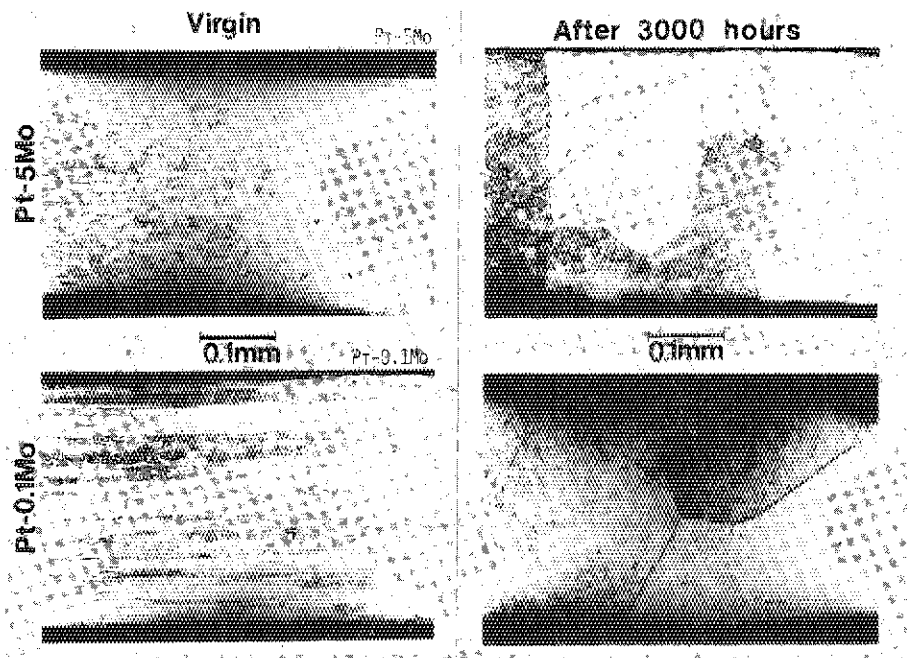


Photo. 5.2.1 Metallographical change of Pt-Mo alloy TC elements at Ca.  $1200^{\circ}\text{C}$ - $10^{-6}$  Torr

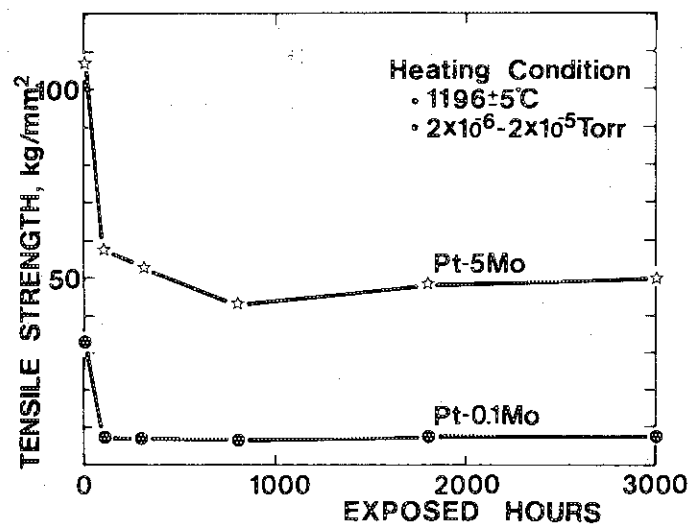


Fig. 5.2.1 Tensile strength of Pt-Mo alloy TC elements, at  $20^{\circ}\text{C}$

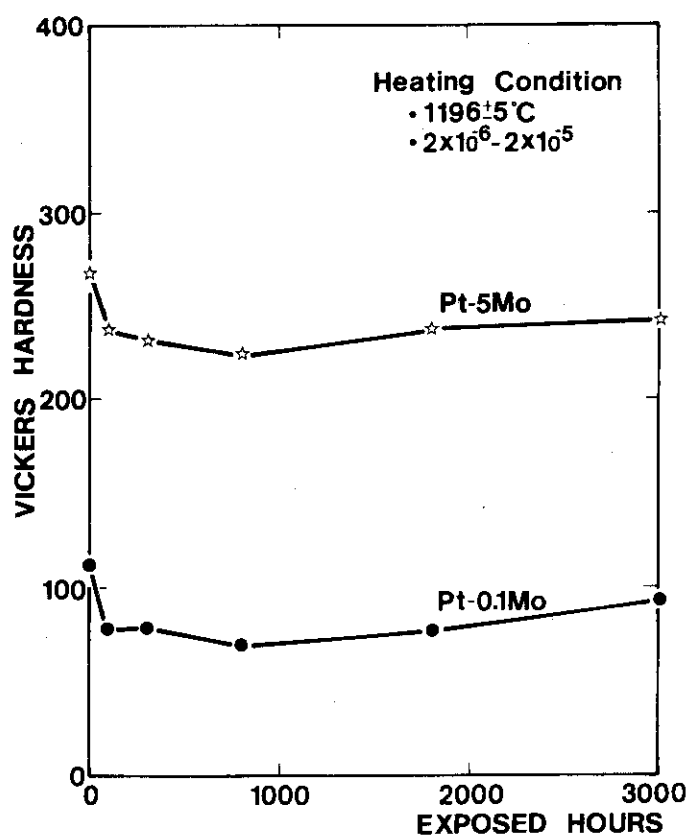


Fig. 5.2.2 Hardness of Pt-Mo alloy TC elements, at  $20^\circ\text{C}$

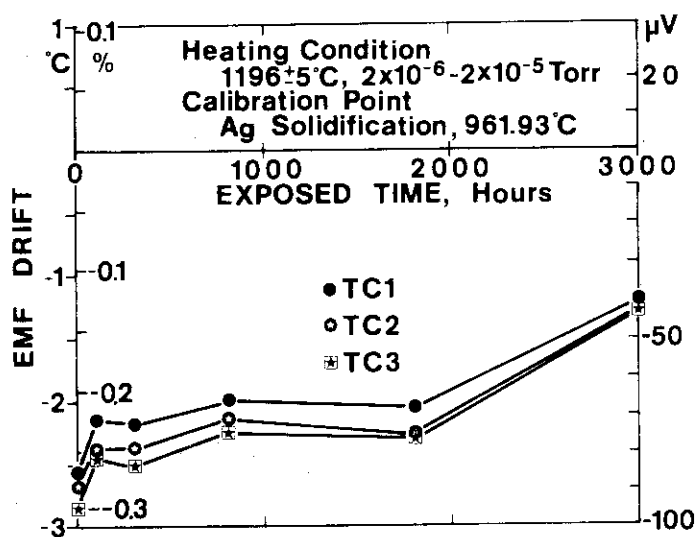


Fig. 5.2.3 EMF drift of Pt-5Mo/Pt-0.1Mo TC



## 5.3 Preliminary Study of Johnson Noise Thermometer for VHTR Application

T. Kakuta

A new temperature measuring method of Johnson noise thermometry (JNT) is based on Nyquist formula which characterizes the behavior of free electrons in thermal equilibrium with a resistor. (1) - (4)

Generally, the thermal noise appearing in a resistor of  $R$  ohm is given by

$$\overline{e_n^2} = 4 k T R \Delta f, \dots\dots\dots(1)$$

or

$$\overline{i_n^2} = 4 k T \frac{1}{R} \Delta f, \dots\dots\dots(2)$$

where  $\overline{e_n^2}$  is the mean squared thermal noise voltage of the unloaded resistor,  $\overline{i_n^2}$  the mean squared thermal noise current of the shorted resistor,  $k$  the Boltzmann's constant,  $\Delta f$  the frequency bandwidth and  $T$  the absolute temperature, respectively.

Since the product of the thermal noise signals; i.e.,  $\overline{e_n^2} \cdot \overline{i_n^2}$ , becomes independent of the sensing resistor, this can lead to an accurate temperature measuring method which is not affected by resistor composition, its thermal and mechanical history and transmutation of resistor material due to neutron irradiation. Therefore, development of JNT was started for applying to in-core calibration of high-temperature thermocouples in VHTR, and a preliminary study was carried out.

Figure 5.3.1 shows the sensing resistor of JNT. The sensing resistor is a coil of 0.1mm-dia stainless steel wire wound on 3.8mm-dia alumina ceramic insulator bobbin. The ohmic value of sensing resistor is 200 ohms at 20°C. This sensing resistor coil is sheathed in a 6.4mm-dia stainless steel tube of 500mm-length with ceramic insulator.

The arrangement of measuring circuit for obtaining the thermal noise voltage-signal is shown in Fig. 5.3.2. The noise signal from the sensing resistor is amplified in the low noise voltage sensitive amplifier, filtered through the band pass filter (establishing  $\Delta f$ ) and converted to the equivalent d.c. signal by the true RMS meter.

An example of experimental results is shown in Fig. 5.3.3. The experimental data agreed very well with the theoretically calculated values, verifying the feasibility of measuring absolute temperature by JNT.

# References

- 1) H.Nyquist, Phys. Rev. 32, 110 (1928).
- 2) J.B.Garrison and A.W. Lawson, Rev. sci. Instrum. 20 785 (1949).
- 3) H.G.Brixy, Nuclear Instruments and Methods 97 (1971) P75-80.
- 4) C.J.Borkowski and T.V.Blalock, Rev. Sci. Instrum., Vol.45, No.2 February, 1974. P151-162.

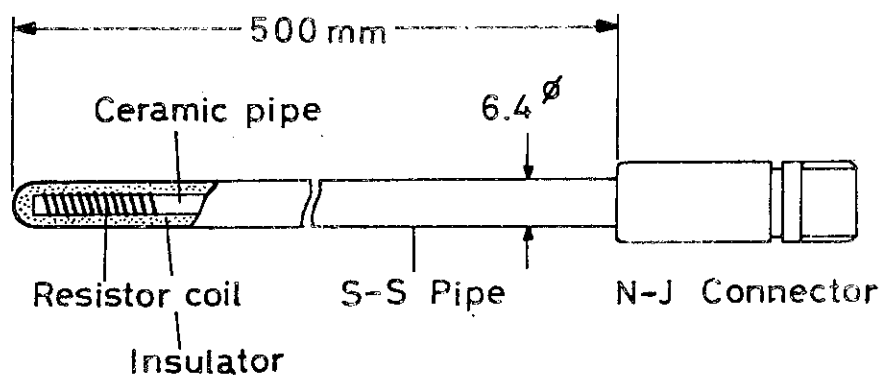


Fig. 5.3.1 Sensing Resistor of Johnson Noise Thermometer

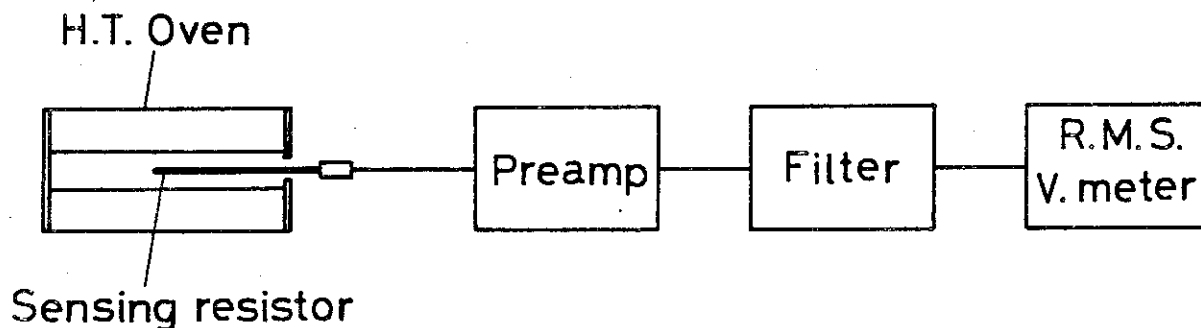


Fig. 5.3.2 Arrangement of Measuring Circuit

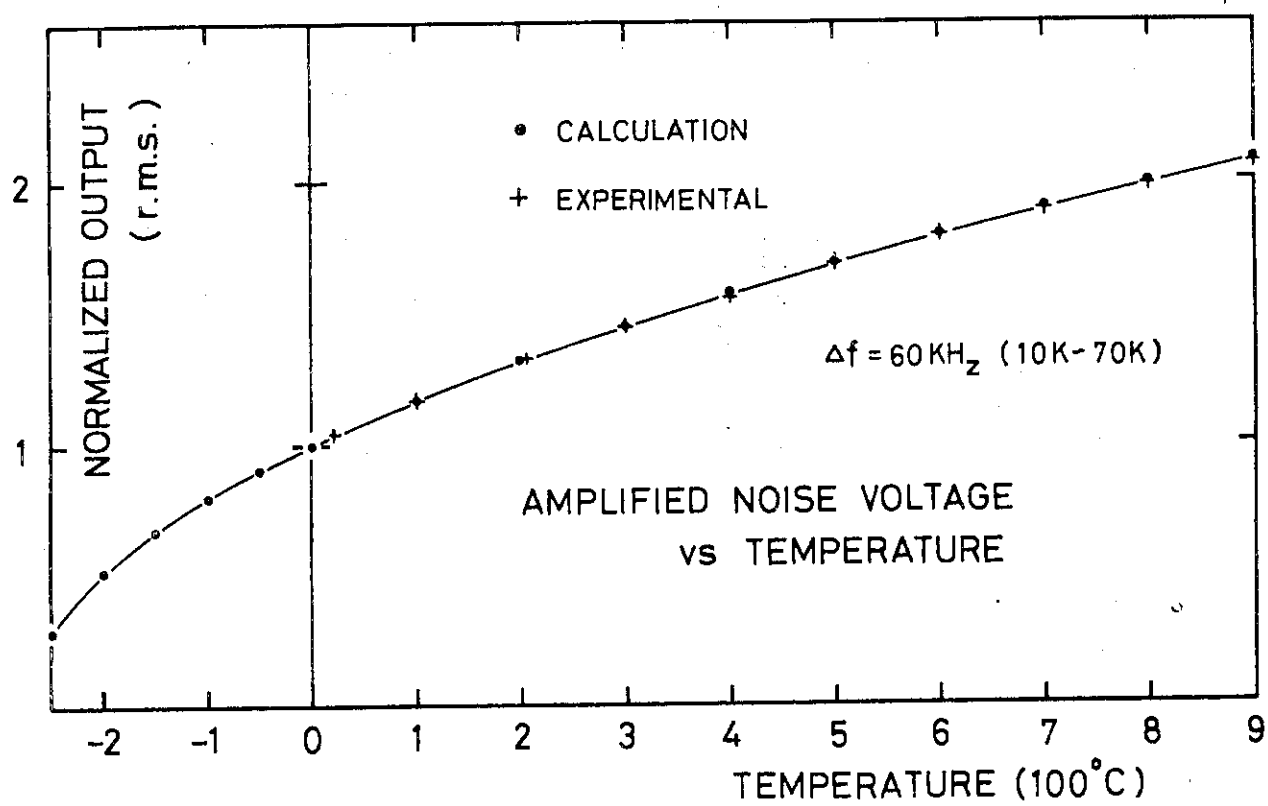


Fig. 5.3.3 Amplified Noise Voltage vs Temperature

## 5.4 Development of Organic and Inorganic Composite Insulated Cables

T. Kakuta, S. Horikoshi\*, H. Sunazuka\*\* and M. Fujiwara\*\*

The new type of soft-and-flexible cables have been developed and tested for the purpose of applying to instrumentation in high-temperature and high-radiation environments, existing in high-temperature reactor such as LMFBF and VHTR.

Figure 5.4.1 shows the cables which comprises two different composite insulating materials, i.e. one is composed of glass-fiber, polyimide-mica material and the other is of glass-fiber, polyimide material.

The developed cables have been tested under high-temperature and high-radiation environments. Figure 5.4.2 shows the insulation resistances at high-temperature and high-radiation environments. The insulation resistances were as very high as  $10\text{M}\Omega \cdot \text{km}$  under severe condition of  $400^\circ\text{C}$  and  $1 \times 10^6 \text{ R/hr.}$  The cables were able to retain its stable insulation layer even up to the gamma irradiation of  $1.4 \times 10^{10} \text{ R.}$

Furthermore the cables showed excellent fire resistivity during vertical tray flame tests based on IEEE383 standard. Figure 5.4.3 shows the insulation resistances measured during the tests. This means that the cables were able to retain its performance capabilities for hours in the case of fire accident.

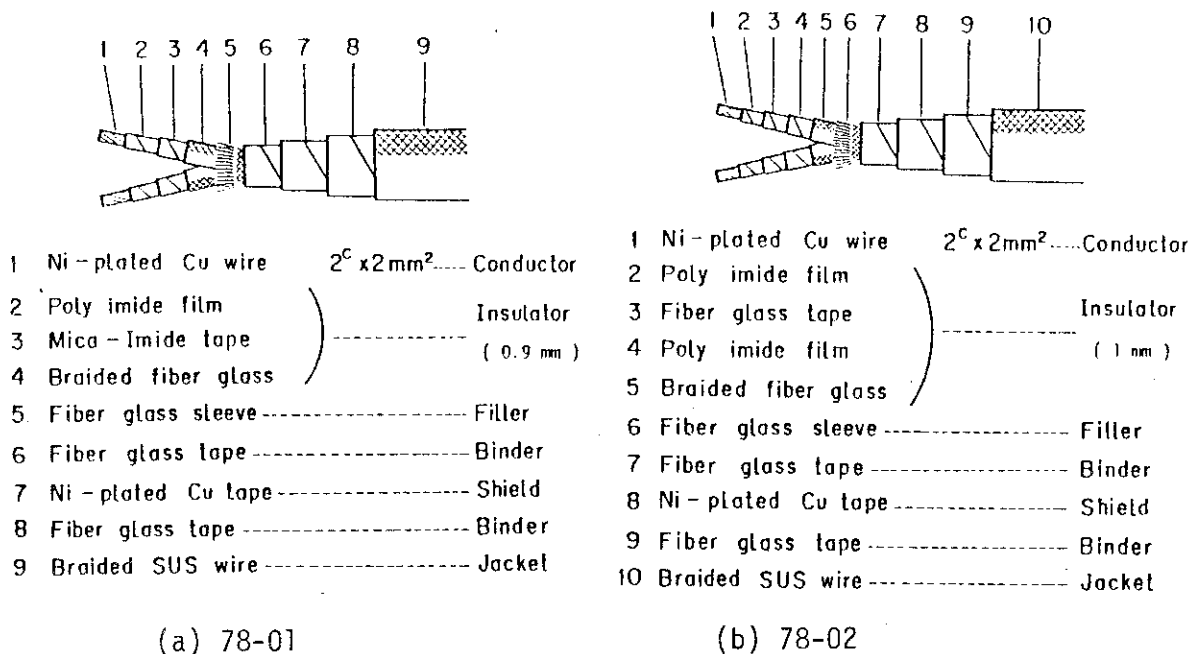


Figure 5.4.1 Organic-and-Inorganic Composite Insulated Cable

\* Power Reactor and Nuclear Fuel Development Corporation.

\*\* The Fujikura Cables Works, Ltd.

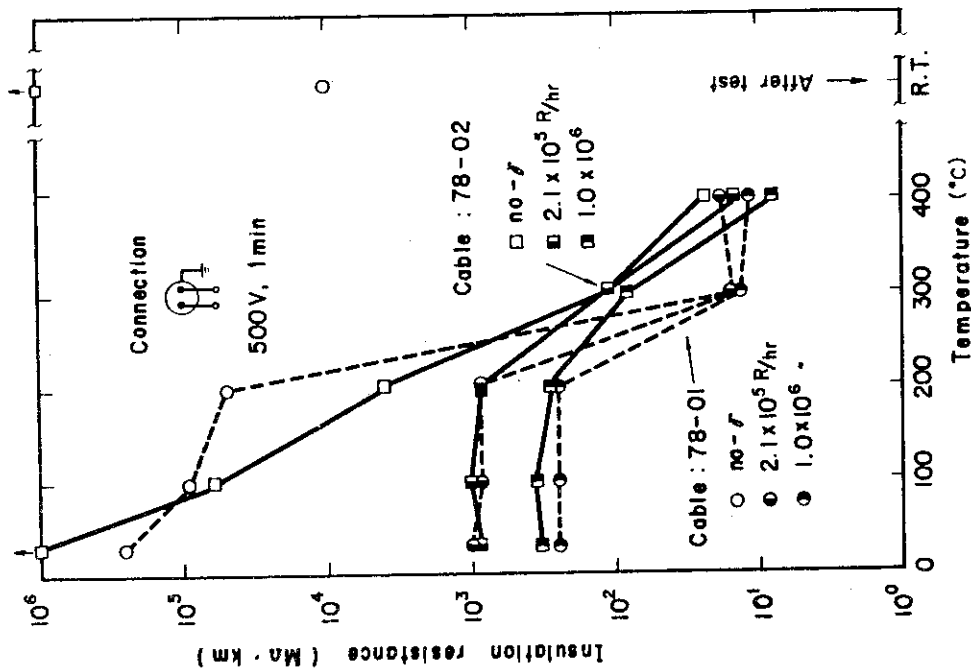


Figure 5.4.2 Insulation Resistances at high Temperature-and-Radiation Environment

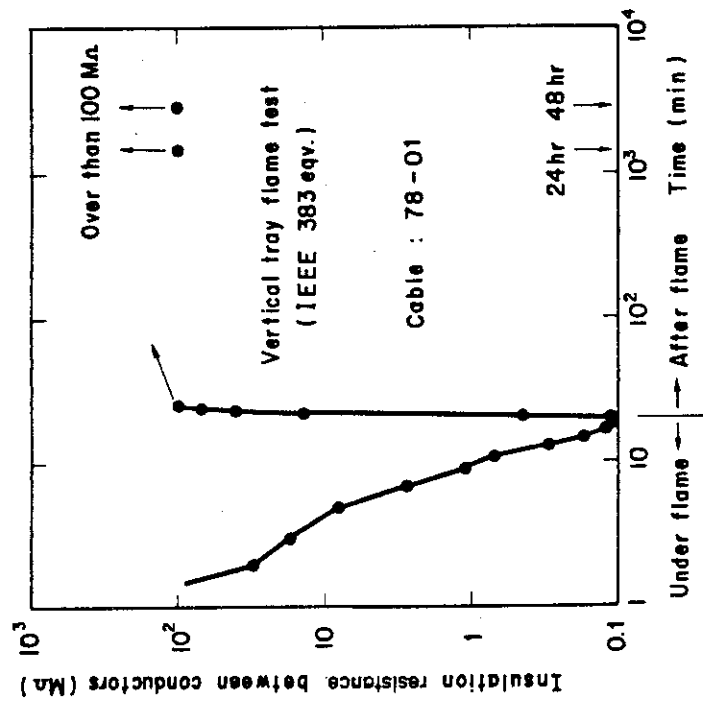


Figure 5.4.3 Insulation Resistances Measured During the Vertical Tray Flame Test

## 5.5 Development and Test of On-Line Cover-Gas Gamma-Ray Monitor for LMFBR

E. Sakai, K. Kubo\* and H. Yoshida

In order to obtain the basic data for designing the failed fuel detection and location system of proto-type fast breeder reactor "MONJU", the testing of various types of cover-gas monitor systems installed in the Cover-Gas Monitor Test Facility (CGMTF) was started in Japan Research Reactor 3.

Development of an on-line cover-gas gamma-ray spectrometer has been continued by adding a 16kw memory and one disk drive unit to PDP-11/05 computer and making some of necessary programs such as GAMMAJ, GAMMAX(A,B), GAMMAY(A,B), SOAPL2, COLECT(revised).

Adsorption and desorption characteristics of a room temperature charcoal unit of a cylinder type were measured using standard gases of 500, 1000 and 5000ppm Kr, Xe in He and Ar carrier. Flow rate and pressure dependence of adsorption and desorption was investigated. The charcoal was 50g Tsurumi coal 2GM packed in a 100cm<sup>3</sup> volume cylinder.

JRR-3 cover gas including  $10^{-4}$ ppb Kr-85m, 87, 88,  $1.5 \times 10^{-2}$ ppb  $^{133}\text{Xe}$ ,  $4.4 \times 10^{-3}$ ppb  $^{135}\text{Xe}$ ,  $1.4 \times 10^{-5}$ ppb  $^{138}\text{Xe}$ ,  $2.4 \times 10^{-6}$ ppb  $^{135\text{m}}\text{Xe}$  and  $2 \sim 8 \times 10^{-4}$ ppb  $^{41}\text{Ar}$  in He was flowed at 1l/min through the charcoal unit and a change in Ge(Li) detector peak counting rate of gamma-rays from the charcoal unit was measured. The saturated enrichment factors in the charcoal thus observed were  $33.2 \sim 45.6$  for Kr-85m, 87 and 88,  $136.4 \sim 467.9$  for Xe-133, 135m and 2.5 for  $^{41}\text{Ar}$ , respectively.

A membrane unit was also investigated by flowing the above described standard gases and JRR-3 cover gas. The enrichment factors depended on each run; this seems to be caused by different temperature of gas in each of the runs.

These results were reported in a contract report.<sup>1)</sup>

More detailed studies on various type of cover-gas monitor will be carried out in the next contract with Power Reactor and Nuclear Fuel Development Corporation.

## References

- 1) Sakai, E., Kubo, K., Yoshida, H.: "Development and Test of Cover-Gas On-Line Gamma-Ray Monitor (II)", SJ 250 80-27/JAERI-memo 8962/SDG-8009 (in Japanese) (June 1980).

---

\*Visiting engineer, on leave from Tokyo Shibaura Electric Corporation.

## 5.6 Temperature Dependence of $^3\text{He}$ Proportional Counter Performance

E. Sakai, K. Kubo\* and H. Yoshida

$^3\text{He}$  proportional counters are said to be able to operate at temperatures up to  $200^\circ\text{C}$ , but only one report was found which described the temperature dependence of the plateau curves.<sup>1)</sup>

The temperature dependence of the thermal neutron detection performance of seven different  $^3\text{He}$  proportional counters manufactured by six different manufacturers has been measured in the temperature range from room temperature to  $300^\circ\text{C}$ . The highest temperatures of the counters were chosen as those where spurious pulses started. Their anode voltages were varied widely from the voltage that gave ionization chamber operation to that gave gas multiplication of more than 100. The typical performance is summarized in Table 5.6.1. The second group of the lines in the table lists the performance measured at the manufacturer's suggested anode voltages while the fourth group of the lines lists that measured at the voltages giving the best FWHM's at room temperature. Both voltages were found not to be the same.

The following summarizes the results of our measurements.

- (1) One counter showed spurious pulses at  $100^\circ\text{C}$ , three at  $200^\circ\text{C}$  and three at  $300^\circ\text{C}$ . The thermal neutron counts were constant unless spurious pulses appeared.
- (2) Five counters recovered their original performance at room temperature after cooled down from the highest temperatures they had experienced while one counter lost its original performance and the other which had an Al wall punctured at  $300^\circ\text{C}$ .
- (3) An increase of the pulse heights of the thermal neutron peaks was observed as the temperature that lost its original performance after the high temperature measurement.
- (4) The shape of the thermal neutron peak became more asymmetrical and the FWHM became wider as the temperature increased.
- (5) The extent of the FWHM degradation differed from counter to counter.
- (6) The extent of the FWHM degradation was small at the voltage that gave the ionization chamber operation and was larger as the anode voltage increased, i.e., as the gas multiplication increased.

---

\*Visiting engineer, on leave from Tokyo Shibaura Electric Corporation.

- (7) The risetimes of the thermal neutron pulses of  $^3\text{He}$  proportional counters exhibited little temperature dependence.<sup>2)</sup>
- (8) The above observations indicate that the variance in the gas multiplication increases as the temperature increases.
- (9) When one plans to perform neutron spectroscopy at elevated temperatures, he must bear the above observations in mind.
- (10) The cause of the temperature dependence of  $^3\text{He}$  proportional counters are not known and needs further investigation.

This work was reported in several meetings<sup>3) ~ 5)</sup> and published in IEEE Transactions on Nuclear Science, vol. NS-27, No. 1.<sup>6)</sup>

#### References

- 1) Myers, Jr., J. E.: "High Temperature Helium-3 Detectors", IEEE Trans., NS-14(1), pp.416-421 (1967).
- 2) Sakai, E., Kubo, K., Yamagishi, H., Itoh, H.: "Performance of Fuel Failure Detection System in Sodium In-Pile Loop Experiment(VI)" (in Japanese), SJ 250 78-22/JAERI-memo 7754(June 1978).
- 3) Sakai, E., Kubo, K.: "Temperature Performance of  $^3\text{He}$  Proportional Counters", Fall Meetings of Japanese Society of Applied Physics, Hokkaido University, October 2, 1979.
- 4) Sakai, E., Kubo, K.: "Temperature Performance of  $^3\text{He}$  Proportional Counter (2)", Fall Meeting of Japan Physical Society, 2pKD2, Kōchi University, October 2, 1979.
- 5) Sakai, E., Kubo, K., Yoshida, H.: "Temperature Dependence of Thermal Neutron Detection Performance of  $^3\text{He}$  Proportional Counters", 1979 Nuclear Science Symposium, San Francisco, October 19, 1979.
- 6) Sakai, E., Kubo, K., Yoshida, H.: "Temperature Dependence of Thermal Neutron Detection Performance of  $^3\text{He}$  Proportional Counters", IEEE Transactions on Nuclear Science, NS-27(1), pp.776-782(1980).



Table 5.6.1 Specifications and performance of  $^3\text{He}$  proportional counters tested

	Reuter Stokes RS-P4-810-207 U 3974	Reuter Stokes RS-P4-812-31 M 2588	20th Century 31 He <sup>3</sup> /380/258 7838-445	LND 2521 81014-78-14	Hitachi Electronics HS811 K 7002	Harshaw H3 6S D 8979	Texas Nuclear Textilum 9341 1719
Sensitive region	1"dia. $\times$ 10"	1"dia. $\times$ 12"	1"dia. $\times$ 310mm	1"dia. $\times$ 10"	1"dia. $\times$ 257mm	1"dia. $\times$ 6"	1"dia. $\times$ 195mm
Cathode material	304SS	Al	SS	446SS	SS	SS	SS
Counting gas	$^3\text{He}$ 10atm	$^3\text{He}$ 4atm	$^3\text{He}$ 5atm	$^3\text{He}$ 10atm	$99.9\% ^3\text{He} + \text{Ar}, 6\text{atm}$	$^3\text{He}$ 1atm + Kr 4atm	$^3\text{He}$ 4atm + Kr 2atm
Thermal neutron sensitivity	40cps/nv		54.3cps/nv	38cps/nv	37cps/nv		
Operation temperature	Up to 150°C	Up to 150°C	200°C possible (catalogue)*	-50°C to 150°C	Up to 100°C	Up to 175°C	Up to 200°C
Operating voltage	3300V - 3800V	3000V	1412V	3000V	2900V		
Output charge	$4.9 \times 10^{-14}\text{C}$ (3550V)	$1.8 \times 10^{-14}\text{C}$ (3000V)	$4.2 \times 10^{-14}\text{C}$ (1400V)	$6.2 \times 10^{-15}\text{C}$ (3000V)	$6.3 \times 10^{-15}\text{C}$ (2900V)		
Gas multiplication(M)+1	14.4 (3550V)	5.2 (3000V)	12.2 (1400V)	1.65 (3000V)	185.7 (2900V)		
Energy resolution** (FWHM) at 25°C	6.3% (3550V)	4.8% (3000V)	6.4% (1400V)	12.5% (3000V)	11.8% (2900V)		
Risetime at 25°C	About 1 $\mu$ s (3550V)	About 0.9 $\mu$ s (3000V)	About 0.7 $\mu$ s (1400V)	About 0.4 $\mu$ s (3500V)			
Temperature dependence of FWHM**							
50°C	11.7% (3550V)	9.4% (3000V)	18.2% (1400V)	13.0% (3000V)	40.2% (2900V)		
100°C	13.2% (3550V)	18.4% (3000V)	149% (1400V)	12.0% (3000V)	56.3% (2900V)		
150°C	55.7% (3550V)	23.5% (3000V)	108% (1400V)	14.4% (3000V)			
Anode voltage which gave gas multiplication M=0 at 25°C	1500V	1500V	450V	2000V	1100V	600V	800V
Output charge at M=0 and 25°C	$4.12 \times 10^{-15}\text{C}$	$4.57 \times 10^{-15}\text{C}$	$4.44 \times 10^{-15}\text{C}$	$3.77 \times 10^{-15}\text{C}$	$5.05 \times 10^{-15}\text{C}$	$4.20 \times 10^{-15}\text{C}$	$4.95 \times 10^{-15}\text{C}$
Apparent W value at 25°C	29.0eV	26.1eV	26.9eV	31.7eV	23.7eV	28.5eV	24.2eV
Energy resolution (FWHM) at M=0, 25°C	13.2%	13.8%	13.3%	17.5%	12.0%	10.7%	11.4%
Anode voltage which gave the best FWHM at 25°C***	3500V	3250V	1000V	4000V	2000V	1500V	1750V
Gas multiplication(M)+1	10.4	8.5	2.95	6.3	3.7	4.8	33.0
Temperature dependence of FWHM							
25°C	4.5%	4.1%	7.2%	5.3%	7.8%	5.8%	4.5%
$\sim 60^\circ\text{C}$	10.3% (60°C)	10.9% (56°C)	9.9% (63°C)	9.6% (60°C)	9.3% (60°C)	6.0% (62°C)	5.8% (60°C)
$\sim 100^\circ\text{C}$	15.6% (100°C)	19.5% (98°C)	19.8% (111°C)	13.8% (110°C)	13.8% (109°C)	7.1% (108°C)	11.5% (117°C)
$\sim 150^\circ\text{C}$	28.8% (152°C)	30.9% (145°C)	59.3% (162°C)	35.2% (150°C)		9.1% (150°C)	15.9% (160°C)
$\sim 200^\circ\text{C}$	30.8% (190°C)	34.3% (195°C)		48.7% (199°C)		10.2% (190°C)	19.0% (208°C)
$\sim 240^\circ\text{C}$	30.1% (240°C)					11.3% (235°C)	
$\sim 300^\circ\text{C}$	30.6% (300°C)					12.7% (303°C)	
Temperature where break-down pulses appeared	300°C	200°C	300°C	200°C	100°C	300°C	200°C
Note		Detector wall punctured at 300°C.	Detector performance deteriorated permanently after temperature performance measured.				

\*Up to 80°C (letter) \*\*Amplifier shaping time was 3 $\mu$ s-3 $\mu$ s. \*\*\*Amplifier shaping time was 5 $\mu$ s-5 $\mu$ s.

5.7 Fabrication Technique Development of  $\text{HgI}_2$  Radiation Detectors

E. Sakai and K. Kubo\*

Recently appeared  $\text{HgI}_2$  detectors seems to find special applications in which room temperature operation is inevitably required, but, their commercially supplying sources are not yet established. Therefore, we decided to fabricate  $\text{HgI}_2$  detectors by ourselves. We reported that very simple fabrication method using vapor transport in an evacuated ampoule could make small detectors of about 5 keV energy resolution for 60 keV gamma-rays, but the yield of getting the detectors of a reasonable performance was very low.<sup>1)</sup> Schieber, et al.<sup>2)</sup> reported that temperature oscillation method could make large crystals using a horizontal furnace or vertical furnace, although a special solution growth was successfully applied to make large crystals.<sup>3)</sup>

We started to built vapour phase furnaces of temperature-oscillation method of horizontal and vertical types which were now in a near complete stage as shown Photo. 5.7.1. We will start crystal growth using these furnaces soon and apply these detectors to plasma X-ray spectroscopy in Japan Fusion Tokamak 2 and also to catheters for medical use in the future.

## References

- 1) Nakatani H., Sakai E., Katagiri M.: "Fabrication of  $\text{HgI}_2$  Nuclear Radiation Detectors", JAERIM 8478/SDG-79016 (in Japanese) (October 1979).
- 2) Schieber M., Beinglass I., Dishon G., Holzer A.: "Growth of large crystals of  $\text{HgI}_2$  from the vapor phase by temperature-oscillation methods", in 1976 Crystal Growth and Materilas, ed. E. Kaldis and H.J. Scheel (North-Holland Publishing Co., 1977), pp.279-300.
- 3) Friant A., Mellet J., Mohammed Brahim T.: " $\text{HgI}_2$  Detectors from Solution Grown Crystals", IEEE Trans., NS-27(1), pp.281-285 (1980).

---

\* Visiting engineer, on leave from Tokyo Shibaura Electric Corporation.

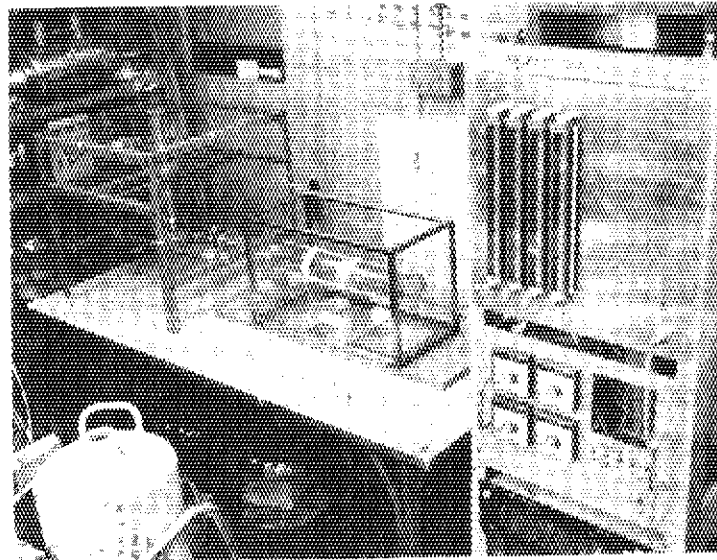


Fig. 5.7.1 Photo of HgI<sub>2</sub> crystal growing furnaces of temperature-oscillation method of horizontal (right) and vertical type (left)

## 5.8 Performance of an Anticoincidence-Shielded High-Purity Ge Gamma-Ray Spectrometer

E. Sakai, K. Kubo\* and H. Yoshida

An anticoincidence-shielded high-purity Ge gamma-ray spectrometer was built combining a 10" dia.  $\times$  10" long NaI(Tl) scintillation annulus having a 70mm dia. through hole (10.7% energy resolution for 662keV gamma-ray), a 2.5" dia.  $\times$  3" long NaI(Tl) scintillation annulus, and a closed-end high-purity Ge detector (PGT IGC 45 $\times$ 45 SIN340; 1.78keV resolution, 11.5% peak detection efficiency, 44:1 peak-to-Compton ratio for 1333keV gamma-rays) in a 15cm thick lead shield. The performance of various types of the spectrometer was investigated. Some of the results are as follows.

- (1) A gamma-ray beam was directed into the high-purity detector from the directions perpendicular to the detector axis and anti-coincidence shielding was applied by the plug and the annulus detectors. The peak-to-Compton ratios for 662keV and 1333keV gamma-rays were 917 as shown in Fig. 5.8.1 and 480, respectively. The peak absolute detection efficiencies were  $1.0 \times 10^{-5}$  and  $4.3 \times 10^{-6}$  cts/photon for a source-to-detector axis distance of 488mm.
- (2) Weak gamma-ray sources were placed in a space between the high-purity Ge detector and the plug detector. The two detectors were surrounded by the annulus detector. The anticoincidence measurement using the plug and the annulus gave peak-to-Compton ratios of 609, 636 and 146 for 662keV, 834.8keV and 1333keV gamma-rays from  $^{137}\text{Cs}$ ,  $^{54}\text{Mn}$  and  $^{60}\text{Co}$ , respectively, as shown in Fig. 5.8.2. The peak absolute detection efficiencies were  $1.7 \times 10^{-2}$ ,  $1.0 \times 10^{-2}$ , and  $1.6 \times 10^{-3}$  cts/photon, respectively. Using an observed pulse height distribution of the background gamma-rays and peak detection efficiencies, the detection limits (at  $3\sigma$ ) for 1000 min counting were calculated to be 0.72pCi for a point source and 1.9pCi for a 1367cm<sup>3</sup> volume sample of 0.334g/cm<sup>3</sup> density.
- (3) The pulse height distributions from the Ge detector was coincidence-gated by the plug together with the annulus anticoincidence. This arrangement proved to be very useful to detect weak radioactivities emitting coincident gamma-rays.

The spectrometer performance, especially, very high peak-to-Compton

---

\*Visiting engineer, on leave from Tokyo Shibaura Electric Corporation.

ratios, is the best one achieved at least in Japan, and the spectrometer will be used various measurements in the future.

Some of the results were reported at the two meetings.<sup>1)2)</sup>

#### References

- 1) Sakai, E., Kubo, K., Yoshida, H.: "Performance of an Anticoincidence-Shielded High-Purity Ge Gamma-Ray Spectrometer", Annual Meeting of Atomic Energy Society of Japan, F15, Nagoya University, March 27, 1980.
- 2) Sakai, E., Kubo, K., Yoshida, H.: "Performance of an Anticoincidence-Shielded Type High-Purity Ge Gamma-Ray Spectrometer", Spring Meeting of Japanese Society of Applied Physics, Yamanashi University, April 3, 1980.

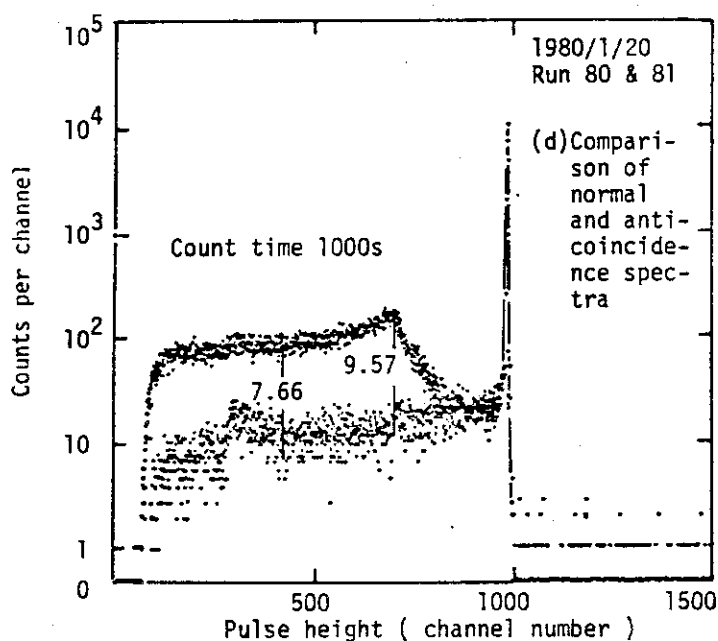


Fig. 5.8.1 Normal and anticoincidence pulse height distributions of Cs-137 gamma-ray beam obtained from an anticoincidence-shielded high-purity gamma-ray spectrometer

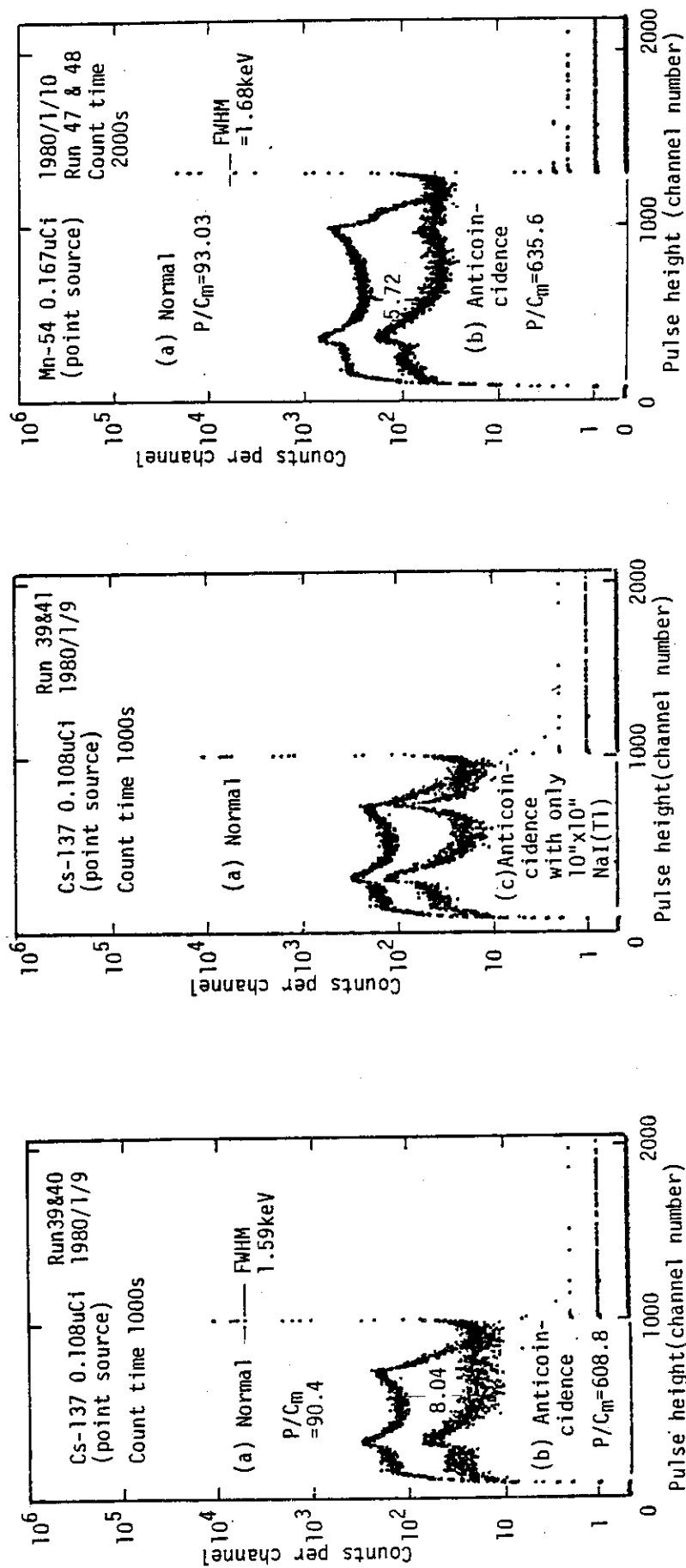


Fig. 5.8.2 Gamma-ray pulse height distributions of Cs-137, Mn-54 and Co-60 sources in an anticoincidence-shielded high-purity gamma-ray spectrometer

## 5.9 Nondestructive Measurement of FP plateout Density Using a Portable Ge(Li) Detector with a Lead Collimator

M. Katagiri, H. Terada, H. Takahashi and N. Wakayama

A nondestructive method for qualitative and quantitative analysis of fission product deposited on inside surfaces of the primary duct has been developed.<sup>1),2)</sup> Fission products are measured by in-situ measurements of gamma-rays from plateout nuclides using a portable Ge(Li) detector with a lead collimator. It is one of the important problems in this method to obtain conversion coefficients for calculating the plateout density ( $\mu\text{Ci}/\text{cm}^2$ ) on the inner surface of the primary ducts from gamma-ray peak counting rates. The conversion coefficient can be obtained using gamma-ray peak detection efficiencies and geometry between the detector and ducts. Mock-up experiments using standard gamma-ray sources and mock-up ducts were carried out to estimate the error of this conversion coefficient. As the result of experiments, it was revealed that the error was 25% ~ 50% at a straight multi-co-centric ducts.

The preliminary measurements of FP plateout in OGL-1 primary ducts were carried out after shut downs of JMTR 39th to 44th operating cycles. Three high temperature ducts, a regenerative heat exchanger and a filter were measured. Figure 5.9.1 shows conversion coefficients, as function of gamma-ray energy at every measuring point, obtained by above-mentioned calculation method. The plateout densities in OGL-1 primary ducts were calculated by using these conversion coefficients.

Plateout distributions of Ag-110m, Mn-54, Co-60, Zn-65, Sb-124 and I-131 were obtained at every operating cycle. Figure 5.9.2 shows plateout distribution of Ag-110m as parameter of the operating cycle. As the result of the analysis, it was revealed that Ag-110m removed downstream to lower temperature sections. Sb-124, Zn-65 and I-131 also showed the same plateout behavior. Moreover, Co-58, Eu-152, Cr-51, Hf-181, Sc-46, Ta-182 and La-140 were observed as function of the operating cycle. Figure 5.9.3 shows plateout densities of Hf-181 at a filter as function of the operating cycle. Cr-51, Sc-46 and Ta-182 also showed the same plateout behavior. The analysis of these plateout behavior has been continued.

Besides, the method of in-situ measurements was investigated in detail and arranged to an internal report. And, this method was applied to the design of OGL-1 FP plateout measurement system.

## References

- 1) Katagiri M., Terada H., Takahashi H.: "Measurement of FP Plateout Using a Portable Ge(Li) Detector" JAERI-M 7579 (1978)
- 2) Terada H., Katagiri M., Takahashi H., Wakayama N.: "In-Situ Measurement of Fission Product plateout in In-Pile Gas Loop Using Portable Ge(Li) Gamma-Ray Spectrometer" Journal of Nuclear Science and Technology Vol. 17 No. 3, pp. 225~240, (1980)

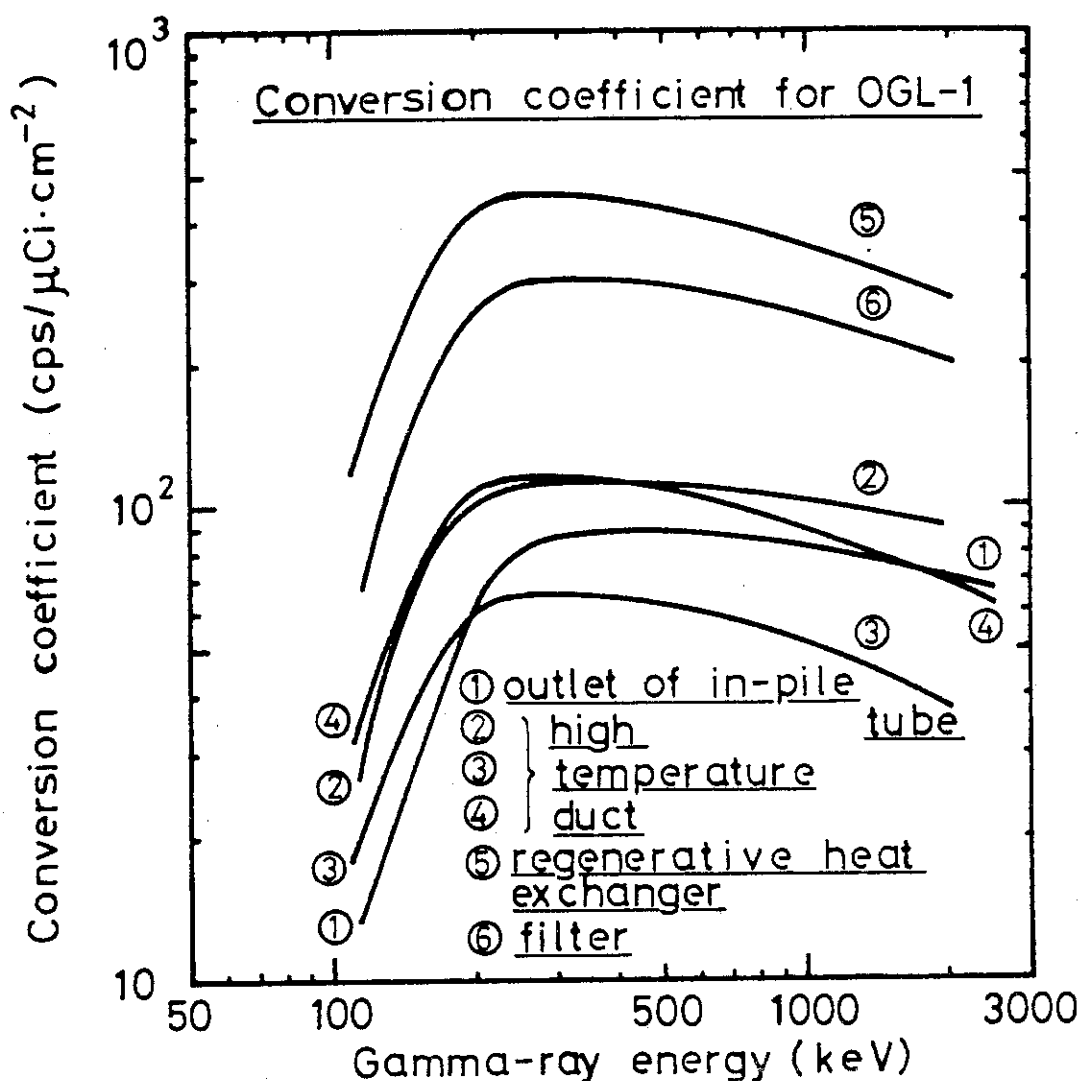


Fig. 5.9.1 Fission product plateout conversion coefficients for various measurement points in OGL-1



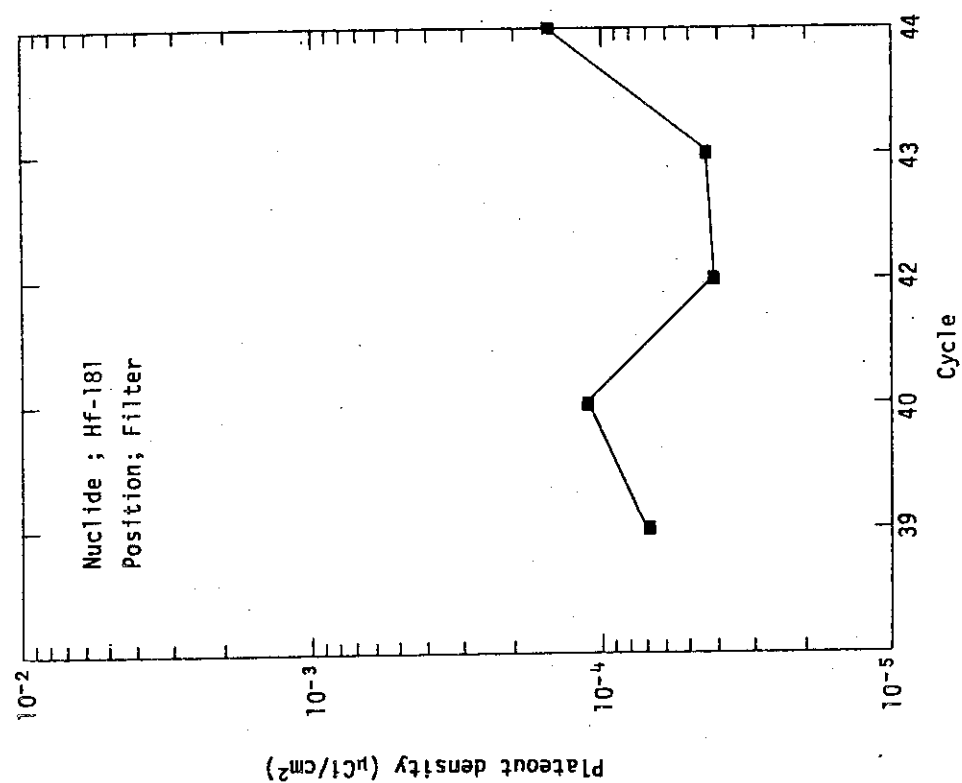


Fig. 5.9.3 Plateout density of Hf-181 measured at OGL-1 filter as function of JMTR operating cycle

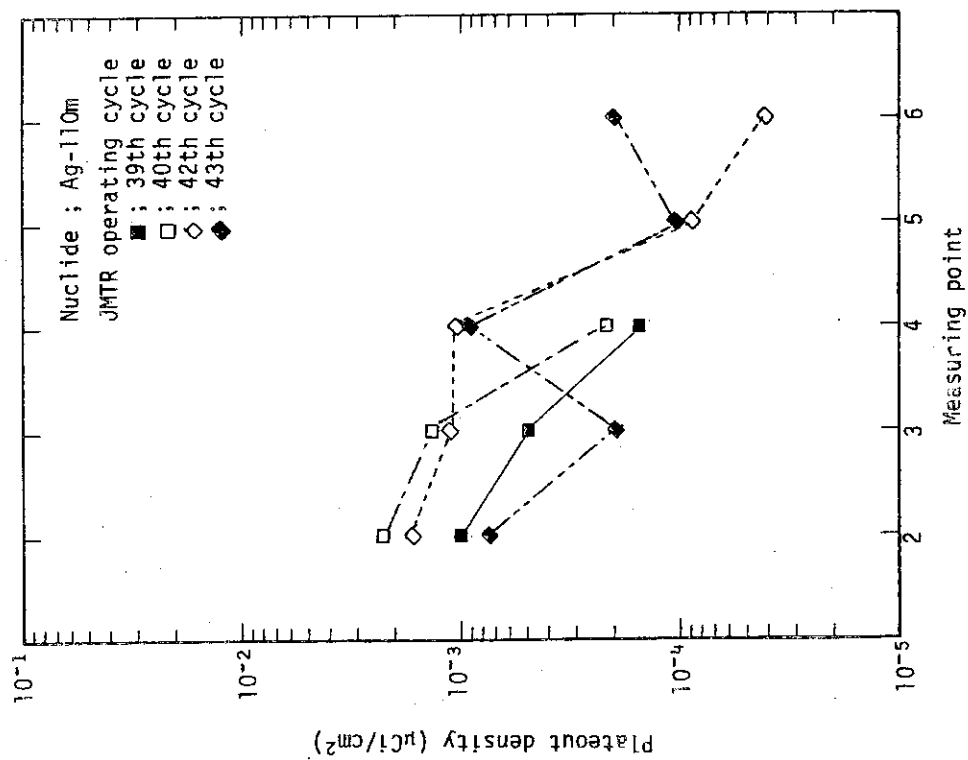


Fig. 5.9.2 Distributions of plateout densities of Ag-110m measured at OGL-1 primary system in JMTR 39th to 43th cycles

## 5.10 Development of Passive Gamma Type Nondestructive Nuclear Material Assay Meter System

H. Yagi, H. Gotoh and Y. Ikku

An assay meter with high portability was constructed basing on a formerly developed transportable type passive gamma assay meter<sup>1)</sup>. The total weight of this assay system is lightened by simplifying the part of pulse height analysis with the dual use of the memory region of a micro-computer for the storage of pulse height distribution. An analysis program was developed to the attribute test of plutonium samples for the system and its practicality was tested successfully.

The hardware of the system is composed of four parts: an analyzer part for pulse height analysis and data processing, a console typewriter for key operation and print-out, a floppy disk for data storage and a gamma-ray detection part including a bias supply and an amplifier. The composition is shown in Fig. 5.10.1. The analyzer part uses a DEC LSI-11/02 with 28KW RAM and an 80KB bubble memory as system device. An ORTEC model 800 ADC is used and connected to the computer memory with a DMA type ADC interface. The specifications of pulse height analysis includes a resolving power of 4096 channels and a data size of 32 bits per channel. The ADC interface has a presetable timer up to  $10^4$  seconds. An XY display controller is provided to observe the pulse height distribution by connecting an oscilloscope to external connectors. Table 5.10.1 shows weights, sizes and the power consumption of processor and floppy disk. Photo 5.10.1 shows three parts except the detection part.

A model flow chart of the assay system is shown in Fig. 5.10.2 for attribute mode measurement. The statistical error is evaluated intermittently in the course of measurement and counting is continued until the error is diminished within a preset interval. When the test error is satisfied, the measurement result is judged and a conclusion is printed. When a series of measurements is completed, a report is produced.

The analysis program for plutonium derives relative abundances of  $^{239}\text{Pu}$ ,  $^{241}\text{Pu}$  and  $^{241}\text{Am}$  from a peak complex in a specified narrow energy region (330 ~ 345 keV), which cancels effects of energy dependence of detection efficiency and attenuation<sup>2,3)</sup>. The sequence of analysis is as follows. Values of peak centers and the peak width are evaluated and the background is subtracted. Normalized response profiles are formed basing on gamma-ray energies and branching ratios for three nuclides mentioned

above which contribute the peak complex. Finally abundances of nuclides are computed using these spectra. Fig. 5.10.3 shows the flow of procedure. A precision of about 1% was attained by a 200 sec counting for plutonium samples of adequate amount. An analysis time of about 40 sec is needed after the completion of counting.

#### References

- 1) Reactor Engineering Division Annual Report, JAERI-M 8393 (1979), p.116
- 2) Baba H., Suzuki T., Nakahara Y., Yagi H., Okazaki S.: "Determination of Plutonium Isotopic Ratios by Ge(Li)  $\gamma$ -ray Spectrometry", JAERI-M 8450 (1979)
- 3) Baba H., Yagi H.: "Simulation for Isotopic Ratio Determination of Plutonium by Ge(Li)  $\gamma$ -ray Spectrometry", JAERI-M 8451 (1979)

Table 5.10.1 Dimensions, weights and the power consumption of the portable assay meter

	DIMENSION (mm)			WEIGHT (kg)	POWER (VA)
	W	H	D		
ANALYZER	225	315	495	18.1	130
FLOPPY DISK	175	315	495	12.7	50

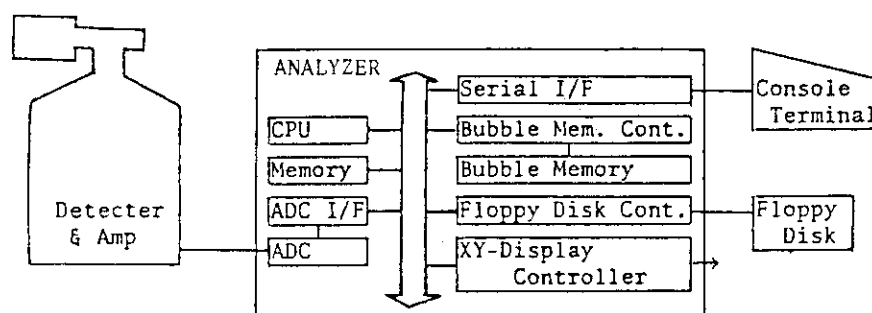


Fig. 5.10.1 System composition of the portable assay meter system

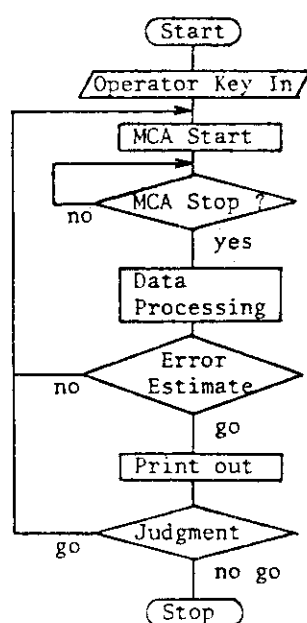


Fig. 5.10.2 Flow chart of the assay meter system for attribute mode measurement

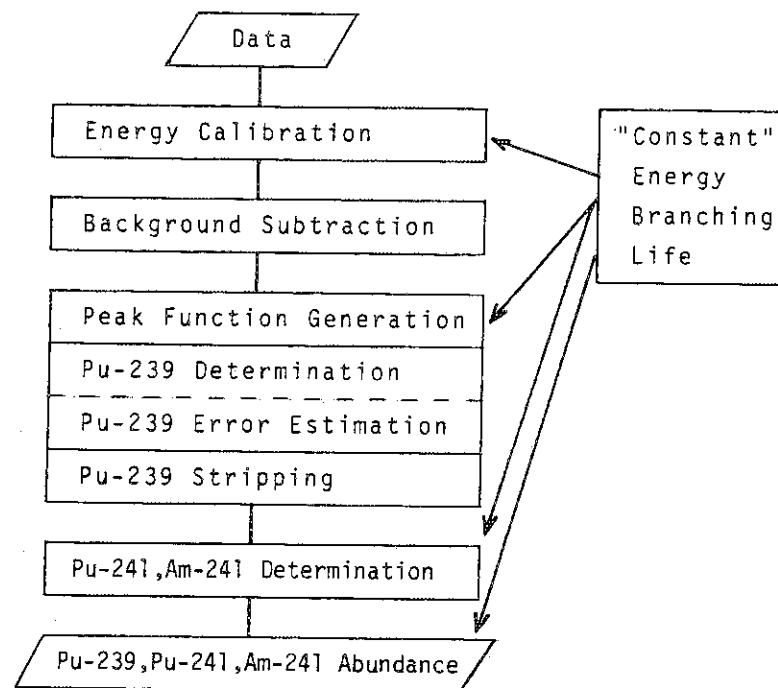


Fig. 5.10.3 Flow chart of the analysis program for plutonium

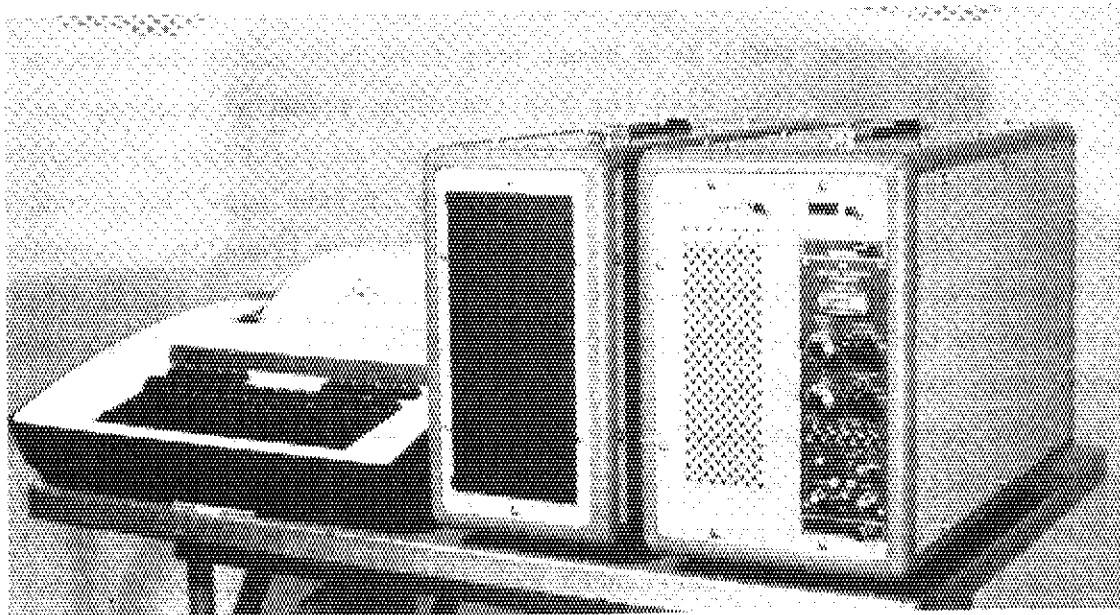


Photo 5.10.1 Standard arrangement of the portable assay meter system; analyzer (right), floppy disk (middle) and console (left)

## 5.11 Portal Monitor Development at FCA for IAEA Safeguards

T. Mukaiyama and H. Kuroi

The first stage of the portal monitor development at FCA has been completed as a measure of Containment and Surveillance<sup>1)</sup> (C/S) of IAEA Safeguards.

The main components of the portal monitor are the walk-through type metal detector (MD), the closed circuit TV with cassette video-recorder and tamper indication system. Metal detector, optical switches, intrusion sensors and TV cameras are placed inside the detection chamber located at the exit of FCA reactor room (Photo 5.11.1). Electric signals are controlled and processed by the controller. The operation/display unit (Photo 5.11.2) is located in IAEA inspector's office at the west wing of FCA building. The system turn on/off, check of the system malfunction, display and recording of the status inside the detection chamber are handled by this unit. The system status and alarms activated are indicated on the graphic display panel. The signal transfer between control/display unit and the controller is handled by multiplexer-transmitters, a kind of encrypted signal transfer.

The most important component of this portal monitor is the metal detector. The preliminary test was performed to know the characteristics of the metal detector (MD). The MD response (the amplified output of the magnetic field coils) to a clean tester which is a human body free from metal substances except a zipper is lower than 2.4V for the traveling speed of a clean tester between 0.20 to 2.5m/sec. When a clean tester carries one piece of stainless steel plate of 2"x2"x1/16" or uranium metal plate of same size, MD output is higher than 7V regardless of the plate direction to the traveling direction and of traveling speed. This result indicates that our MD can distinguish clearly between the clean tester and the human body carrying metal substances of larger than the test piece.

The test revealed that even a thrown metal substance can be detected by this metal detector. The output of MD for a stainless steel plate of 2"x2"x1/16" which was thrown along the passage inside MD was higher than 6V. It has been widely said that thrown metal substances are very difficult to be detected by a metal detector, but our metal detector did it!

Under the research agreement between JAERI and IAEA, some modification of the system is expected so as this portal to be accepted as a IAEA Safeguards sensor.

Reference

- 1) Mukaiyama, T. and Kuroi, H.: "Reactor Engineering Division Annual Report" p122, JAERI-M 8393 (1979).

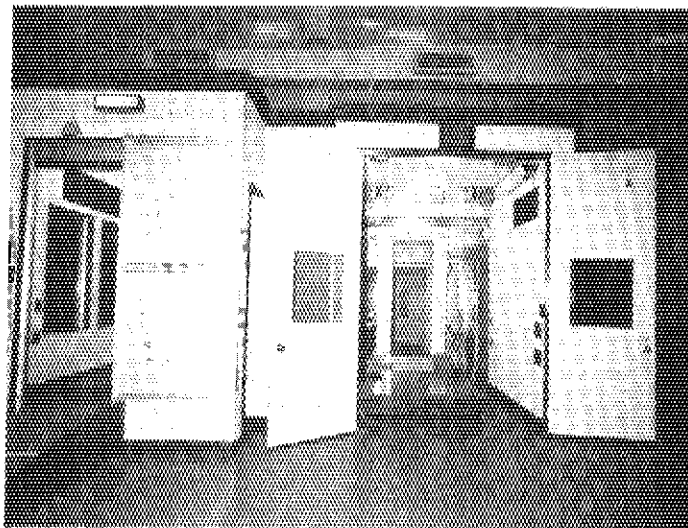


Photo 5.11.1 Detection unit of FCA portal monitor

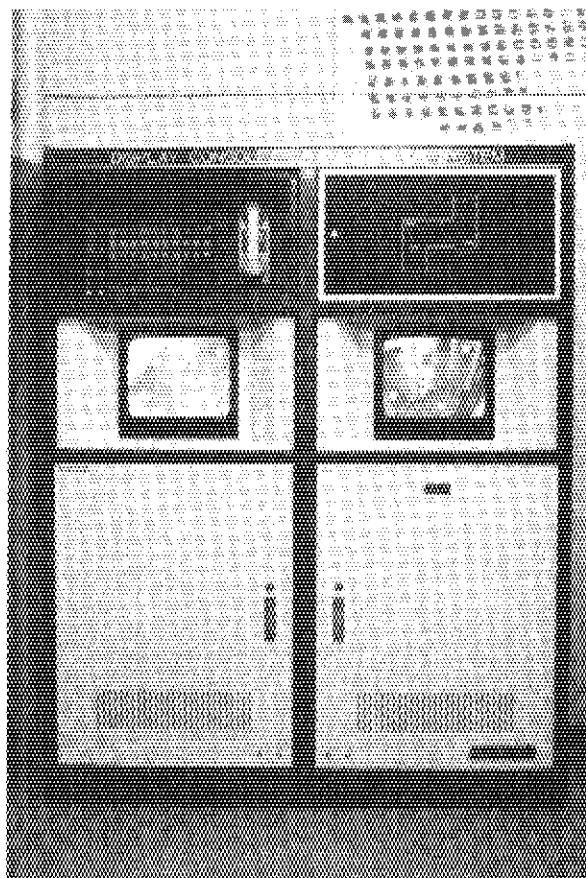


Photo 5.11.2 Operation/display unit of FCA portal monitor



## 5.12 Uncertainty Induced by Count Statistics in Enrichment Measurement with SAM-2

H. Gotoh

When the enrichment of uranium samples is measured with SAM-2, it is important to confirm that the apparatus including conditions in use is suited to samples to be tested. This can be performed by ascertaining that the enrichment of the third standard falls into its confidence interval deduced from counts taken against three standards and enrichment values of first two standards.

In practice inspectors are frequently forced to decide the counting time as short as the precision of enrichment measurement permits.

Information necessary to these decisions is afforded by taking six counts separately in channel 1 and in channel 2 open against three standards or sample.

Let  $C_{11}$  and  $C_{21}$  be counts of SAM-2 in channel 1 open and in channel 2 open respectively for a standard of known enrichment  $E_1$  in counting time  $T_1$ , and let  $C_{12}$  and  $C_{22}$  be the same for another standard of known enrichment  $E_2$  in counting time  $T_2$ . Denoting by  $C_1$  and  $C_2$  the same for a sample of unknown enrichment  $E_3$  in counting time  $T$ , we obtain an equation for the point estimation  $E$  of  $E_3$

$$\begin{vmatrix} C_{11} & C_{21} & E_1 T_1 \\ C_{12} & C_{22} & E_2 T_2 \\ C_1 & C_2 & E T \end{vmatrix} = 0. \quad (1)$$

The solution is given by

$$E = \frac{-1}{T \cdot \Delta} \cdot (\hat{C}_1 \cdot C_1 + \hat{C}_2 \cdot C_2), \quad (2)$$

where  $\Delta$  is the cofactor of element  $ET$  in the determinant in the left side of eq.(1)

$$\Delta = \begin{vmatrix} C_{11} & C_{21} \\ C_{12} & C_{22} \end{vmatrix}, \quad (3)$$

and  $\hat{C}_1$  and  $\hat{C}_2$  are respectively cofactors of elements  $C_1$  and  $C_2$

$$\tilde{C}_1 = \begin{vmatrix} C_{21} & E_1 T_1 \\ C_{22} & E_2 T_2 \end{vmatrix}, \quad \tilde{C}_2 = (-1) \cdot \begin{vmatrix} C_{11} & E_1 T_1 \\ C_{12} & E_2 T_2 \end{vmatrix}. \quad (4)$$

As six C's are independent random variables of Poisson type, E is a random variable dependent on C's, and E is approximately distributed normal, then the standard deviation of E is represented as

$$\sigma_E = \frac{1}{T} \cdot \left[ \sum_{i=1}^2 \left\{ \sum_{j=1}^2 \left( \frac{\partial E}{\partial C_{ij}} \right)^2 \cdot C_{ij} + \left( \frac{\partial E}{\partial C_i} \right)^2 \cdot C_i \right\} \right]^{1/2}. \quad (5)$$

This reduces to

$$\sigma_E = \frac{1}{T \cdot \Delta} \cdot \left\{ \sum_{i=1}^2 \left( \sum_{j=1}^2 \tilde{C}_{ij}^2 \cdot C_{ij} + \tilde{C}_i^2 \cdot C_i \right) \right\}^{1/2}, \quad (6)$$

where  $\tilde{C}_{ij}$  is the cofactor of element  $C_{ij}$  ( $i=1,2; j=1,2$ ). The 95% confidence limits for the enrichment of the sample are given by

$$\left. \begin{aligned} E_{\text{lower}} &= E + 1.960 \sigma_E \\ E_{\text{upper}} &= E - 1.960 \sigma_E \end{aligned} \right\} \quad (7)$$

When we use the digital rate multiplier with two setting of  $n_1$  and  $n_2$ , the expression of the standard deviation of enrichment measurement is changed to

$$\sigma'_E = \frac{1}{T \cdot \Delta} \cdot \left\{ \sum_{i=1}^2 \left( \sum_{j=1}^2 \tilde{C}_{ij}^2 \cdot C_{ij} + \frac{1000}{n_i} \cdot \tilde{C}_i^2 \cdot C_i \right) \right\}^{1/2}. \quad (8)$$

The procedure for calculating E,  $E_{\text{lower}}$  and  $E_{\text{upper}}$  was programmed in Hewlett-Packard model 97 calculator. It is composed of four steps:

(1) key-in  $C_{11}$ ,  $C_{21}$ ,  $T_1$  and  $E_1$ ,

(2) key-in  $C_{12}$ ,  $C_{22}$ ,  $T_2$  and  $E_2$ ,

(3) key-in the confidence coefficient, and obtain the inverse

cumulative normal distribution corresponding to the coefficient,

and (4) key-in  $C_1$ ,  $C_2$  and  $T$ , and obtain E,  $E_{\text{lower}}$  and  $E_{\text{upper}}$ .

The program can also be used with model 67.

The routine presented above was tested in a physical inventory taking of uranium plates and blocks for the Fast Critical Assembly of JAERI.

## 5.13 Program Development for Canberra Industries 8100/Quanta System

H. Yoshida, K. Kubo\* and E. Sakai

In the previous report,<sup>1)</sup> we described that the programs to collect and analyze the data of gamma spectra obtained from Ge(Li) detectors and scintillation counters by Canberra Industries 8100/Quanta System are prepared with programming language "CLASS" (Canberra Laboratory Automation Software System).<sup>2)</sup> Thereafter, the memory size of the PDP-11/05 computer of this System increased from 16k- to 28k-words: an additional disk drive unit which contains a fixed head type disk and a removable cartridge type disk has been connected to the computer. An increase of memory size in the computer made it possible to use longer programs which had been impossible before because of the memory size limitation. The resultant use of the three disks increased the number of 4096-channel-data sets obtained from MCA's (multichannel pulse height analyzers) to be able to store on a disk cartridge from 50 to 100.

The following change in the System was performed: (1) an additional MCA (Canberra Industries Model 8100) with a magnetic tape deck was connected to the computer; (2) an 8 input channel multiplexer was designed and added. The System block diagram is shown in Fig. 5.13.1.

To meet the added equipment and our experimental requirement, all of related programs were revised as follows.

(a) Maximum number of detectors available to calibrate channel number vs. energy characteristics was increased 5 to 10.

(b) The 'COLECT' program described in the last progress report<sup>1)</sup> was revised as follows: (b-1) this program performs a series of automatic measurements, that accumulates, stores and analyzes spectrum data up to 100 runs; the maximum number of the measurement condition sets was also increased 5 to 10: each set consists of detector number, collection time, and number of MCA's (#1 or #2); (b-2) after a data of spectrum was stored, one of three ways can be selected: one is to omit data analysis, second, to detect photopeaks, calculate their areas and FWHM's, third, to detect photopeaks, calculate their areas, estimate nuclides of isotopes, calculate their intensities and store the resultant data on a disk.

---

\*Visiting engineer, on leave from Toyko Shibaura Electric Corporation.

In addition to those mentioned above, following programs are developed.

(1) Two programs which analyze one or more spectrum data in series stored on the disk are developed; "GAMMAX" program detects photopeaks calculates their areas and FWHM's: "GAMMAY" program detects photopeaks, calculates their areas, estimates nuclides of isotopes, calculates their intensities and stores the resultant data on the disk.

(2) "LIN" program<sup>3)</sup> computes the coefficients in the formulae that relate the channel numbers of gamma-ray photopeaks obtained from MCA to the energy values.

(3) "AR" program<sup>3)</sup> is an interactive program which subtracts the background component from the total count of a photopeak. The input data are typed in after they were read on the MCA display

(4) "DAYS" program<sup>3)</sup> calculates the lapse of time in days or years following the preparation of radiation sources.

#### References

- 1) Yoshida, H., Kubo, K., Sakai, E.: Reactor Engineering Division Annual Report (April 1, 1978 - March 31, 1979), 5.16, pp.128-130, JAERI-M 8393 (September 1979).
- 2) Yoshida, H., Kubo, K.: Programming of Canberra Industries 8100/Quanta System - Program Development with "CLASS", JAERI-M 8694 (March 1980) (in Japanese).
- 3) Reference,<sup>2)</sup> 12, pp.66-74.

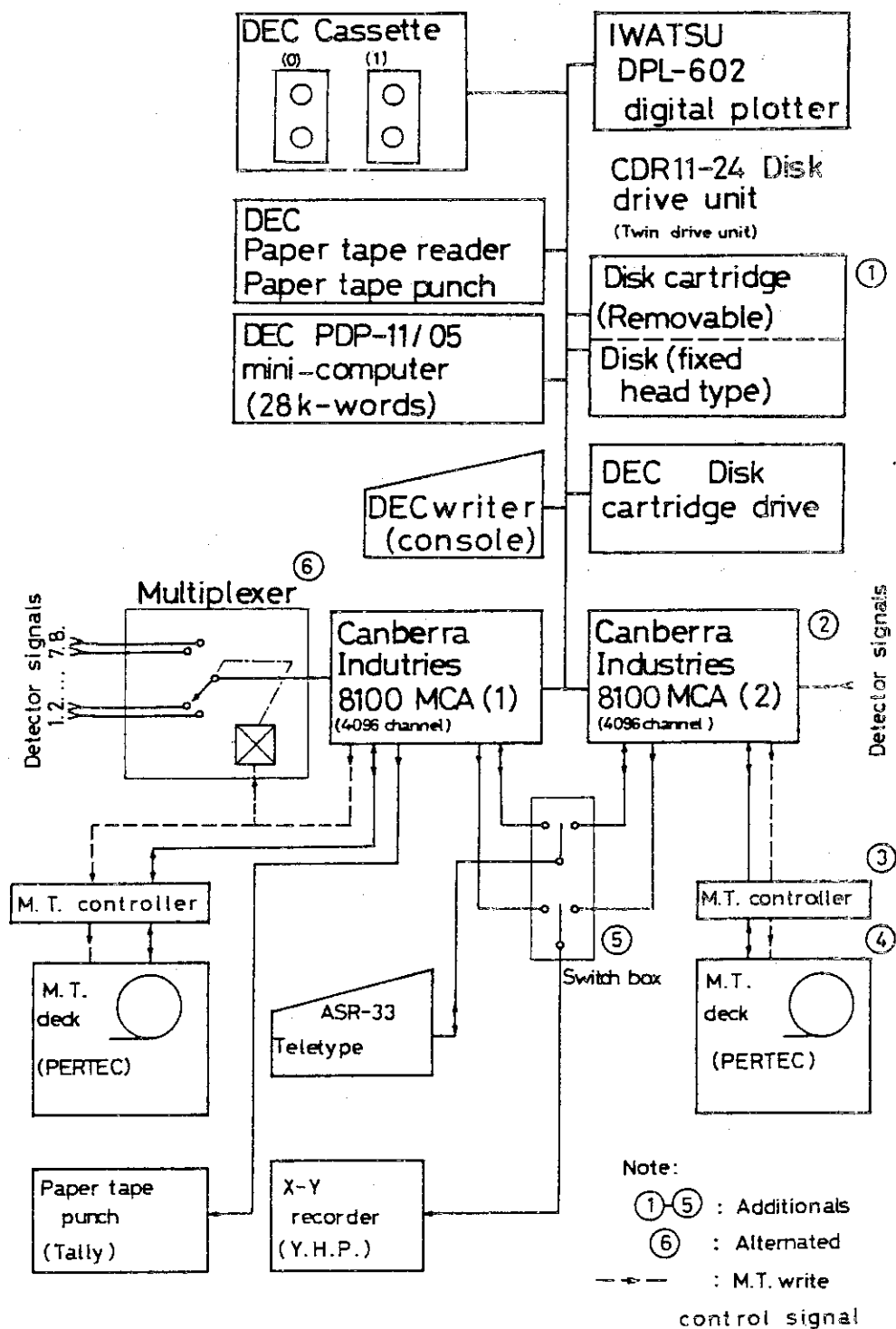


Fig. 5.13.1 Block diagram of Canberra Industries 8100/Quanta System and measurement system

## 6. Reactor Control and Diagnosis

### 6.1 Preliminary Study on Detection of Sodium Boiling in LMFBFR

Y. Shinohara and J. Shimazaki

Methods of sodium boiling detection were studied in order to develop a subsystem of core surveillance system for LMFBFRs.

First, an extensive literature survey was made on the theoretical and experimental works which have been done so far in various countries in relation to sodium boiling. The most sensitive method of sodium boiling detection seems to be that based on the correlation between neutronic and acoustic signals, although this method is not applicable if the reactivity coefficient of sodium void is practically zero.

In order to check the sensitivity of the sodium boiling detection method based on the correlation method, a simulation study was performed using a hybrid computer. In this study, the dynamics model of a fast reactor was set up on the analog part of the hybrid computer. The noise signal which simulates the reactivity fluctuation due to sodium boiling and the additive noise signal which simulates the measurement noise were applied to the reactor simulator. A reactivity estimator based on the Kalman-Bucy filtering technique was also setup on the analog part, while computation of correlation function, power spectral density function and coherence function was performed by the digital part of the computer. By varying the noise signal amplitudes and spectral patterns, detectable average void volume was determined.

From the simulation study, it was concluded that the sodium boiling detection method based on the cross-correlation between neutronic and acoustic signals is not always effective in realistic case of the LMFBFR considered and that in some cases it may be improved by taking other cross-correlations. A plan of experimental work was also proposed.

## 6.2 Reactivity Anomaly Diagnosis for Fast Experimental Reactor

J. Shimazaki, Y. Fujii and Y. Shinohara

A study was made on the reactivity anomaly diagnosis scheme for the Fast Experimental Reactor "JOYO", based on the balance calculation of net reactivity and feedback reactivity components which are estimated by applying the optimal estimation theory to the reactor dynamic model. An algorithm for estimation of reactivity components and computer program has been developed. Fundamental ideas of reactivity anomaly diagnosis were already reported.<sup>1)</sup>

Computer program for analyzing the reactivity anomaly diagnosis consists of three subprograms which are used for observability/stability test, Kalman-Bucy type estimator design, and dynamic simulation with/without estimators. The dynamic model accepted in this program is the nodal state space equations up to 50 dimensions. The model for estimation of reactivity components is made to be the coarse mesh nodal model of reactor core heat transfer. Using the computer program, reactivity anomaly diagnosis system can be evaluated to the different noise in reactor core. First assuming plant and measurement white noise with a given covariance, dynamic simulation is executed to get the measurement simulation data. And two estimators are designed for the estimation of net reactivity and feedback reactivity components. Finally the reactivity anomaly diagnosis system is constructed from two estimators and is tested through dynamic simulation using measurement simulation data.

One of the simulation results is shown in Fig. 6.2.1. This is the case of 2  $\beta$  external reactivity added to the reactor core. Neutron flux and coolant outlet temperature are measured with different Gaussian noise of 0.002 and 0.1 covariance each. Neutron flux is sufficiently filtered and the reactivity residual is the good estimation of 2  $\beta$  external reactivity disturbance with the accuracy of  $\pm 0.1 \beta$  after 5 sec from the starting time of estimation.

### Reference

- 1) Shimazaki J., Shinohara Y.: "Reactivity Anomaly Detection via an Optimal Estimation of Reactivity Feedback Components", Anomaly Detection and Prediction Techniques Symp. of SICE, Tokyo (1978).

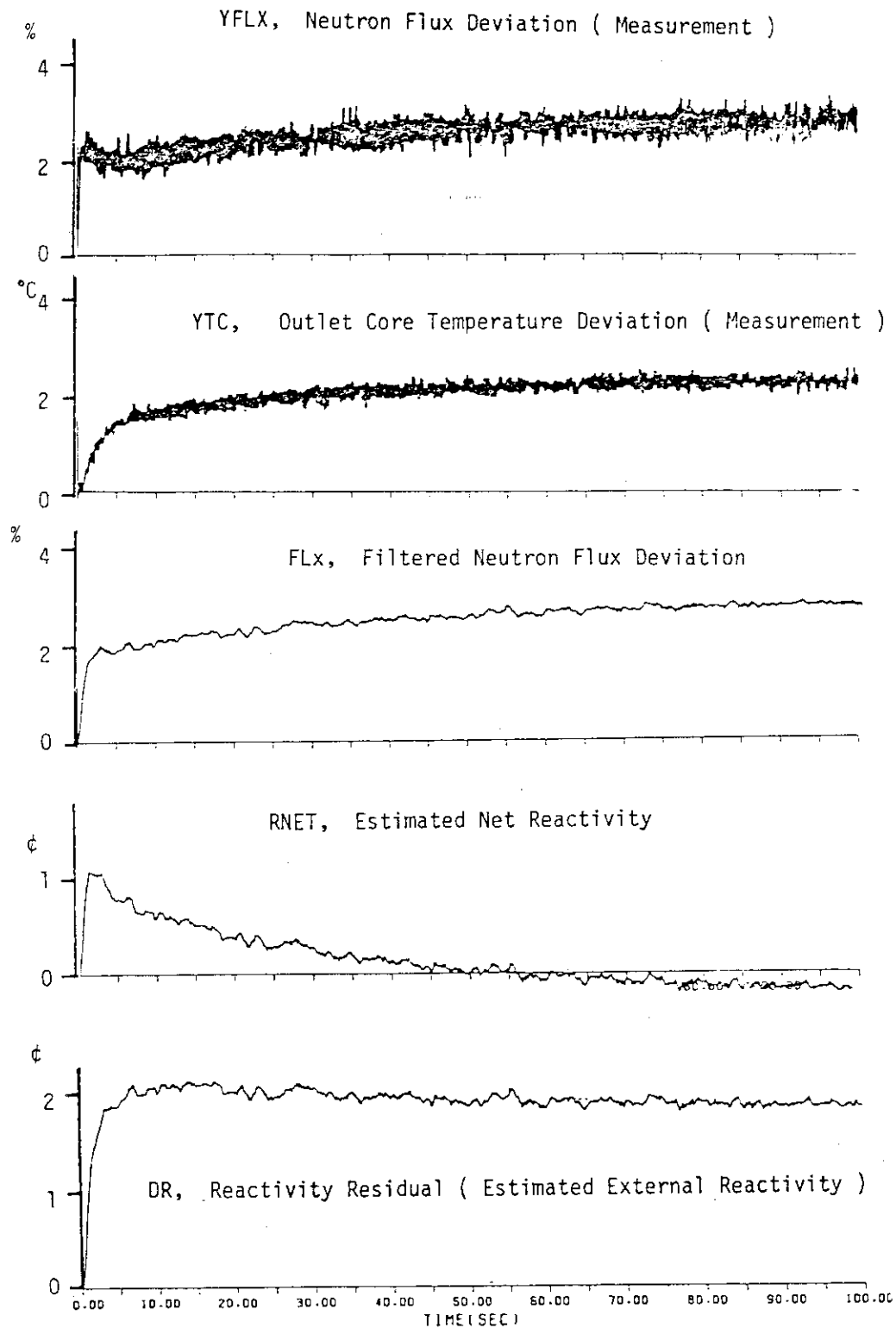


Fig. 6.2.1 Computer simulation result of reactivity anomaly diagnosis of Fast Experimental Reactor "JOYO" when 2  $\rho$  external reactivity input



### 6.3 Reactor Water Level Estimation of a BWR Plant by the Use of Kalman-Bucy Filtering Technique

J. Shimazaki and M. Yokobayashi

A problem of water level estimation occurs when meter level and real water level show the different behavior specially in the case of large core flow change or pressure decrease. The fundamental estimator design of reactor water level in a BWR plant and some of the computer simulation results are shown here.

The water level meters of JPDR-II plant consist of two types of level meter. One is Yarway-type meter for the reactor safety system and the other is Bailey-type meter for normal reactor operation. In the steady state operation, the difference of Bailey-type meter level and real water level is small and approximately up to 5 cm because of the effect of carryunder quality. However the difference grows large when recirculation pump trip or large steam flow change occurs. The real water level is one of state variables to be continually monitoring for the safety of reactor core.

A state variable dynamic model of reactor core is useful to estimate internal core state variables. The dynamic model of water level estimation was made to be eight dimensional state variable and seven input variable from fifteen dimensional state variable model already developed.<sup>1)</sup> These variables are shown in Fig. 6.3.1 where reactor thermal power  $Q_C$ , core average void fraction  $R_g$ , core outlet quality  $X_C$ , riser average void fraction  $R_{gR}$ , riser outlet quality  $X_R$ , reactor pressure  $P$ , meter water level  $H_m$  and real water level  $H_R$  as eight state variables, and neutron flux  $N$ , turbine steam flow  $W_{ST}$ , dump condenser steam flow  $W_{ID}$ , recirculation flow  $W_O$  and core inlet temperature  $T_{in}$  as seven input variables.

The water level estimator is designed applying Kalman-Bucy filtering technique, where measurement variables are pressure and meter level and the covariance of state and measurement variables is assumed 1 ~ 2 % of normal steady state values. The estimator had the good characteristics of stability and convergence from computer simulation results. In the case of 5 % core flow up, estimated real water level was followed to the level calculated by JPDR-II digital dynamic code (JPDYN-IV)<sup>2)</sup> and was consistent approximately after 15 sec from the starting time of estimation.

One of computer simulation results is shown in Fig. 6.3.2 when turbine bypass valve full open. The figure shows that the water level estimation using the estimator designed above is the good consistence of the results from JPDYN-IV code calculation and that the difference between meter level and real water level is approximately 20 cm during the transient.

It concludes that the water level estimator with small dimension of state variable is useful for the estimation of real water level. Presently it is continued to apply this type of estimator to the practical data obtained from JPDR-II dynamic experiments.

#### References

- 1) Shimazaki J., Yokobayashi M.: "Control and State-Estimation Problems for JPDR-II Plant (I), Discussions of Dynamic Model", 1978 Fall Meeting of Atomic Energy Society of Japan, C39.
- 2) Yokobayashi M., et al.: "JPDYN-IV: A Computer Code for JPDR-II Dynamics Analysis", JAERI-M 8010 (1978).

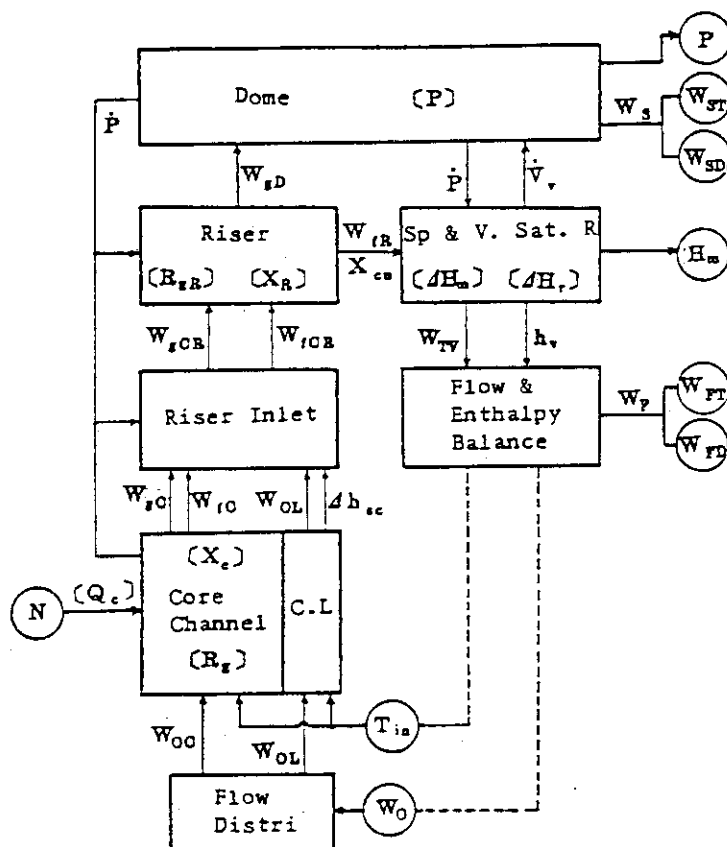


Fig. 6.3.1 State and external input variables of the water level estimator

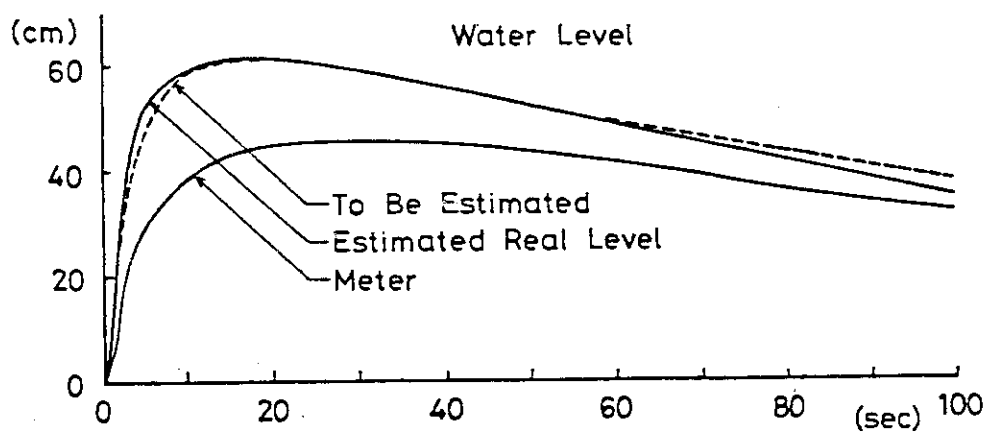


Fig. 6.3.2 Dynamic simulation of the water level estimator in the case of turbine bypass valve full open

## 6.4 Survey of Existing Robot Technologies for Nuclear Application

Y. Shinohara and H. Usui

As a preliminary work for developing robot technology for reactor application, a survey of the existing robot technologies applied in nuclear field were continued.

The types of the robots which have been developed so far in various countries can be divided into two categories; namely, the general purpose robots for surveillance and maintenance and the special purpose robots for in-service inspection. The former is an advanced type of classical teleoperator and the latter is that of flexible automation. During the last decade, much effort has been made in France and Germany in developing general purpose robots while various special purpose robots have been developed in USA and Japan as well as in Europe. However, the present state of art of robot technology in the nuclear field is very primitive. From the survey of the existing technologies, it was concluded that the major problems to be considered in developing the work robots for nuclear reactor application are the developments of 1) special vehicles of flexible mobility, 2) compact manipulators with versatile hands, 3) control language that can accept fuzzy commands, 4) measures of easy decontamination of the robot itself, and 5) control systems of the robot that are easy to operate. The control system must include highly developed intelligence systems such as pattern recognition system. The development of radiation resistant sensors is also important if the robot is to be used in high level radiation environment.

The conceptual design of a work robot for dismantling nuclear reactors is now envisaged as the first stage in the development of work robots for nuclear reactor application.

### References

- 1) Shinohara Y.: "Needs of Robot Technology in Nuclear Installations", Robot, No.23, 34 (1979)
- 2) Shinohara Y.: "Status of Robots for Nuclear Application", Oyokikaikogaku, No.9, 116 (1979)

## 7. Fusion Reactor Technology

### 7.1 Construction of Accelerator System for Fusion Neutronics Source (FNS)

#### ----- Factory Test -----

T. Nakamura, H. Maekawa, J. Kusano, Y. Oyama, Y. Ikeda and  
C. Kutsukake

The accelerator for Fusion Neutronics Source (FNS) had finished installation and adjustment at General Ionex Corporation factory after considerable delay in schedule due to the design modification of telemetry system, motor alternator bearing failure, 90 degree analyzing magnets reshaping etc. The outline of FNS was described in the annual reports of last two years (JAERI-M 7844 and 8393).

The factory demonstration test was carried out from Feb. 15 to Mar.  
1. The procedures and results are as follows.

#### (1) System inspection

- A. Vacuum System - Recorded base pressure readings in each vacuum section and confirmed that all were below the specified value.
- B. HV Power Supply - Confirmed the stable running at 400 kV throughout the test period.
- C. Beamline - Identified the components and tested the function in the case of necessity.
- D. Rotating Target Assembly - Observed rotation and water flow and measured vacuum of the section with/without rotation.

#### (2) DC beam test with High Current Ion Source

- A. Ion Source Characteristics - Measured maximum obtainable beam current (32 mA of  $H_1^+$ ) and recorded the source parameters, also measured atomic ratio ( $H^+$ :74.1%,  $H_2^+$ :17.0%,  $H_3^+$ :8.9%) by using Faraday Cup #1 (FC 1).
- B. Beam Test on 0° Beamline - Tuned beam through 0° transport system and measured maximum available current at the end of the beamline (FC 5: 14.5 mA by current meter and 17.2 mA by reference calorimetric means).
- C. Beam test on 80° Beamline - Led beam into 80° transport line and measured reference data on beam transmission (FC 1: 7.0 mA, FC 2:

4.8 mA, FC 3: 2.8 mA), beam current being restricted to protect the buncher electrodes.

(3) DC beam test with Low Current Ion Source

- A. Ion Source Characteristics - Measured maximum obtainable beam current (5.2 mA of  $H_1^+$ ) and recorded the source parameters, also measured atomic ratio ( $H_1^+$ : 66.8%,  $H_2^+$ : 27.6%,  $H_3^+$ : 5.6%) by FC 0.
- B. Beam Test on 80° Beamline - Tuned beam through 80° transport system and measured maximum available current at the end of the beamline (FC 3: 2.8 mA).

(4) Pulsed beam test

- A. Pulse Control Modules - Observed output waveforms of diverter, sweeper, post acceleration deflector, buncher and arc pulser control modules using an oscilloscope.
- B. Sweep Mode Pulse Operation - Tuned and observed beam form at Fast Faraday Cup (FFC) on the 80° transport end for pulse widths of 20 ns, 500 ns and 8  $\mu$ s.
- C. Bunched Mode Pulse Operation - Observed beam form of FFC with/without buncher voltage and measured pulse widths and peak currents (unbunched: 25 ns, bunched:  $\sim$ 2 ns) with  $H_1^+$  ion of reduced energy.

The results did not always satisfy the values described in the specifications, mainly because beam axis alignment was insufficient to get best optics. The careful examination and additional tests indicated that the machine had the enough potentiality to achieve full specifications, when it should be installed in the FNS building that had better conditions for alignment. So it was concluded that further refinements would be done at the installation in JAERI. Soon after the test the accelerator was disassembled and packaged for transportation.

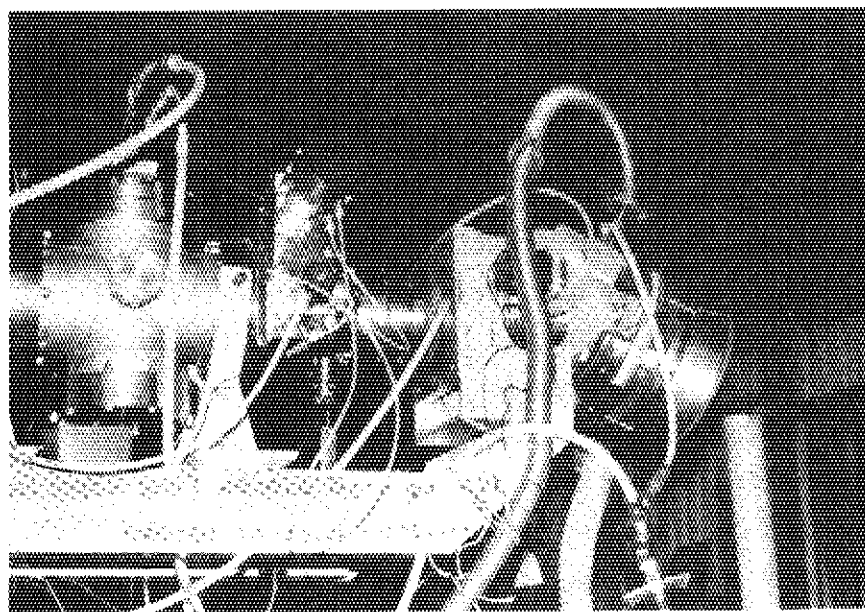


Photo. 7.1.2 End of 80° Beamline.  
They measured the shape of pulse beam by  
an oscilloscope.

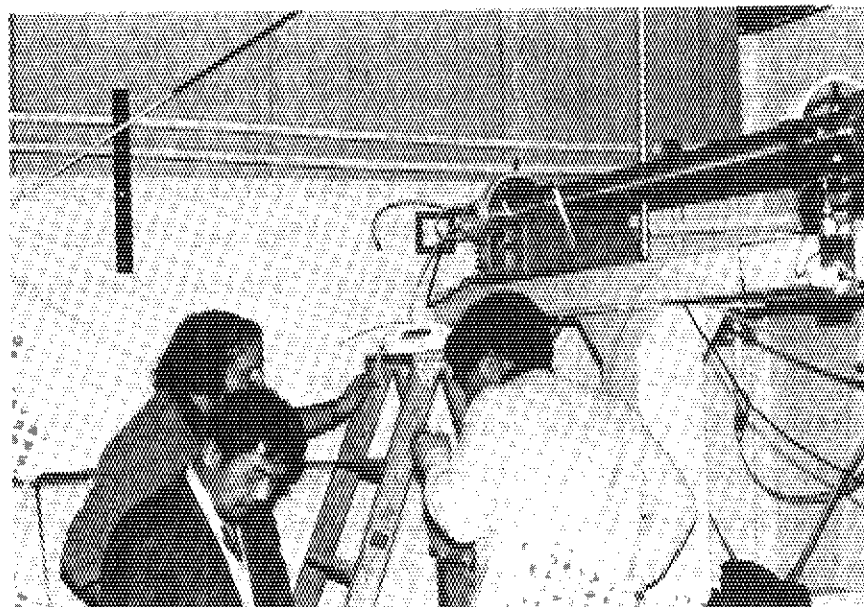


Photo. 7.1.1 End of 0° Beamline.  
Water catcher was removed from the rotating target.

## 7.2 Effect of Hydrogen and Carbon in Lithium Oxide Blocks on Data of Integral Experiments

H. Maekawa and T. Nakamura

We are now planning to prepare 1.5 ton of  $\text{Li}_2\text{O}$  blocks for the benchmark experiment of fusion blanket. Lithium oxide is proposed by JAERI's design group as a blanket material.<sup>1)</sup>

As  $\text{Li}_2\text{O}$  is chemically active material, it is very difficult to keep low impurity, especially  $\text{LiOH}$  and  $\text{Li}_2\text{CO}_3$ , during the manufacturing of  $\text{Li}_2\text{O}$  blocks. Neutron spectrum in  $\text{Li}_2\text{O}$  assembly is affected greatly by the existence of hydrogen and carbon because of their light mass. If we can loosen restrictions of impurity in  $\text{Li}_2\text{O}$  blocks from experimental point of view, there is a room for reducing the cost of blocks.

Effect of H and C atoms in  $\text{Li}_2\text{O}$  has been estimated by a calculated fission-rate that is good measure for the fusion neutronics. The model adopted for the calculation of a  $\text{Li}_2\text{O}$  assembly is shown in Fig. 7.2.1. This model used for a reference assembly was chosen on the basis of previous experiments.<sup>2),3)</sup> The nuclide densities of reference assembly are given in Table 7.2.1. The neutron fluxes in the assembly were calculated by ANISN code with  $\text{P}_5\text{-S}_{64}$  approximation using a cross section set of GICX40V4<sup>4)</sup>. An isotropic D-T neutron source is assumed to be uniformly distributed in the central sphere of 0.5 cm radius. In addition to the reference assembly, four types of assembly were calculated. They were named as H-1, H-5, C-1 and C-5. For example, H-1 was an assembly adding H atoms at the rate of 1 % of Li atoms to the reference assembly. The fission-rate distributions of  $^{232}\text{Th}$ ,  $^{238}\text{U}$ ,  $^{237}\text{Np}$  and  $^{235}\text{U}$  in the five assemblies were calculated from the spectra. Typical fission-rate change is shown in Fig. 7.2.2.

Even if the quantity of hydrogen is very small in  $\text{Li}_2\text{O}$ , the neutron spectrum shifts to be soft and reaction rates of  $^{235}\text{U}$  and  $^{238}\text{U}$  increases and decreases, respectively. This makes large uncertainty in the measurement of tritium breeding-ratio. It can be concluded that the fraction of hydrogen and carbon in  $\text{Li}_2\text{O}$  should be kept less than 0.5 % and 3 % of Li atoms, respectively, to achieve the reaction-rate change within the order of experimental error, i.e., about 6 %.



## References

- 1) Sako K., et al.: Conceptual design of a gas-cooled tokamak reactor, JAERI-M 5502, (1973).
- 2) Maekawa H., Seki Y.: J. Nucl. Sci. Technol., 14 [2], 97 (1977).
- 3) Maekawa H., et al.: ibid, 16 [5], 377 (1979).
- 4) Seki Y., Iida H.: Coupled 42-group neutron and 21-group gamma ray cross section sets for fusion reactor calculations, JAERI-M 8818 (1980).

Table 7.2.1 Nuclide densities of reference assembly

Nuclide	Nuclide density ( $10^{24}$ atoms/cm <sup>3</sup> )	
	Void	Li <sub>2</sub> O
<sup>6</sup> Li		$3.3547 \times 10^{-3}$
<sup>7</sup> Li		$4.1857 \times 10^{-2}$
O		$2.2606 \times 10^{-2}$
Cr	$1.827 \times 10^{-3}$	$2.011 \times 10^{-3}$
Ni	$7.964 \times 10^{-4}$	$8.781 \times 10^{-4}$
Fe	$6.652 \times 10^{-3}$	$7.346 \times 10^{-3}$

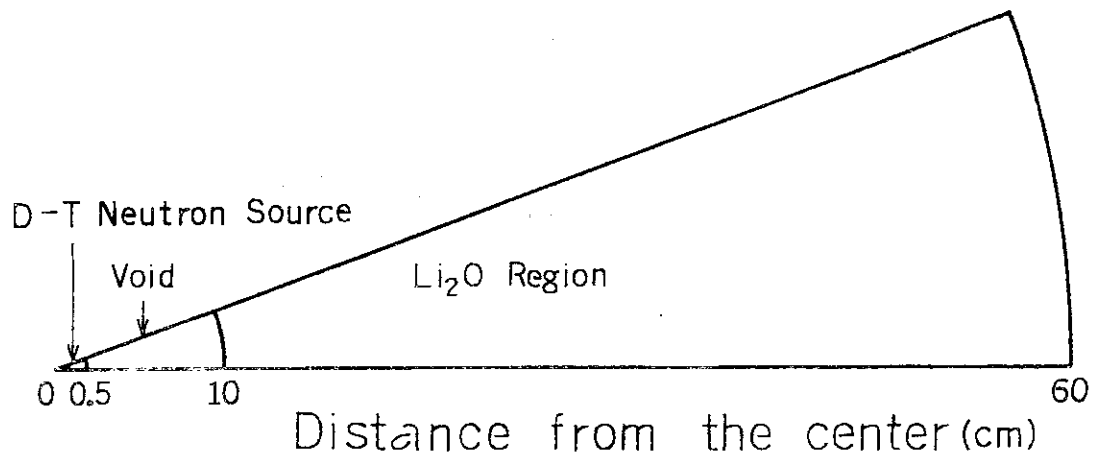
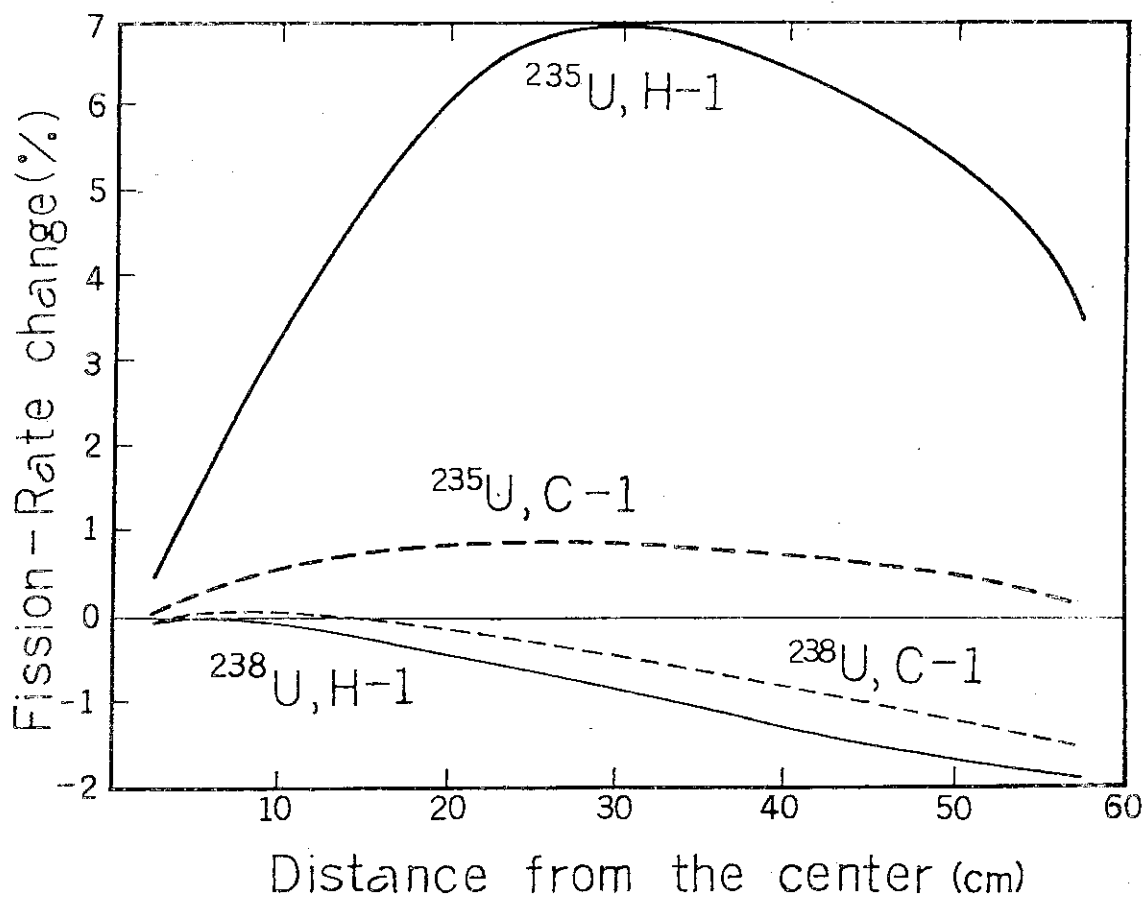


Fig. 7.2.1 Calculational model of reference assembly

Fig. 7.2.2 Fission-rate change of  $^{235}\text{U}$  and  $^{238}\text{U}$  in  $\text{Li}_2\text{O}$  assembly due to the existence of hydrogen and carbon

### 7.3 Preliminary Hot-Test on Tritium Scrubber for FNS

S. Tanaka, Y. Oyama, C. Kutsukake, Y. Ikeda, H. Maekawa, J. Kusano and T. Nakamura

In Fusion Neutronics Source (FNS), tritium targets of about 20-1800 Ci are used to yield a high intensity 14 MeV neutron due to D-T reaction. The tritium inventory of each target released into the accelerator vacuum system during the operation of FNS is estimated as shown in Table 7.3.1. The Tritium Adsorption Plant (TAP) having a Tritium Removal System (TRS) in FNS is accommodated to collect the exhaust air and to remove tritium from the air before it is vented to the atmosphere. Figure 7.3.1 shows the flow of TAP.

Following items on the performance of the TRS are evaluated by experiments, prior to the start of FNS operation.

- 1) The decontamination factor (DF) for  $H_2$  and  $D_2$  is larger than that of the design.
- 2) The performance of TRS is sufficient for tritium scrubbing of the exhaust air shown in Table 7.3.1.
- 3) The tritium scrubbing rate of TRS satisfy the designed performance.
- 4) Hydrogen swamping gives a good effect for scrubbing low concentration tritium.

Experimental results have indicated that the DF for  $H_2$  and  $D_2$  was larger than the designed value of  $10^3$ , and the tritium concentration was reduced to the low level of about  $2 \times 10^{-4}$  -  $5 \times 10^{-4}$  ppm without any hydrogen swamping. On the other hand, the effect of hydrogen swamping was not observed explicitly, since the tritium concentration was too low to be measured by the tritium monitor of TRS during the hydrogen swamping. Figure 7.3.2 shows the typical result of tritium concentration as a function of time. The observed scrubbing rate deviated from the design value as tritium concentration decreased. This is presumed that the rate was influenced by the slow release of adsorbed tritium gas on the inner wall of TRS.

The present experiments demonstrated that the performances of TRS are satisfactory to remove the tritium in the vacuum exhaust of FNS. However, further experiments are necessary to estimate quantitatively

the influence due to the adsorption and release of tritium on inner wall to the tritium scrubbing rate. Furthermore, prescriptions against tritium contamination of monitor are needed for measuring accurately the tritium concentration over the wide range, since a difficulty is encountered in monitoring the tritium of low concentration by the contamination.

Table 7.3.1  $^3\text{T}$  release from FNS during a operation  
(estimated value)

Target (Ci/disk)	Time of target usage (hr/run)	Number of usage per year (run/year)	$^3\text{T}$ release (Ci/run)	SORBAC pump adsorption (Ci/run)	Vacuum exhaust (Ci/run)
1800*	100	4	270	216	54
350**	100	2	53	35	18
20**	4-8	150	0.12-0.24	0.08-0.16	0.04-0.08

\* usage at 2nd target room

\*\* usage at 1st target room

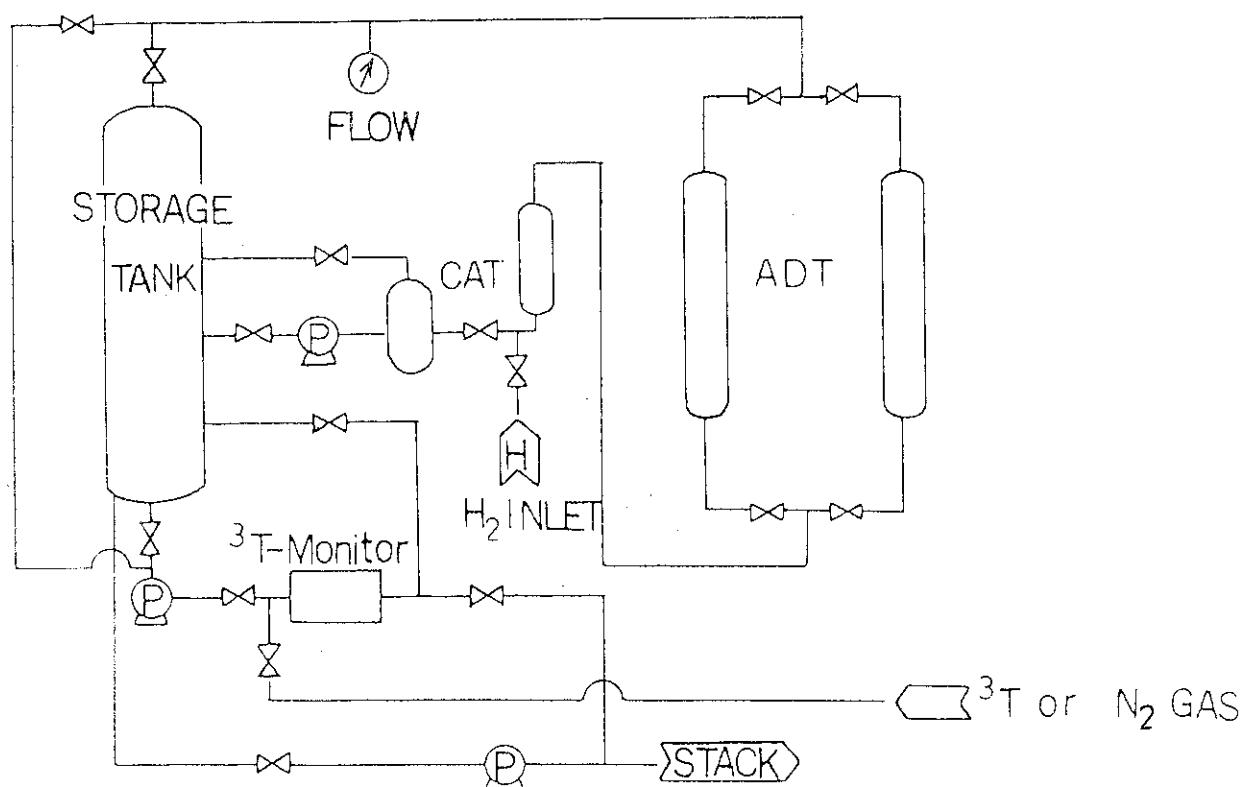


Fig. 7.3.1 The flow of TAP

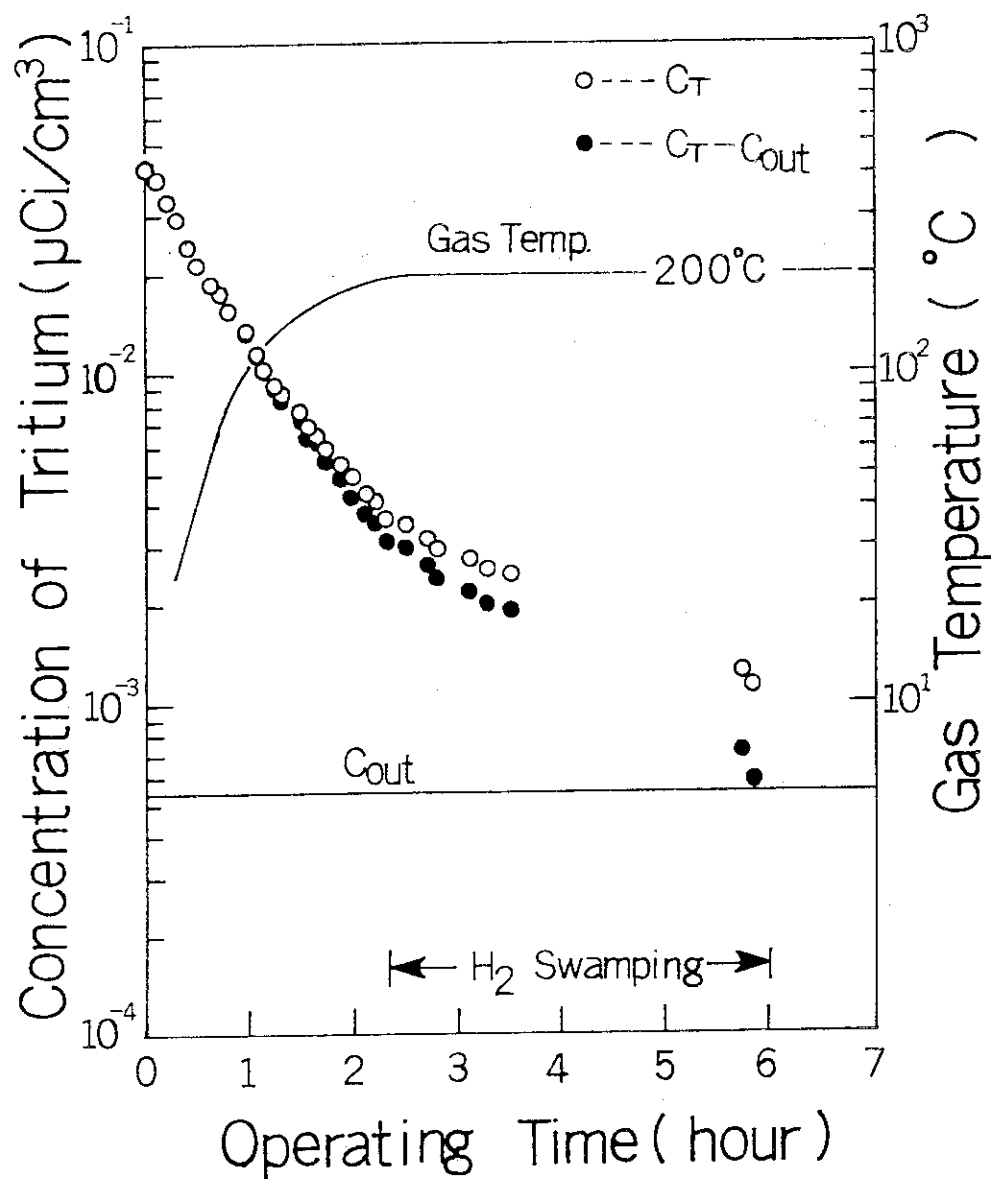


Fig. 7.3.2 The typical result of experiments ( $C_T$  and  $C_{out}$  is concentration of Tritium in storage tank and ADT exhaust gas respectively)

#### 7.4 Cross Section Sensitivity Analysis of $^{235}\text{U}$ and $^{238}\text{U}$ Fission Rates in a Graphite Reflected Lithium Oxide Assembly

Y. Oyama, Y. Seki, H. Maekawa and T. Nakamura

In the conceptional design of JAERI's experimental fusion reactor JXFR, lithium oxide ( $\text{Li}_2\text{O}$ ) is adopted for a solid state blanket breeding materials. In previous work, the absolute fission-rate distribution of  $^{235}\text{U}$ ,  $^{238}\text{U}$ ,  $^{232}\text{Th}$  and  $^{237}\text{Np}$  by micro-fission chambers were obtained in an assembly which simulated a "Graphite Reflected Lithium Oxide Blanket".<sup>1)</sup> In order to get clearer understanding in the interpretation of the results of the measurements and calculations, the sensitivity calculation of  $^{235}\text{U}$  and  $^{238}\text{U}$  fission-rates on each constituent cross section at each measured position were performed by the computer code SWANLAKE.<sup>2)</sup>

The cross section set for the present analysis is processed from ENDF/B-IV data using NJOY code. The calculational model of the  $\text{Li}_2\text{O}$ -C assembly is assumed to be spherical symmetry, uniform composition in each region with a isotropic D-T neutron source (Fig. 7.4.1). The forward and adjoint angular fluxes in the assembly are calculated by the ANISN code with the  $P_5$ - $S_{64}$  approximation. These angular fluxes are applied to the SWANLAKE code based on a perturbation theory.

The results of sensitivity calculation are examined through a integrated sensitivity with respect to energy and a sensitivity profile as a function of energy (Fig. 7.4.2). The followings are obtained: (1) The discrepancy of the C/E values, which are the ratios of calculational estimates to the experimental data, seems to be partly attributed to the uncertainty of  $^{12}\text{C}$  cross section data. (2) The sensitivity analysis gives the condition of assembly which is required by the experiment. The results suggest to make a measurement in an assembly which gives a large sensitivity to the only interesting nuclide.

#### References

- 1) Maekawa H., et al.: J. Nucl. Sci. Technol., 16 [5], 377 (1979).
- 2) Oyama Y., et al.: "Cross Section Sensitivity Analysis of  $^{235}\text{U}$  and  $^{238}\text{U}$  Fission rates in a Graphite Reflected Lithium Oxide Assembly", JAERI-M 8870 (1980) [in Japanese].

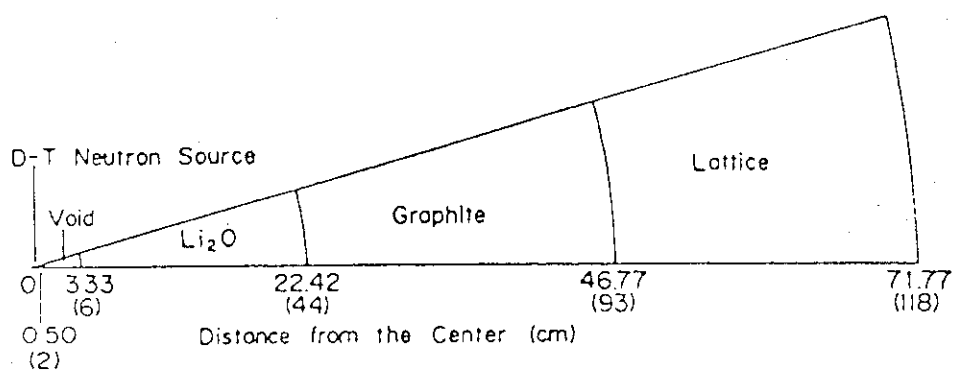


Fig. 7.4.1 Calculational Model of  $\text{Li}_2\text{O}$ -C assembly  
(number in parentheses mean the mesh  
number of boundary in the calculation)

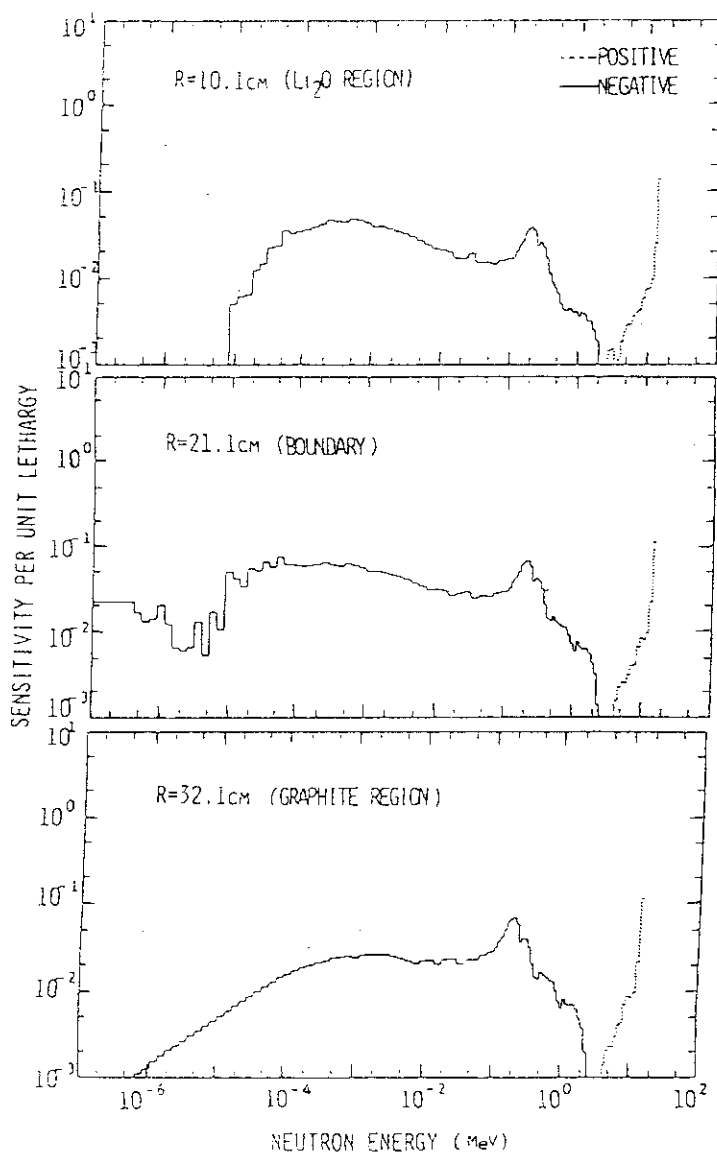


Fig. 7.4.2 Example of the results of sensitivity calculations  
(sensitivity profile of  $^{235}\text{U}$  fission rate for  $^6\text{Li}$ )

## 7.5 Development of Thin Germanium Film Bolometers for Plasma Radiation Loss Measurement

M. Katagiri and M. Maeno

The reduction of the radiation loss power from the plasma is one of the important problems in tokamak research. The radiation loss measurement requires a bolometer with a high sensitivity, a small response time and a well-defined heat capacity. Formerly, infrared bolometers were employed in this measurements. These bolometers had a good sensitivity, but the response time was large and the heat capacity was not well defined. Therefore, a thin germanium film bolometer which improved these defects was developed. And, this bolometer was employed to measure the radiation loss in JFT-2 tokamak.

The schematic structure of a new bolometer is shown in Fig. 7.5.1. A backing metal is a thin stainless steel plate 28 mm in diameter and 50  $\mu$ m in thickness. Silicon monoxide is deposited on the stainless steel as an electric insulator in vacuum ( $\sim 10^{-6}$  mmHg). Then, germanium is deposited on it as a thermistor element in high vacuum ( $\sim 10^{-7}$  mmHg), keeping the temperature of the backing metal at 300°C. After that, aluminium is deposited so as to be patterned as shown in Fig. 7.5.1. The resistance between both aluminium electrodes is 10 k $\Omega$   $\sim$  20 k $\Omega$  at room temperature.

Figure 7.5.2 shows calibration curves of a typical thin germanium film bolometer. Figure 7.5.2(a) shows resistance-temperature relation of the germanium film. Figure 7.5.2(b) shows the dependence of the coefficient on temperature. The temperature coefficient of the bolometer is 2.1 %/°C at room temperature. The response time and the cooling time constant which were measured by use of a Xenon lamp were 0.3 msec and 2.2 sec. The response time is much shorter than discharge duration of 0.1 sec  $\sim$  0.2 sec in JFT-2. The cooling time constant is satisfactorily large compared to the discharge duration. So, the incident radiation loss power density  $q_r$  at the bolometer can be calculated from a simple heat balance equation:

$$q_r = \gamma c d (dT/dt)$$

where  $\gamma$ ,  $c$  and  $d$  are the density, the specific heat capacity, and the thickness of the stainless steel, respectively.

The bolometer was so arranged in JFT-2 tokamak that its surface coincided with a liner surface. The bolometer was carefully shielded from the light of the plasma. And, one electrode of the bolometer was connected to the liner of JFT-2 for decreasing the electrical induction to it during discharge.



Figure 7.5.3 shows typical waveforms of discharge. The radiation loss measurement was made under the conditions: toroidal magnetic field  $B_t = 16$  kG; plasma current  $I_p = 100$  kA; and the mean line of sight density  $n_e = 10^{13} \text{ cm}^{-3}$ . The integral waveform shows total incident radiation loss and the differential waveform (differential time constant = 10 msec) shows the incident radiation loss power density  $q_r$ . The maximum value of  $q_r$  is about  $2 \text{ W/cm}^2$  at 13 msec and the  $q_r$  during constant current phase is  $0.5 \sim 1.0 \text{ W/cm}^2$ .

Consequently, it is revealed that the thin germanium film bolometer is capable of measuring the incident radiation loss power density of  $0.5 \text{ W/cm}^2$  in the high S/N ratio of 40 dB.

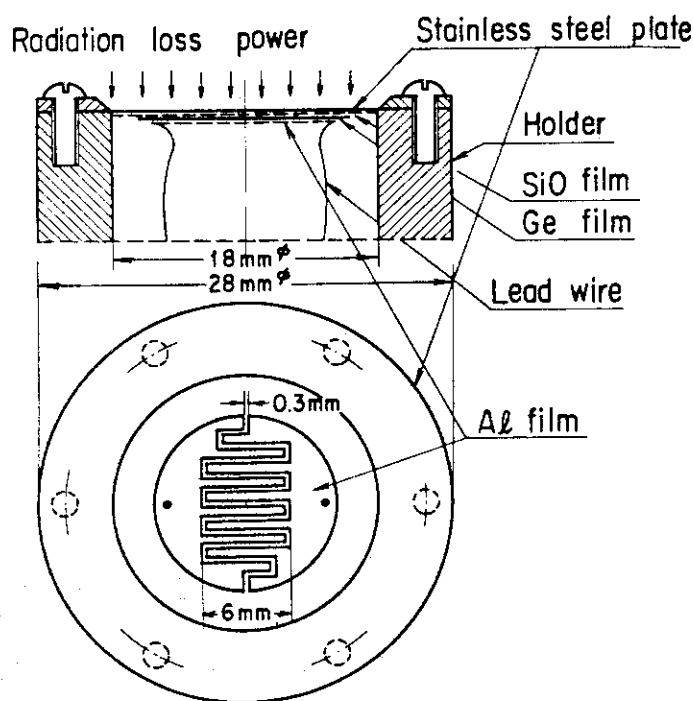


Fig. 7.5.1 The schematic structure of a thin germanium film bolometer

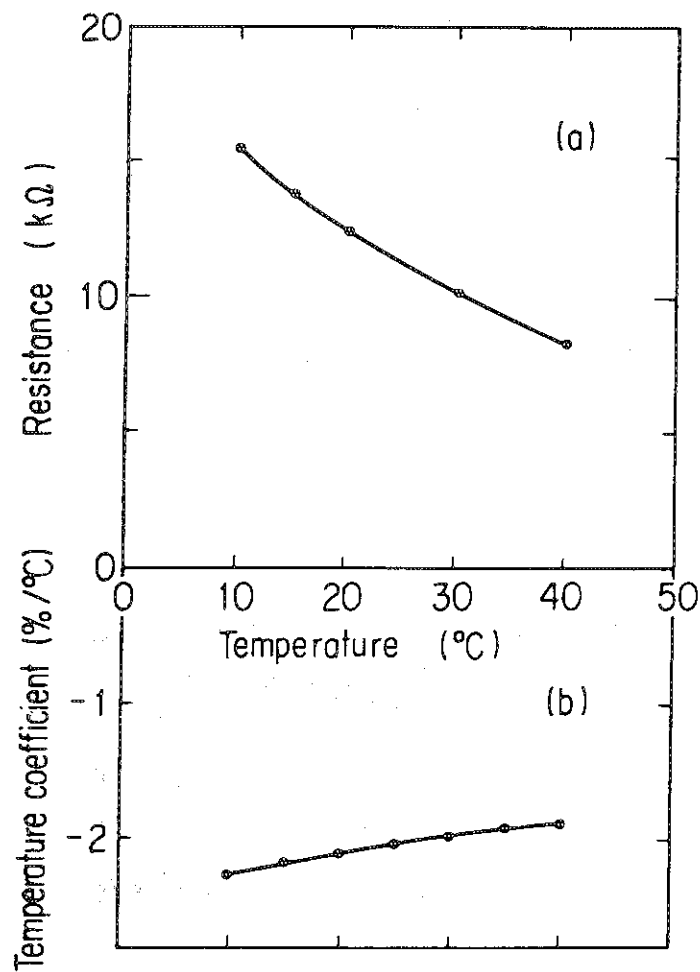


Fig. 7.5.2 Resistance-temperature relation of the germanium film (a); and temperature coefficient of the resistance (b)

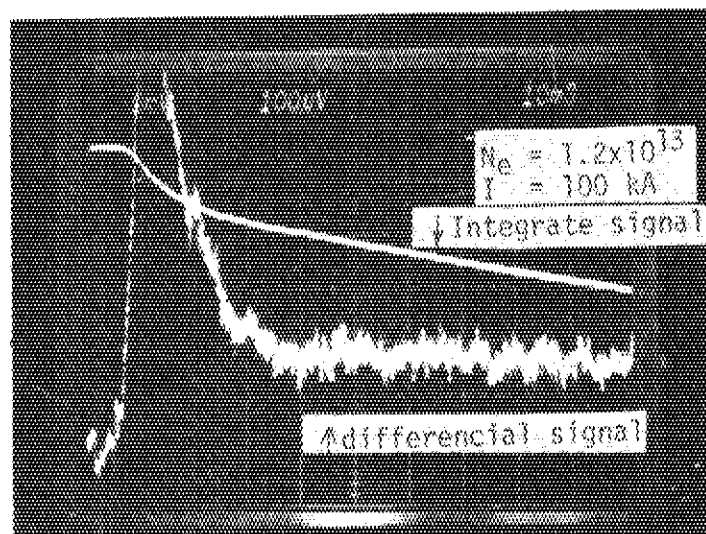


Fig. 7.5.3 Integral waveform and differential waveform of the bolometer signal measured in JFT-2 tokamak

## 8. Activities of the Committees

### 8.1 Activities Related to the NEA Committee on Reactor Physics

J. Hirota

During this one year period, the Committee on Reactor Physics continued to make efforts for the objectives, having the connection with the NEA Committee on Reactor Physics (NEACRP). The Committee made a significant contribution to the 22nd meeting of the NEACRP which was held in October. For the 3rd Specialists' Meeting on Reactor Noise (SMORN-III) to be held in 1981 in Tokyo, the Preparatory Committee has been organized under the Committee to prepare the proposals for the Meeting and the benchmark test.

The Committee held the 34th meeting in May: The process of the NEA Data Bank ANL Seminar, IAEA/ OECD NEA International Symposium on Fast Reactor Physics and SMORN-III, and the renewal of the mandate of the NEACRP were reported and discussed. Then, three papers, "Detail Analyses of a BWR Core Performance by Leakage Iterative Method," "POLESTAR-2F/3F Code for Power Mapping and Refuelling Analysis of Operating HWR-Fugen" and "Effective Use of Operating Data for 3 - Dimensional BWR Core Simulator" were reported and discussed for the presentation at the NEACRP Specialists' Meeting on Calculation of 3 - Dimensional Rating Distributions in Operating Reactors in November. It was recommended that these papers should be discussed in detail at the Subcommittee on Reactor System Analysis before the Meeting.

The Committee held the 35th meeting in August, for making the preparation to the 22nd meeting of the NEACRP: The research activities in Japan during the period from November 1978 to September 1979 were discussed to prepare the review-paper<sup>1)</sup>. The items cover fast and thermal reactor physics, fusion and shielding studies. For contributions from Japan to the topics of the meeting, three papers and one short note were reported and discussed, which were as follows; "Determination of Pu Accumulated in Irradiated Fuels by Non-Destructive Isotope Correlation Technique" , "Some Correlations between Isotopes of Nd, U, Pu and Burn-up Parameters for the FBR Irradiated Fuel", "Evaluation of Criticality Computation Using the Monte Carlo Code KENO-4 with a New Multi-Group Nuclear Constants Library and "Comments on the Draft Proceedings of the NEACRP/IAEA Specialists'

Meeting on the International Comparison Calculation of a Large Sodium-Cooled Fast Breeder Reactor", In addition, comments on the draft, "Summary of NEACRP Views on Actinide Production and Burn-up" , and a list of papers to be presented at the Specialists' Meeting on Calculation of 3 - Dimensional Rating Distributions in Operating Reactors were distributed. Proposals from Japan for the topics of the 23rd meeting of the NEACRP were also discussed.

#### Reference

- 1) Hirota J., Inoue T. : "Reactor Physics Activities in Japan - November 1978 to September 1979", NEACRP-L-231 (Japan)

## 8.2 Activities of the Subcommittees on Reactor Physics

J. Hirota

The Subcommittees on Reactor System Analysis, Fusion Reactor and Shielding held the meeting two times respectively during this one year period to discuss topics of relevance to the each field. The Subcommittee on Shielding has organized a new working group on sensitivity and uncertainty analysis in order to catch up with recent progress in Europe.

The Subcommittee on Reactor System Analysis held the 1st meeting in July: For contributions from Japan to the topics of the 22nd meeting of the NEACRP, papers related to isotopic correlations for fuel exposure history determination, criticality problems in storage and transportation in out-of-pile fuel, heterogeneous cores, including safety related FBR problems, and detailed review of conclusions from the LMFBR Benchmark were reported and discussed. The Subcommittee held the 2nd meeting in November: Three papers to be presented at the Specialists' Meeting on Calculation of 3 - Dimensional Rating Distributions in Operating Reactors were reported and discussed in detail. Then, a summary of the 22nd meeting of the NEACRP was reported which included a review of the present status of the heterogeneous core study. Papers contributed from other countries to the topics such as isotopic correlation techniques and criticality problems in out-of-pile fuel were reviewed and discussed.

The Subcommittee on Fusion Reactor held the 1st meeting in May: A summary of the Advisory Group Meeting on Nuclear Data for Fusion Reactor Technology organized by the IAEA and held in December 1978 was reported and discussed. The present status of fusion neutronics studies in the world and the shielding experiment and analysis at ORNL were also reported. Then, the future plan of the Subcommittee was discussed. The Subcommittee held the 2nd meeting in October: The fusion neutronics study at Karlsruhe Centre was reported which included the experiment and analysis on Lithium spherical system and a newly developed analytical method. Then, the construction status of FNS at JAERI and OKTAVIAN at Osaka University were reported and proposals of the benchmark experiment were discussed.

The Subcommittee on Shielding held the 7th meeting in June: Results of the benchmark calculation carried out in the last fiscal year were reported and discussed. Three benchmark problems of 3 - dimensional duct streaming were proposed for the calculation in this fiscal year and it was

decided to start the calculation by the working group. The Subcommittee held the 8th meeting in October: Results of the benchmark calculation in progress were reported and discussed. After a summary of the session related to shielding in the 22nd meeting of the NEACRP was reported, presented papers were reviewed and discussed, which were as follows; "An Appraisal of the NEA Collaborative Programme of Uncertainty Analysis and Benchmark Experiments" (NEACRP-L-241), "Preliminary Version of the EURLIB Variance - Covariance Matrices" (NEACRP-A-388), "A Simple Comparison of Adjusted Data Sets for Iron Based on Measurements in ASPIS and in the Case of Fast Reactor Criticals" (NEACRP-A-387) and "Uncertainty Analysis in a typical Sodium-Cooled Fast Reactor" (NEACRP-A-389). Taking these substantial progress in Europe into consideration, it was decided to organize a new working group on sensitivity and uncertainty analysis under the Subcommittee. This working group held the meeting two times by the end of March 1980 aiming at contributions to the NEACRP Specialists' Meeting on Nuclear Data and Benchmarks for Reactor Shielding to be held in October 1980.

### 8.3 Activities of the Japanese Preparatory Committee for SMORN-III

J. Hirota and Y. Shinohara

At the 21st Meeting of the NEACRP held in 1978, it was proposed to hold the Third Specialists Meeting on Reactor Noise (SMORN-III) in 1981 in Japan. In order to make necessary technical preparations for the Meeting, the Japanese Preparatory Committee for SMORN-III was then organised as one of its subcommittees. The members of the Committee consist of eleven representatives from universities, nuclear industries, Power Reactor and Nuclear Fuel Development Corporation and JAERI.

As one of the major topics to be discussed at SMORN-III, it has been proposed to make benchmark test of the reactor noise analysis methods. The objective of the benchmark test is to obtain useful informations for providing some bases of standardisation of reactor noise data by making comparison of the results of benchmark test obtained by various noise analysis methods. For this purpose it is proposed to distribute a common data recorded on a magnetic tape to the applicants. Both real reactor noise data and artificially synthesized data will be used for the test.

During the past one year period, the Committee held five meetings and mostly devoted itself for discussions of the benchmark test problem to be proposed as well as the major topics to be covered at SMORN-III. The proposed major topics cover mathematical and physical interpretation of at-power reactor noise, innovation of analysis methods and instrumentation, safety related application, and efforts for standardization of noise analysis techniques.

The Committee submitted the proposal for SMORN-III (NEACRP-A-384) to the 22nd meeting of the NEACRP held in October, proposing to hold SMORN-III in Tokyo in October 1981.

#### 8.4 Activities of the Committee on Study of Decommissioning of Nuclear Facilities

M. Kawano

General study meetings were held several times by JAERI specialists on the decommissioning of JPDR (Japan Power Demonstration Reactor), on the process of liquid wastes coming from fuel reprocessing, on the decommissioning of the fuel reprocessing facility of JAERI, Tokai, on the decommissioning plan of JRR-3 (Japan Research Reactor-3), on the result of AHCF decommissioning, on the financing problem of decommissioning of nuclear power plants and so on.

In October, Atomic Energy Commission of Japan decided the object and the contents of activities of the committee. The object was the same as the last year's and the contents were as follows:

- 1) Case study on decommissioning of nuclear power plants and basic survey on decommissioning of fuel cycle facilities.
- 2) Survey on the current regulations of decommissioning of nuclear facilities in the main countries in the world.
- 3) Survey of the main literatures on decommissioning of nuclear facilities in the world.

According to the above contents, one subcommittee was added to the three subcommittees formed in the last year. These are Planning and General Subcommittee (leader; T. Egashira), Dismantling Technology Subcommittee (leader; T. Onda), Decontamination and Waste Disposal Subcommittee (leader; K. Ueno) and Fuel Reprocessing and Hot Laboratories Subcommittee (leader; T. Tsujino).

The number of the committee members increased to 55 specialists in JAERI, 24 specialists from the outside of JAERI and over 13 observers from the outside (including STA (Science and Technology Agency) members, MITI (Ministry of International Trade and Industry) members and members from some private industrial companies).

From November 1979 to March 1980, committee meetings were held 2 times and subcommittee meetings 18 times, and they had discussions on the above-mentioned subjects from various viewpoints. As the results, the committee prepared the summary report of following contents:

Chapt. 1 Introduction

Chapt. 2 Decommissioning plan of nuclear power plants,



Chapt. 3 Basic survey on decommissioning of nuclear fuel cycle facilities,

- Appendices: 1 Present status on decommissioning in the world,  
2 Current regulations relevant to decommissioning in the main countries -n the world,  
3 Summaries of 12 literatures on decommissioning.

These contents are to be explained by the chairman (K. Torikai) to the commissioners of Atomic Energy Commission of Japan.

In addition, several members of the committee surveyed technical terms on decommissioning of nuclear facilities and prepared the draft report on them.

In April 1980, the office of the committee has moved from Division of Reactor Engineering to Division of JPDR by reason that JPDR will not be operated any more and the decommissioning will be performed after some safety researched on light water reactor components.

#### References

- 1) Torikai K., et al.: "Survey on Decommissioning of Nuclear Facilities (II), Summary Report", (unpublished)
- 2) Iguchi A., et al.: "Technical Terms on Decommissioning of Nuclear Facilities (draft)", (unpublished)
- 3) Torikai K., et al.: "Survey on Decommissioning of Nuclear Facilities (Cont.)", (unpublished)

## Publication List

## 1. Nuclear Data and Group Constants

- (1) Nakagawa M., Takano H., Hasegawa A., Ishiguro Y., Katsuragi S.: "Assessment of JAERI-Fast Group Constants Set Version 2", ENC '79 Conf. (Humburg), Trans. Am. Nucl. Soc., 31 236 (1979).
- (2) Nakagawa M.: "Interference Effect of Strong Scattering Resonances on Elastic Removal Cross Section", J. Nucl. Sci. Technol., 16 (12) (1979).
- (3) Takano H., Ishiguro Y., Matsuura S.: "Effect of Resonance Interference Between  $^{238}\text{U}$  and  $^{133}\text{Cs}$  on Isotopic Correlation of Fission Product", Paper BC-12 presented at International Conference on Nuclear Cross Sections for Technology, Knoxville 22-26 Oct. 1979.
- (4) Takano H., Matsui Y., Ishiguro Y.: "Comparison Between Group Constants Produced by Processing Codes ETOX and TIMS", NEA Data Bank, Newsletter No. 23, 15 (1979).
- (5) Mukaiyama T., Koyama K., Kuroi H.: "Generation of an actinide isotopes cross section set for fast reactor calculations using data from ENDL and ENDF/B-IV", JAERI-M 8310 (1979).

## 2. Theoretical Method and Code Development

- (1) Nakagawa M., Asaoka T.: "A Computer Program for Perturbation Calculations by Correlated Sampling Monte Carlo Method", JAERI-M 8556 (1979) (in Japanese).
- (2) Fujimura T., Tsutsui T.: "EISPACK-J: Subprogram Package for Solving Eigenvalue Problems (Development and Benchmark Test of SSL, No.8)", JAERI-M 8253 (1979) (in Japanese).
- (3) Fujimura T.: "Benchmark Test for Computational Programs of Linear Algebra", Proceedings of the Institute of Mathematical Science of Kyoto University on the Evaluation of Mathematical Software, No.359 59 (1979) (in Japanese).
- (4) Fujimura T., Nishida T., Asai K.: "Manual on JSSL (JAERI Scientific Subroutine Library), 2nd Edition", JAERI-M 8479 (1979) (in Japanese).
- (5) Tajo Y.: "Stability of Vacancy Due to Noncentral Force Interactions in Diamond Structural Crystals", J. Phys. Soc. Jpn., 48, (1980).
- (6) Izui K., Furuno S., Nishida T., Otsu H.: "High Resolution Structure

Images and Their Application to Defect Studies", Nobel Symposium.  
(Lidingo) (1979).

- (7) Takahashi H., Nakahara Y.: "Analysis of Neutron Yield Produced by High Energy Proton", Int. Conf. on Nucl. Cross Sections for Technol., Knoxville (1979).
- (8) Kaneko Y.: "Probabilistic Method for Evaluation of Reactivity Margin of Experimental Very High Temperature Reactor", JAERI-M 8847 (1980) (in Japanese).
- (9) Tuchihashi K., Ishiguro Y. and Kaneko K.: "Resonance Absorption in High-Temperature Gas-Cooled Reactor Fuel with Double Heterogeneity", Nucl. Sci. Eng., 73, 163-173 (1980).
- (10) Koyama K., Yamano N., Miyasaka S.: "ORIGEN-JR: A Computer Code for Calculating Radiation Sources and Analysing Nuclide Transmutations", JAERI-M 8229 (1979).

### 3. Integral Experiment and Analysis

- (1) Kaneko Y. and Akino F.: "Critical Experiments on Enriched Uranium Graphite-Moderated Cores Related to High Temperature Gas Cooled Reactor", J. Atomic Energy Society of Japan, 21 (11), 876 (1979) (in Japanese).
- (2) Kaneko Y., Takeuchi M. and Masuyama T.: "Heating apparatus for single-fuel rod experiments", JAERI-M 8311 (1979) (in Japanese).
- (3) Kaneko Y., Yasuda H., Akino F. and Takeuchi M.: "Measurement of Reactivity Change with Temperature of Single Fuel Rod Using Coated Particles", JAERI-M 8846 (1980) (in Japanese).
- (4) Obu M., Shirakata K., Ichimori T.: "Proton-Recoil Counter Technique for Measurement of Fast Neutron Spectrum", J. Nucl. Sci. Technol., 16 (5), 329 (1979).
- (5) Obu M.: "Measurement of Fast Neutron Spectrum of FCA Assembly with Proton-Recoil Counters", JAERI-M 8327 (1979) (in Japanese).
- (6) Nakano M., Iijima S., Shirakata K., Hirota J.: "An Experimental Study of Heterogeneous LMFBR Core Using FCA Assemblies with Axial Internal Blanket", Int. Sym. Fast Reactor Physics, IAEA-SM-244/4 (1979).
- (7) Mukaiyama T., Mitani H., Koyama K., Obu M., Kuroi H.: "Evaluation of Actinide Cross Sections by Integral Experiments in Fast Critical Assembly FCA", Proceedings of the International Conference on Nuclear Cross Sections for Technology (Knoxville, Oct., 1979).

- (8) Koyama K., Mitani H., Kuroi H.: "Effect of Fission Product Accumulation on Sodium Void Worth", Int. Sym. Fast Reactor Physics, IAEA-SM-244/2 (1979).

#### 4. Shielding

- (1) Miura T., Takeuchi K. and Yamano N.: "Fast Neutron Transport through Laminated Iron-Water Shield", J. Nucl. Sci. Technol., 16 (8), 563 (1979).
- (2) Yamano N., Koyama K. and Minami K.: "Method of Calculation for Anisotropic Transmission Problems by  $S_N$ -Transport Code", J. Nucl. Sci. Technol., 16 (12), 919 (1979).
- (3) Sasamoto N. and Takeuchi K.: "An Improvement of the PALLAS Discrete Ordinates Transport Code", Nucl. Sci. Eng., 71 (3), 330 (1979).
- (4) Sasamoto N. and Takeuchi K.: "Two-Dimensional Shielding Benchmark Calculations by Discrete Ordinates and Monte Carlo Codes", Newsletter, SECU, NEA-Data Bank, No.23, 87 (1979).
- (5) Sasamoto N. and Takeuchi K.: "Analysis of  $^{60}\text{Co}$  Gamma-ray Transport through Air by Discrete Ordinates Transport Codes", Nucl. Technol., 47 (1), 189 (1980).
- (6) Tanaka S., et al.: "Shielding Benchmark Problems (II)", JAERI-M 8686 (1980) (in Japanese).
- (7) Asaoka T.: "Computer Program JN-METD3 to Deal with Neutron and Gamma-ray Transport in Multilayer Slabs by the  $j_N$  Method", JAERI-M 8672 (1980).

#### 5. Reactor and Nuclear Instrumentation

- (1) Sakai E., Kubo K., Yoshida H.: "Temperature Dependence of Thermal Neutron Detection Performance of  $^3\text{He}$  Proportional Counters", IEEE Trans. NS-27(1), 776 (1980).
- (2) Sakai E.: "Measurement of In-Situ Environmental Gamma-Rays Using Ge Detectors", Genshiryoku Kogyo, 25 (12), 60 (1979) (in Japanese).
- (3) Sakai E.: "Recent Topics on Gamma-Ray Detector Development", Hoshasen to Sangyo, No. 15, 5 (1980) (in Japanese).
- (4) Yoshida H., Kubo K.: "Programming on Canberra 8100/QUANTA System — Program Development with CLASS Language", JAERI-M 8694 (1980) (in Japanese).

- (5) Sakai E., et al.: "Test Procedures of Germanium Gamma-Ray Detectors", JIS Z 4520-1979 (1979) (in Japanese).
- (6) Nakatani H., Sakai E., Katagiri M.: "Fabrication of  $\text{HgI}_2$  Nuclear Radiation Detectors", JAERI-M 8478 (1979) (in Japanese).
- (7) Terada H., Katagiri M., Takahashi H., Wakayama N.: "In-Situ Measurement of Fission Product Plateout in In-Pile Gas Loop Using Portable  $\text{Ge(Li)}$  Gamma-Ray Spectrometer", J. Nucl. Sci. Technol., 17 (3), 225 (1980).
- (8) Baba H., Suzuki T., Nakahara Y., Yagi H.: "Determination of Plutonium Isotopic Ratios by  $\text{Ge(Li)}$   $\gamma$ -Ray Spectrometry", JAERI-M 8450 (1979) (in Japanese).
- (9) Baba H., Yagi H.: "Simulation for Isotopic Ratio Determination of Plutonium by  $\text{Ge(Li)}$   $\gamma$ -Ray Spectrometry", JAERI-M 8451 (1979) (in Japanese).
- (10) Wakayama N.: "Sensors and Transducers in the Nuclear Radiation Environment", Journal of the Japan Society of Mechanical Engineers, Vol.82, No. 731, pp.1154-1159, Oct. (1979) (in Japanese)

## 6. Reactor Control and Diagnosis

- (1) Shinohara Y.: "Needs of Robot Technology in Nuclear Installations", Robot, 23 34 (1979) (in Japanese).
- (2) Shinohara Y.: "Application of Systems Control Theories to Nuclear Reactors", Systems and Control, 23 (11), 614 (1979) (in Japanese).
- (3) Shinohara Y.: "Status of Robots for Nuclear Application", Oyo Kikai Kogaku, 9 116 (1979) (in Japanese).
- (4) Kambayashi Y.: "Position Control Characteristics of a Plasma Column with Proportional Control Law", JAERI-M 8461 (1979).
- (5) Kambayashi Y.: "Over-all Transfer Functions of a Position-Controlled JT-60 Plasma Column", JAERI-M 8462 (1979).
- (6) Oguma R.: "Application of the AR Modeling Technique to Study of The Resonant Power Oscillation in the Halden Boiling Water Reactor", JAERI-M 8579 (1979) (in Japanese).
- (7) Oguma R. and Matsubara K.: "Dynamics Analysis of Boiling Water Reactor via Multivariate Autoregressive (MAR) Model", Keisoku to Seigyō, 19 (7) 626 (1980) (in Japanese).

## 7. Fusion Reactor Technology

- (1) Maekawa H., Oyama Y., Kusano J. and Nakamura T.: "Absolute Fission-Rate Distribution in Graphite-Reflected Lithium Oxide Blanket Assembly", J. Nucl. Sci. Technol., 16 (5) 377 (1979).
- (2) Inoue S., Taji Y., Nakahara Y., Suzuki T.: "Monte Carlo Treatment for Neutral Particle Transport Problem in a Toroidal Plasma", Nucl. Sci. Eng., 73, 119 (1980).

## 8. Activities of the Committees

- (1) Hirota J., Inoue T.: "Reactor Physics Activities in Japan - November 1978 to September 1979", NEACRP-L-231 (Japan).